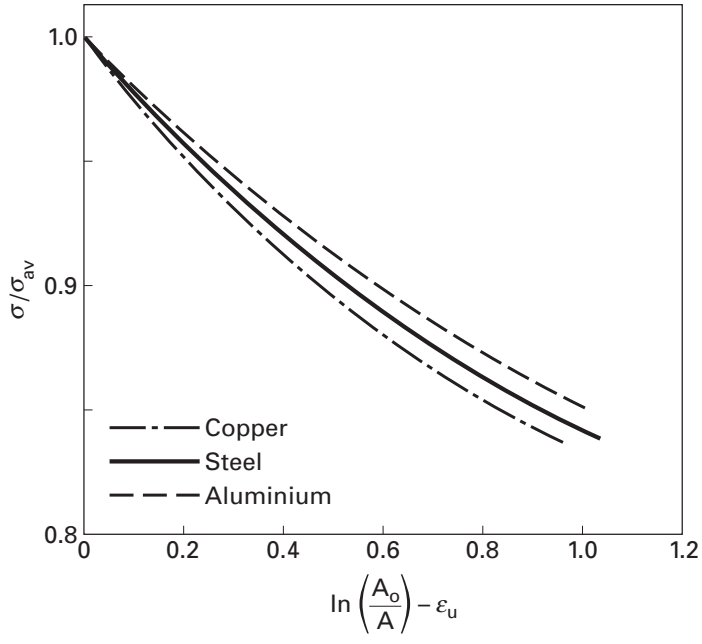


**Fig. 3.10** Correction factor for necking as a function of strain in neck, $\ln(A_0/A)$, minus strain at necking, $\varepsilon_u$. (Adapted with permission from W. J. McGregor Tegart, *Elements of Mechanical Metallurgy* (New York: MacMillan, 1964), p. 22.)

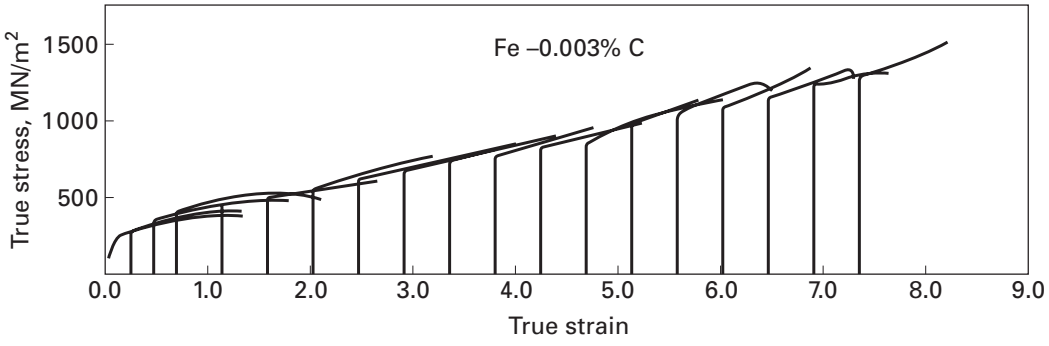


**Fig. 3.11** Stress–strain curves for Fe–0.003% C alloy wire, deformed to increasing strains by drawing; each curve is started at the strain corresponding to the prior wire-drawing reduction. (Courtesy of H. J. Rack.)

wire consists of pulling it through a conical die; at each pass, there is a reduction in cross section. Tensile tests were conducted after different degrees of straining (0 to 7.4) by wire drawing; it can be seen that the wire work-hardens at each step. However, the individual tensile tests are interrupted by necking and fracture. In wire-drawing, necking and fracture are inhibited by the state of stress in the deformation zone (compressive). The individual true-stress–true-strain curves were corrected for necking by Bridgman's technique; in each case, the individual curve fits fairly well into the overall work-hardening curve. It may be concluded that the individual tensile test gives only a very

limited picture of the overall work-hardening response of a metal; for the wire in Figure 3.11 the total strain exceeded 7.4.

### 3.2.3 Strain Rate Effects

For many materials, the stress–strain curves are sensitive to the strain rate $\dot{\varepsilon}$. The lowest range of strain rates corresponds to creep and stress-relaxation tests. The tensile tests are usually conducted in the range $10^{-4}\ \text{s}^{-1} < \dot{\varepsilon} < 10^{-2}\ \text{s}^{-1}$. At strain rates on the order of $10^{2}\ \text{s}^{-1}$, inertial and wave-propagation effects start to become important. The highest range of strain rates corresponds to the passage of a shock wave through the material.

More often than not, the flow stress increases with strain rate; the work-hardening rate is also affected by it. A parameter defined to describe these effects

$$m = \left.\frac{\partial \ln \sigma}{\partial \ln \dot{\varepsilon}}\right|_{\varepsilon,T}, \tag{3.21}$$

is known as the *strain rate sensitivity*. Equation 3.21 can also be expressed as

$$\boxed{\sigma = K\dot{\varepsilon}^{m}.} \tag{3.22}$$

where $K$ is a constant. Note that this $K$ is different from the Ludwik–Hollomon parameter.

Materials can be tested over a wide range of strain rates; however, standardized tensile tests require well-characterized strain rates that do not exceed a critical value. High-strain-rate tests are often used to obtain information on the performance of materials under dynamic impact conditions. The cam plastometer is one of the instruments used. In certain industrial applications, metals are also deformed at high strain rates. Rolling mills generate bar velocities of 180 km/h; the attendant strain rates are extremely high. In wire-drawing, the situation is similar.

Figure 3.12(a) shows the effect of different strain rates on the tensile response of AISI 1040 steel. The yield stress and flow stresses at different values of strain increase with strain rate. The work-hardening rate, on the other hand, is not as sensitive to strain rate. This illustrates the importance of correctly specifying the strain rate when giving the yield stress of a metal. Not all metals exhibit a high strain rate sensitivity: Aluminum and some of its alloys have either zero or negative $m$. In general, $m$ varies between 0.02 and 0.2 for homologous temperatures between 0 and 0.9 (90% of the melting point in K). Hence, one would have, at the most, an increase of 15% in the yield stress by doubling the strain rate. It is possible to determine $m$ from tensile tests by changing the strain rate suddenly and by measuring the instantaneous change in stress. This technique is illustrated in

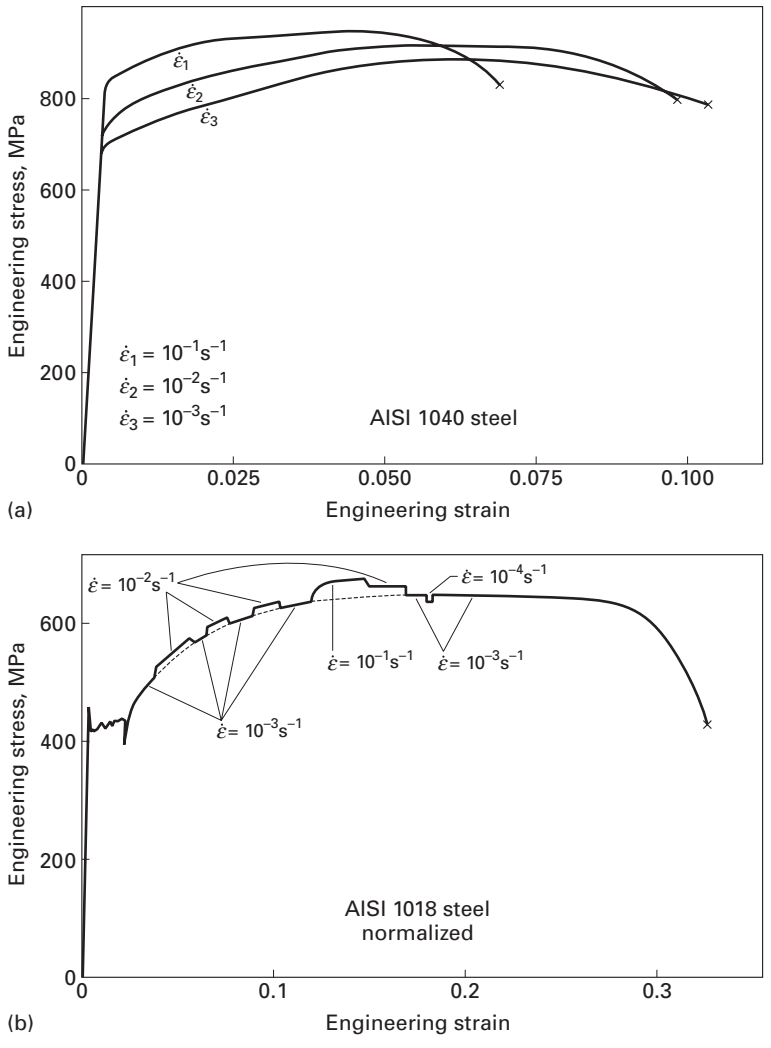


**Fig. 3.12** (a) Effect of strain rate on the stress–strain curves for AISI 1040 steel. (b) Strain-rate changes during tensile test. Four strain rates are shown: $10^{-1}$, $10^{-2}$, $10^{-3}$, and $10^{-4}$ $s^{-1}$.

Figure 3.12(b). Applying Equation 3.22 to two strain rates and eliminating $K$, we have

$$m = \frac{\ln(\sigma_2/\sigma_1)}{\ln(\dot{\varepsilon}_2/\dot{\varepsilon}_1)} \tag{3.23}$$

The reader can easily obtain $m$ from the strain-rate changes in the figure.

Some alloys show a peculiar plastic behavior and are called *superplastic*. When necking starts, the deformation concentrates itself at the neck. Since the velocity of deformation is constant, and the effective length of the specimen is reduced during necking, the strain rate increases ($\dot{\varepsilon} = v/L$). If a material exhibits a positive strain-rate sensitivity, the flow stress in the neck region will increase due to the increased strain rate; hence, necking is inhibited. This topic is treated

in greater detail in Section 15.8 – Superplasticity; it is what takes place in superplastic alloys, which can undergo uniform plastic strains of up to 5,000%.

## Example 3.2

Can the necking phenomenon be observed in *any* kind of mechanical test? Point out some of the problems that this phenomenon can cause during tensile testing.

***Solution***: No, necking is an artifact of the tensile test only. A reduction in cross-sectional area at any irregularities along the length of the specimen occurs in the tension mode only, and therefore, the phenomenon of necking occurs in tension only. In compression, the specimen bulges out.

After necking starts, the plastic deformation is concentrated in a very narrow region of the sample. Thus, one must not compare the total deformation corresponding to failure for two specimens that have different gage lengths. In order to avoid such complications, one should only compare the uniform elongation or use the reduction in area, i.e., the true-strain definition of the final strain. Strain gages and clip-on extensometers will not function properly or give accurate results after necking has begun.

## Example 3.3

Tensile testing of brittle materials such as ceramics is not very common, but is being resorted to in many laboratories. Why? Comment on the problems of doing tensile testing on ceramics.

***Solution***: Direct tensile testing of a sample results in a simple stress state over the whole volume of the sample gage length. All the volume and surface flaws in the gage length of the specimen are called into play and lead to a true measure of the material strength. Hence, there is increasing interest in tensile testing of ceramics. One major problem, however, is that of alignment of the sample. Any offcenter application of the load or loading at an angle can result in a combined state of bending and tension in the specimen. Stresses induced in such a state are called *parasitic bending stresses* and can lead to errors in the computed tensile strength values or even fracture the sample while it is being aligned in the machine. Some self-aligning grips have been designed to take care of these problems. This leads to rather long specimens and rather complex machining of the specimen. All of this makes tensile testing of ceramics very expensive!

## Example 3.4

Determine, for the curve shown in Figure E3.4.1,

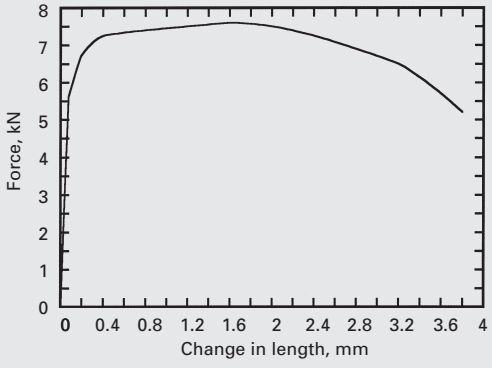


**Fig. E3.4.1**

(a) Young's modulus
(b) the UTS
(c) the yield stress (with a 0.2% offset)
(d) the uniform strain
(e) the total strain
(f) the engineering stress–strain curve.

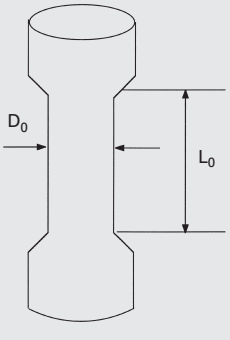


**Fig. E3.4.2**

The dimensions of the specimen, which is depicted in Figure E3.4.2, are:

$$L_0 = 20 \text{ mm},$$
$$D_0 = 4 \text{ mm}.$$

*Solution*:

(a) The elastic region is the straight line of the stress–strain curve. Taking both ends of this line, we obtain

$$\text{Point } 1 : F_1 = 0\,\text{kN}, \quad \Delta l_1 = 0,$$
$$\text{Point } 2 : F_2 = 5.5\,\text{kN}, \quad \Delta l_2 = 0.175\,\text{mm}.$$

To calculate Young's modulus ($E = \Delta\sigma/\Delta\varepsilon$), we have to change $F$, $\Delta l$ in terms of $\sigma$, $\varepsilon$:

Point 1:
$$\sigma_1 = \frac{F_1}{A_0} = 0,$$
$$\varepsilon_1 = \frac{\Delta l_1}{L_0} = 0.$$

Point 2:
$$\sigma_2 = \frac{F_2}{A_0} = \frac{5.5}{\pi(2)^2}\frac{\text{kN}}{\text{mm}^2} \approx 0.44\ \text{kN/mm}^2 = \ 440\ \text{MPa},$$
$$\varepsilon_2 = \frac{\Delta l_2}{L_0} \approx \frac{0.175}{20} \approx 0.009.$$

So

$$E = \frac{\Delta\sigma}{\Delta\varepsilon} = \frac{\sigma_2 - \sigma_1}{\varepsilon_2 - \varepsilon_1} \approx \frac{440}{0.009} \approx 49000\ \text{MPa} \approx 49\ \text{GPa}$$

(b) The UTS is the maximum value of the stress reached just before necking. Therefore, from the stress–strain curve, the UTS is equal to the stress corresponding to $F \approx 7.5$ kN. So

$$\text{UTS} = \frac{7.5}{\pi(2)^2} \approx 0.6\ \text{kN/mm}^2 \approx 600\ \text{MPa}$$

(c) The 0.2%-offset yield stress is

$$\varepsilon = \frac{\Delta l}{L_0}, \qquad \varepsilon = 0.2\% = 0.002, \quad l_0 = 20\ \text{mm}.$$

Therefore,

$$\Delta l = \varepsilon \cdot l_0 = 0.002 \times 20 = 0.04\,\text{mm}.$$

If you draw a line parallel to the elastic region calculated in part (a), from $\Delta l = 0.04$ mm, you will find that the point of intersection with the stress–strain curve is at $F \approx 6$ kN. At that point,

$$\sigma_y = \frac{6}{\pi(2)^2} \approx 0.48\ \text{kN/mm}^2 = 480\ \text{MPa}.$$

(d) For uniform strain, make a parallel line from the UTS point to the stress axis. You will then find that

$$\Delta l_u \approx 1.5\,\text{mm}.$$

The percent uniform strain is

$$\frac{\Delta l_u}{L_0} \times 100\% = \frac{1.5}{20} \times 100\% = 7.5\%.$$

(e) To find the total strain, we repeat (d) from the failure point. We have

$$\Delta l_t \approx 3.7\,\text{mm}.$$

The percent total strain is

$$\frac{\Delta l_t}{L_0} \times 100\% = \frac{3.7}{20} \times 100\% = 18.5\%.$$

(f) The engineering stress–strain curve is as shown in Figure E3.4.3.

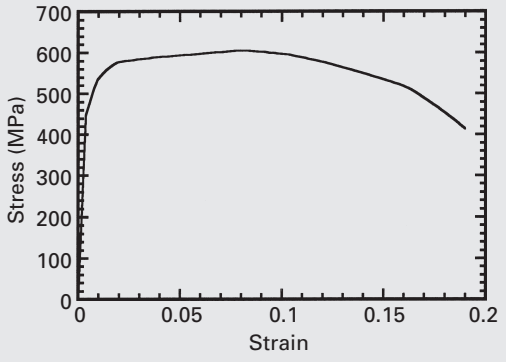


**Fig. E3.4.3**

## Example 3.5

The load–extension curve of an aluminum alloy, shown in Figure E3.5.1 was taken directly from a testing machine. A strain-gage extensometer was used, so machine stiffness effects can be ignored. From this curve, obtain the true and engineering stress–strain curves. Also, calculate the following parameters:

(a) Young's modulus
(b) the UTS
(c) the 0.2%-offset yield stress
(d) the uniform strain
(e) the total strain
(f) the reduction in area at the fracture.

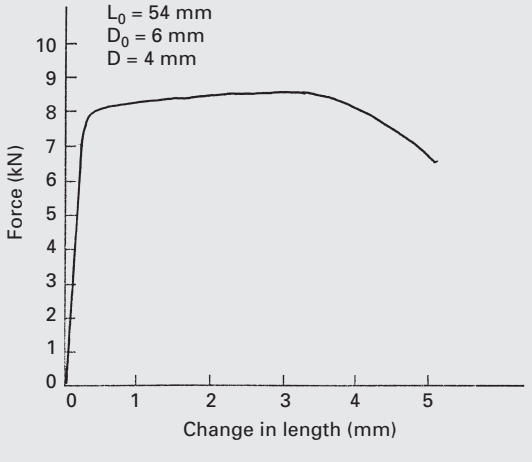


**Fig. E3.5.1**

***Solution***: We first change the coordinates to stress and strain. For engineering stresses, this is easily done:

$$\sigma_e = \frac{P}{A_0} \qquad (A_0 = 28.26\ \text{mm}^2),$$
$$\varepsilon_e = \frac{\Delta L}{L_0} \qquad (L_0 = 54\ \text{mm}).$$

The shape of the curve remains the same. For true stresses and true strains, we have to convert the engineering values into true values using the equations

$$\sigma_t = \sigma_e(1 + \varepsilon_e),$$
$$\varepsilon_t = \ln(1 + \varepsilon_e).$$

This is valid up to the onset of necking. Beyond necking (which starts at the UTS), we have only one point: that corresponding to failure. We can establish the true strain in the neck from the equation

$$\varepsilon_f = \ln \frac{A_0}{A_f} = \ln \frac{\pi \times 9}{\pi \times 4} = 0.81.$$

The corresponding true stress is

$$\sigma_t = \frac{P}{A} = \frac{6.5}{\pi \times 4} \frac{\text{kN}}{\text{mm}^2},$$
$$\sigma_t = 515\,\text{MPa}.$$

The other parameters are determined as follows:

(a) Young's modulus:

$$E = \text{slope of elastic part}$$
$$= \frac{\Delta\sigma}{\Delta\varepsilon}$$
$$= \frac{250}{0.004}\ \text{MPa}$$
$$\approx 63\ \text{GPa}.$$

(b) UTS $\approx$ 300 MPa ($\sigma_{\max}$).
The corresponding true stress is

$$\sigma_t = 300(1 + 0.056) = 317\,\text{MPa}.$$

(c) 0.2%-offset yield stress:

$$\sigma_{ys} \approx 280\,\text{MPa}.$$

(d) The uniform strain is approximately equal to 0.056.
The corresponding true strain is

$$\varepsilon_t = \ln(1 + 0.056) = 0.054.$$

(e) The total strain is approximately equal to 9%.
(f) Reduction in area at the fracture:

$$q = \frac{A_0 - A_f}{A_0} = \frac{\pi \times 3^2 - \pi \times 2^2}{\pi \times 3^2} = 0.55, \quad \text{or} \quad 55\%.$$

The true and engineering stress–strain curves are shown in Figure E3.5.2(a). The engineering curve is shown blown up in Figure E3.5.2(b).

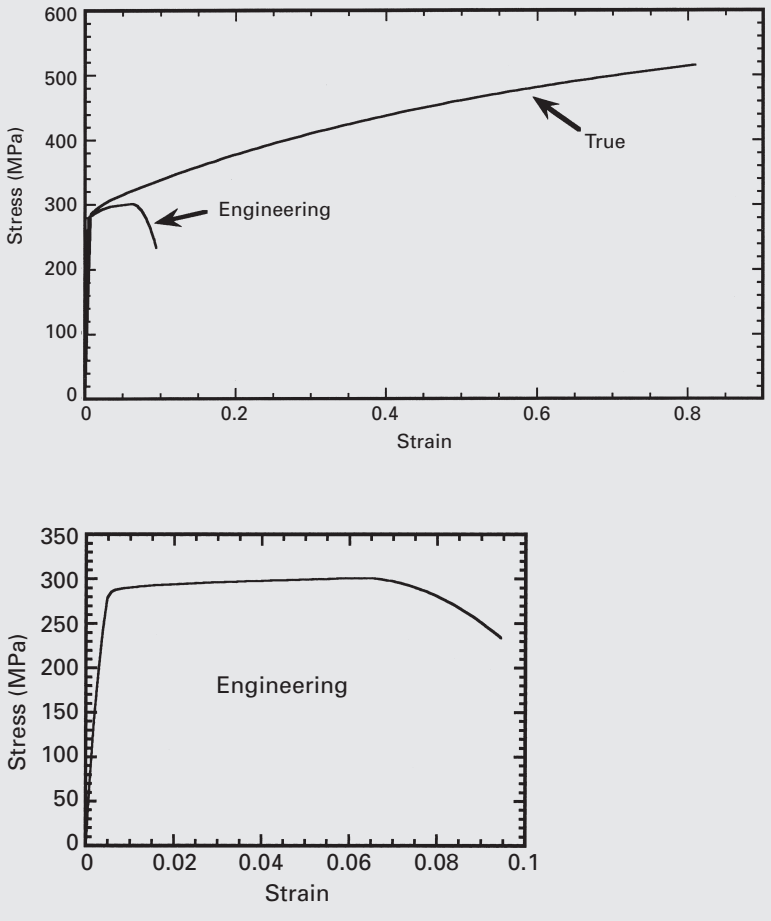


**Fig. E3.5.2**

## 3.3 Plastic Deformation in Compression Testing

In compression testing, a cylinder or a parallelepiped cube (with one side – the one parallel to the loading direction – longer than the other two) is subjected to compression between two parallel plates. The plates should have a self-alignment system, and they often ride on one or two hemispherical caps, as shown in Figure 3.13(a). If ceramics are being tested, it is also common to use special ceramic (WC, for instance) inserts between the specimen and the hemispherical caps. This eliminates indentation and plastic deformation of platens. Lubrication between the specimen and the plate is also very desirable, to decrease barreling (nonuniform deformation) of the specimen.

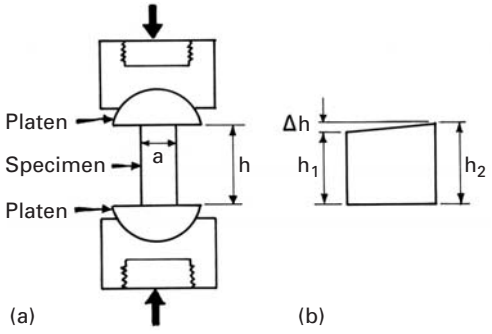


**Fig. 3.13** (a) Compression specimen between parallel platens. (b) Length inhomogeneity in specimen.

(Barreling will be discussed shortly.) The use of a thin Teflon™ coating, molybdenum disulfide, or graphite is recommended. It is also very important to ensure homogeneous loading of the specimen. This is particularly critical for ceramics, which often fail in the elastic range. It is easy to calculate stresses that arise when one of the parallel sides of a specimen is longer than the other. Figure 3.13(b) shows a specimen with a height difference $\Delta h$. The right side will experience a stress $\sigma = E(\Delta h/h_2)$ before the left side is loaded. For a typical ceramic, it is a simple matter to calculate the relationship between $\Delta\sigma$, the difference in stress from one side to the other, from $\Delta h$. For example, consider alumina, for which $E = 400$ GPa and $h = 10$ mm. The compressive strength of alumina can be as high as

$$\sigma_c = 4\,\text{GPa}.$$

Therefore, the failure strain is

$$\varepsilon_f = \frac{\sigma}{E} = 10^{-2}.$$

The corresponding displacement is

$$\Delta h = \varepsilon h = 0.1\,\text{mm}.$$

If the difference in height in the specimen is greater than 0.1 mm, the right side will fail as the left side starts to experience loading. This inhomogeneous loading is eliminated by the hemispherical caps, which can rotate to accommodate differences in height. However, if the surfaces of the specimen are not flat, stress inhomogeneities will arise, which can cause significant differences in the stress–strain response.

In reality, the platens also undergo elastic deformation, and a more uniform stress state is reached. Nevertheless, it is not a good practice to have the stresses on the two sides vary significantly, as this will result in erroneous strength determinations. The use of Teflon or thin metallic shims (stainless steel foil) also helps to alleviate the problem. This example illustrates the care that has to be exercised in choosing the dimensions of the specimen. In the case of ductile materials, it is not so critical, because plastic deformation will "homogenize" stresses.

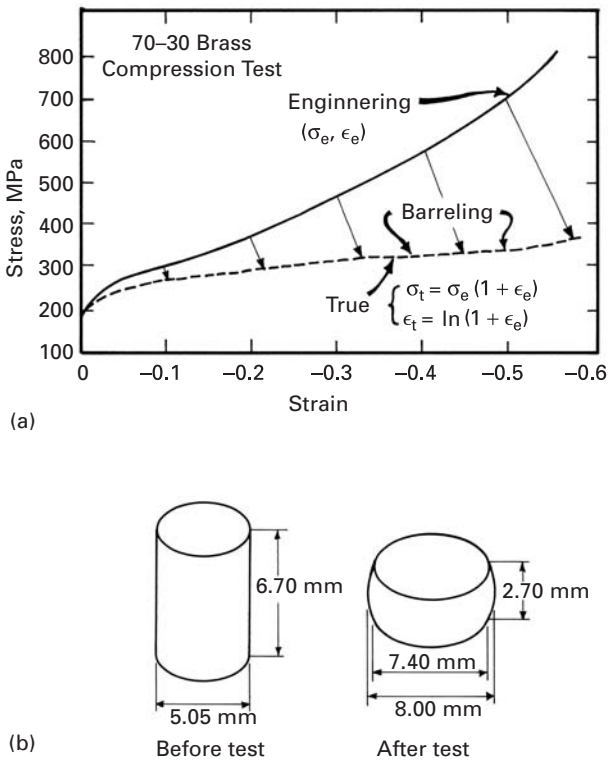


**Fig. 3.14** (a) Stress–strain (engineering and true) curves for 70–30 brass in compression. (b) Change of shape of specimen and barreling.

Figure 3.14(a) shows a typical compressive stress–strain curve for a metal (70–30 brass). The engineering-stress–engineering-strain curve ($\sigma_e$, $\varepsilon_e$) is concave, whereas it is convex in a tensile test. (See, for instance, Figure 3.3). The true-stress–true-strain curve is obtained by means of Equations 3.4 and 3.9. (See also Section 2.2). The translation of five points by using these equations is shown in Figure 3.14(a). After conversion to true-stress–true-strain values, the concavity of the curve is, for the most part, lost. In contrast, the true stress–strain curves in tension are displaced to the left (on the strain axis) and up (on the stress axis) from the engineering stress–strain curves. (See Figure 3.6) The phenomenon of necking is absent in compression testing, and much higher strains are reached. However, necking is replaced by barreling, a nonuniform plastic deformation resulting from friction between the specimen and the platen. Figure 3.14(b) shows the barreling of the brass specimen after the test. This barreling is responsible for some concavity in the true stress–strain curve (at a strain greater than $-0.4$) and limits the range of strain in compression testing of ductile materials to approximately $-0.3$ to $-0.4$. It will be shown, through a stress analysis, that frictional effects play an increasing role as the length/diameter ratio is decreased. This can significantly affect the results of a test. The compression of a cylindrical specimen under an engineering strain of $-0.5$, as simulated by finite elements under sticking conditions (i.e., there is no sliding at the

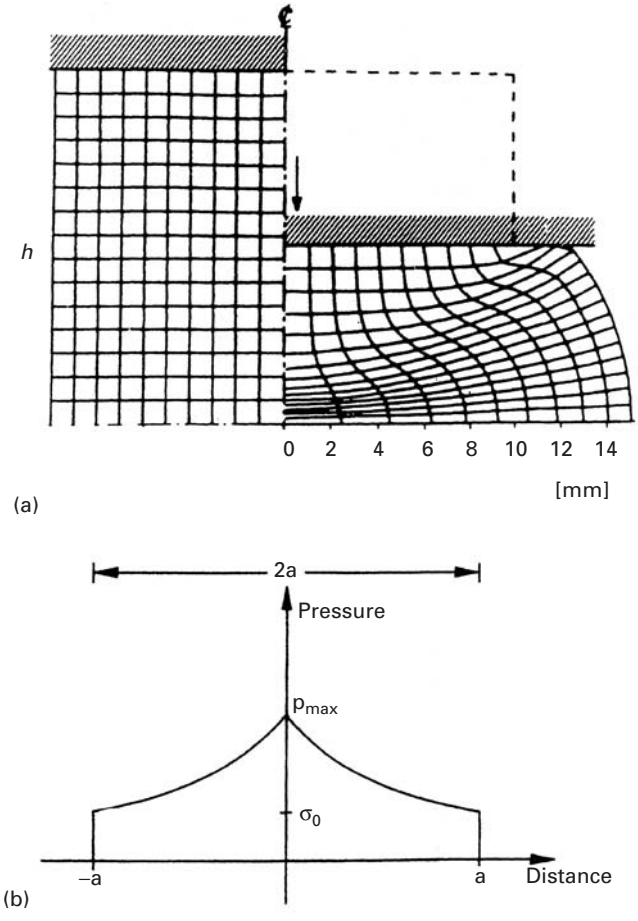


**Fig. 3.15** (a) Distortion of Finite Element Method (FEM) grid after 50% reduction in height *h* of specimen under sticking-friction conditions. (Reprinted with permission from H. Kudo and S. Matsubara, *Metal Forming Plasticity* (Berlin: Springer, 1979), p. 395.) (b) Variation in pressure on surface of cylindrical specimen being compressed.

specimen–platen interface), is shown in Figure 3.15. The distortion of the initially perpendicular grid is visible. This is an extreme case; strain inhomogeneities in the specimen are evident by differences in distortion of the grid. Barreling also can be seen.

The pressure or compressive stress is not uniform over the top and bottom surfaces of the specimen. Pressure differences can be calculated from an equation derived by Meyers and Chawla:[6]

$$p = \sigma_0 e^{2\mu(a-r)/h}.$$

[6] M. A. Meyers and K. K. Chawla, *Mechanical Metallurgy* (Englewood Cliffs, NJ: Prentice-Hall, 1984), p. 122.

This is the equation for the "friction hill." The compressive stress at the outside ($r = a$) is equal to $\sigma_0$, the material flow stress. In the center, it rises to $p_{max}$. The greater the ratio $a/h$, the more severe the problem is. The "friction hill" is schematically plotted in Figure 3.15(b). The pressure rises exponentially toward the center of the cylinder. The greater the coefficient of friction, the greater is $p_{max}$. A friction coefficient $\mu = 0.15$ is a reasonable assumption. It is instructive to calculate the maximum pressure for three $a/h$ ratios:

$$a/h = 2, \quad p_{max} = 1.82\sigma_0;$$
$$a/h = 1, \quad p_{max} = 1.34\sigma_0;$$
$$a/h = 0.5, \quad p_{max} = 1.16\sigma_0.$$

A specimen with an initial length/diameter ratio of 2 would have a maximum pressure of $1.07\sigma_0$. However, after a 50% reduction in length, the ratio $a/h$ is changed to $1.23\sigma_0$. The calculation is left as a challenge to the student; remember that the volume is constant. This can cause significant differences between the actual strength values of materials and stress readings. It is therefore recommended that these effects be considered. On the other hand, if $a/h$ is too small, the specimen will tend to buckle under the load.

## 3.4 The Bauschinger Effect

In most materials, plastic deformation in one direction will affect subsequent plastic response in another direction. The translation of the von Mises ellipse (kinematic hardening; see Section 3.7.4) is a manifestation of this relationship. The ellipse will move toward the direction in which the material is stressed. In one-dimensional deformation, the phenomenon is known as the *Bauschinger effect*. A material that is pulled in tension, for example, shows a reduction in compressive strength. Figure 3.16 illustrates the effect. A stress–strain curve is drawn, and the sequence 0–1–2 represents the loading direction. The material is first loaded in tension and yields at 1. At 2, the loading direction is reversed. Unloading occurs along the elastic line until the stresses become compressive. If there were no directionality effect, the material would start flowing plastically at a stress equal to $\sigma_2$. The idealized reverse curve is also shown in the figure. If the material did not exhibit a dependence on the stress direction, the compressive curve would be symmetrically opposite to the tensile curve. This idealized curve is drawn in dashed lines. The sequence is 0–1$R$–2$R$. Thus, compressive plastic flow, after the 0–1–2 tensile sequence, should occur at $\sigma_3 = \sigma_2 R = -\sigma_2$. If the material exhibits a Bauschinger effect, this stress is decreased from $\sigma_3$ to $\sigma_4$. Hence, the material "softens" upon inversion of the loading direction.

An actual example is shown in Figure 3.17. The 0.2% proof stress (the stress at which 0.2% plastic strain occurs) in compression is divided by the tensile flow stress that preceded it. These values are

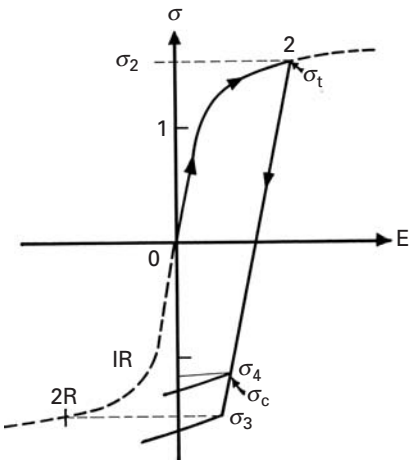


**Fig. 3.16** The Bauschinger effect.

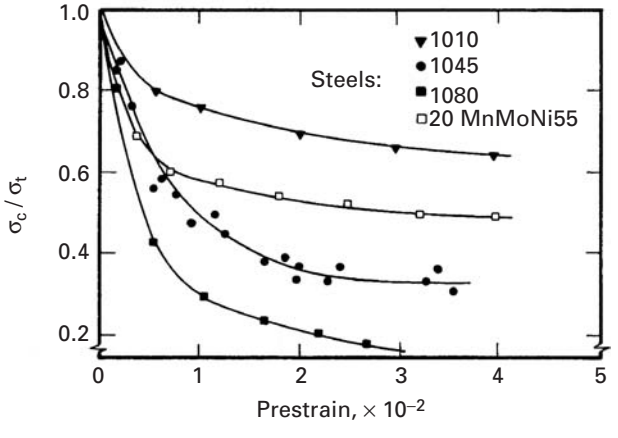


**Fig. 3.17** Ratio of compressive flow stress (0.2% plastic strain) and tensile flow stress at different levels of plastic strain for different steels. (After B. Scholtes, O. Vöhringer, and E. Macherauch, *Proc. ICMA6*, Vol. 1 (New York: Pergamon, 1982), p. 255.)

marked in the figure, which shows three plain carbon steels and one alloy steel. The change in flow stress is indeed highly significant and increases with plastic strain in tension. Thus, this factor cannot be ignored in design considerations when a component is to be subjected to compression stresses in service after being plastically deformed in tension.

## 3.5 Plastic Deformation of Polymers

### 3.5.1 Stress–Strain Curves

At a microscopic level, deformation in polymers involves stretching and rotating of molecular bonds. More commonly, one distinguishes the deformation mechanisms in polymers as brittle, ductile (with or without necking), and elastomeric. Figure 3.18 shows schematically the curves that correspond to these mechanisms. Clearly, factors such as the strain rate and temperature affect the shape of stress–strain

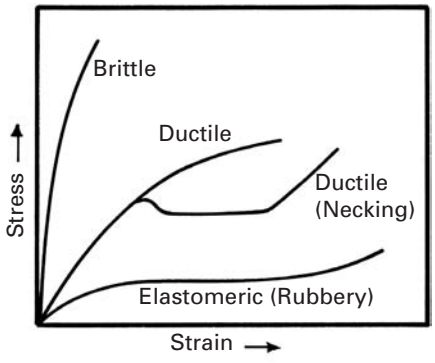


**Fig. 3.18** Schematic of the different types of stress–strain curves in a polymer.

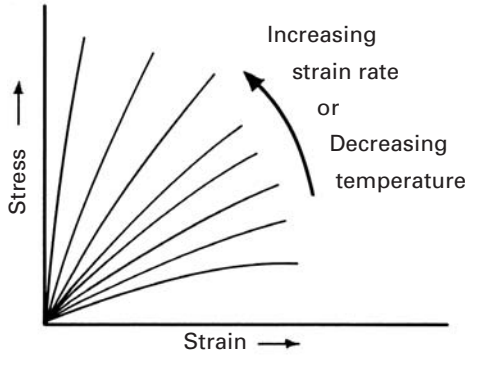


**Fig. 3.19** Effect of strain rate and temperature on stress–strain curves.

curves, much more so in polymers than in ceramics or metals. This is because the polymers are viscoelastic; that is, their stress–strain behavior is dependent on time. Temperature and strain rate have opposite effects. Increasing the strain rate (or decreasing the temperature) will lead to higher stress levels, but lower values of strain. Figure 3.19 shows this schematically.

Polymers (especially, linear, semicrystalline polymers), in a manner superficially similar to metals, can show the phenomena of yielding and necking. The necking condition for polymers can be represented, again in a manner similar to that for metals (see Section 3.2.2, Equation 3.19), by:

$$\frac{d\sigma_t}{d\varepsilon_t} = \sigma_t. \tag{3.24}$$

This equation says that necking occurs when the work-hardening rate $d\sigma_t/d\varepsilon_t$ attains a value equal to $\sigma$. At that point, the increase in strength due to work-hardening cannot compensate for the loss in strength caused by a decrease in cross-sectional area, and necking ensues.

### 3.5.2 Glassy Polymers

In a manner similar to its occurrence in metals, plastic deformation occurs inhomogeneously in polymers. Two forms of inhomogeneous

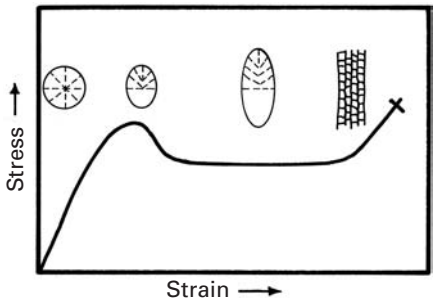


**Fig. 3.20** Schematic of necking and drawing in a semicrystalline polymer.

deformation are observed in glassy polymers: shear bands and crazes. Shear bands form at about 45° to the largest principal stress. The polymeric molecular chains become oriented within the shear bands without any accompanying change in volume. The process of shear band formation can contribute to a polymer's toughness because it is an energy-dissipating process. Shear yielding can take two forms: diffuse shear yielding and localized shear band formation. In localized shear, the shear is concentrated in thin planar regions, and the process involves a "cooperative" movement of molecular chains. The bands form at about 45° to the stress axis. Crazes are narrow zones of highly deformed polymer containing voids; the zones are oriented perpendicular to the stress axis. In the crazed zone, the molecular chains are aligned along the stress axis, but they are interspersed with voids. The void content in a craze may be as much as 55%. Unlike shear band formation, craze formation does not require the condition of constancy of volume. Generally, crazing occurs in brittle polymers. It can also occur to some extent in ductile polymers, but the dominant mode of deformation in these polymers is shear yielding. The phenomena of shear yielding and crazing are discussed further in Chapter 8.

Like ceramics, glassy or amorphous polymers show different stress – strain behaviors in tension and compression. The reason for this is that the surface flaws are much more dangerous in tension than in compression.

### 3.5.3 Semicrystalline Polymers

Semicrystalline polymers containing spherulites show a highly complex mode of deformation. Characteristically, these materials exhibit a ductile stress–strain curve with necking. Figure 3.20 shows such a stress–strain curve. Also illustrated is the process of transformation of a spherulitic structure to a fibrillar structure under the action of a tensile stress. Such orientation of polymeric chains parallel to the direction of stress increases the strength in that direction. Figure 3.21(a) shows a picture of the neck propagating in a linear polyethylene tensile sample while Figure 3.21(b) shows a schematic of the neck formation and propagation.

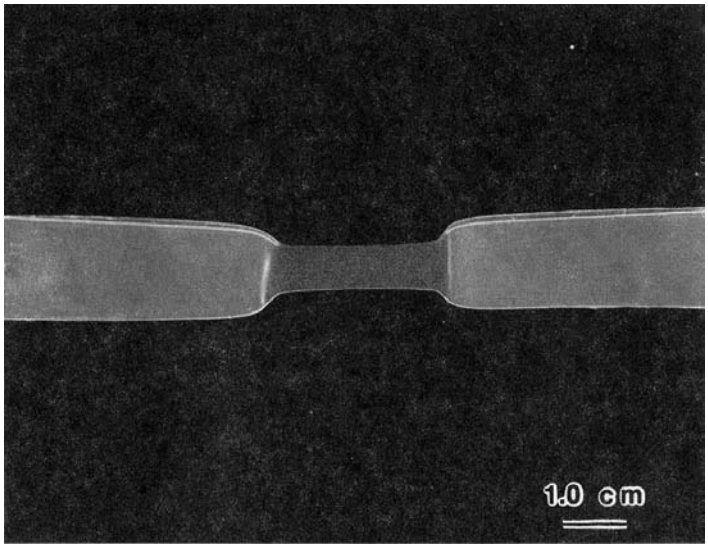


(a)

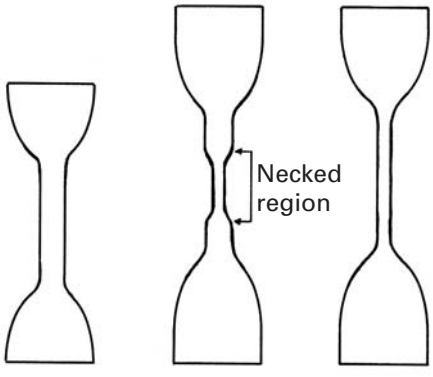


(b)

**Fig. 3.21** (a) Neck propagation in a sheet of linear polyethylene. (b) Neck formation and propagation in a specimen, shown in schematic fashion.

### 3.5.4 Viscous Flow

At high temperatures ($T \geq T_g$, the glass transition temperature), polymers undergo a viscous flow. Under these conditions, the stress is related to the strain rate, rather than the strain. Thus,

$$\boxed{\tau = \eta \frac{d\gamma}{dt},} \tag{3.25}$$

where $\tau$ is the shear stress, $\eta$ is the viscosity, and $t$ is the time. (The derivation of Equation 3.25 is given in Section 3.6.2.)

Viscous flow is a thermally activated process. It occurs by molecular motion, which increases as the temperature increases. The reader can appreciate the fact that such a viscous flow would involve the local breaking and re-forming of the polymeric network structure. The thermal energy for this is available above the glass transition

temperature $T_g$. Below $T_g$, the thermal energy is too low for breaking and re-forming bonds, and the material does not flow so easily. At very high temperatures, the viscosity $\eta$ is given by the Arrhenius-type relationship

$$\eta = A \exp\left(\frac{Q}{RT}\right), \tag{3.26}$$

where $A$ is a constant, $Q$ is the activation energy, $R$ is the universal gas constant, and $T$ is the temperature in kelvin.

### 3.5.5 Adiabatic Heating

There is a unique feature associated with the plastic deformation of polymers. Most of the work done during the plastic deformation of any material is converted into heat. In metals, this is not very important, because metals are good conductors, and except at extremely high rates of deformation, the heat generated is dissipated to the surroundings rather quickly, so that the temperature rise of the metal is insignificant. Polymers are generally poor conductors of heat. Thus, any heat generated in localized regions of a specimen due to plastic deformation can cause local softening. In the case of fatigue, heat may be dissipated rather easily at low strains and at low frequencies, even in polymers. A significant amount of softening, however, can result under conditions of high strain rates and high-frequency cyclic loading. This phenomenon is called *adiabatic heating*.

#### Example 3.6

Polyethylene is a linear-chain thermoplastic; that is, relatively speaking, it is easy to crystallize by stretching or plastic deformation. An extreme case of this is the high degree of crystallization obtained in a gel-spun polyethylene fiber. Describe a simple technique that can be used to verify the crystallization in polyethylene.

***Solution***: An easy way would be to use an X-ray diffraction technique. Unstretched polyethylene will consist mostly of amorphous regions. Such a structure will give diffuse halos. A diffuse halo indicates an irregular atomic arrangement – that is, an amorphous structure. A polyethylene sample that has been subjected to stretching or a gel-spun polyethylene fiber will have highly crystalline regions aligned along the draw axis. There may also be some alignment of chains in the amorphous regions. An X-ray diffraction pattern of such a sample would show regular spots and/or regular rings. The discrete spots indicate regular spacing characteristic of an orderly arrangement in a single crystal. Well-spaced regular rings indicate a polycrystalline region. Regular rings result from overlapping spots due to random crystalline orientations.

**Table 3.1** Mechanical Properties of Some Metallic Glasses[a]

| Alloy | *HV* (GPa) | $\sigma_y$ (GPa) | $H/\sigma_y$ | $E_g$ (GPa) | $Eg/\sigma_y$ |
|---|---|---|---|---|---|
| $Ni_{36}Fe_{32}Cr_{14}P_{12}B_6$ (Metglas 286AA) | 6.1 | 1.9 (tension) | 3.16 | 99.36 | 52 |
| $Ni_{49}Fe_{29}P_{14}B_6S_2$ (Metglas 286B) | 5.5 | 1.7 (tension) | 3.26 | 91.1 | 54 |
| $Fe_{80}P_{16}C_2B_1$ (Metglas 2615) | 5.8 | 1.7 (tension) | 3.35 | | |
| $Pd_{77.5}Cu_6Si_{36.5}$ | 3.4 | 1.08 (compression) | 3.17 | 61.9 | 57 |
| $Pd_{64}Ni_{16}P_{20}$ | 3.1 | 1 (compression) | 3.17 | 61.9 | 57 |
| $Fe_{80}B_{20}$ (Metglas 2605) | 7.6 | 2.55 (tension) | 2.97 | 116.6 | 45 |

[a]Adapted with permission from: L. A. Davis in *Rapidly Quenched Metals*, N. J. Grant and B. C. Giessen (eds.) (Cambridge, MA: MIT Press, 1976, p. 401), p. 369, Table 1.

## 3.6 Plastic Deformation of Glasses

The unique mechanical properties exhibited by metallic glasses are connected to their structure. Table 3.1 lists the hardnesses, yield stresses, and Young's moduli for several metallic glasses. The unique compositions correspond to regions in the phase diagram that have a very low melting point. The low melting points aid in the retention of the "liquid" structure. Metallic glasses are primarily formed by rapid cooling from the molten state, so that the atoms do not have time to form crystals. The Metglas group is commercially produced in wire and ribbon form. Young's modulus for glasses varies between 60 and 70% of the Young's modulus of the equilibrium crystalline structure. Li[7] has proposed a relationship between the shear modulus of the glassy and crystalline states, namely,

$$G_g = \frac{0.947}{1.947 - \nu} G_c \tag{3.27}$$

where $G_g$ and $G_c$ are the shear moduli of the glassy and crystalline states, respectively, and $\nu$ is Poisson's ratio. The crystalline Young's modulus of glasses is recovered when the material is annealed and crystallinity sets in. The yield stresses of metallic glasses are high, as can be seen in Table 3.1. For Fe–B metallic glasses, strength levels over 3.5 GPa were achieved. This is close to the highest yield strengths achieved in polycrystalline metals. (See Section 1.4.) The yield stresses

[7] J. C. M. Li, in *Frontiers in Materials Science – Distinguished Lectures*, L. E. Murr and C. Stein, eds. (New York: Marcel Dekker, 1976), p. 527.

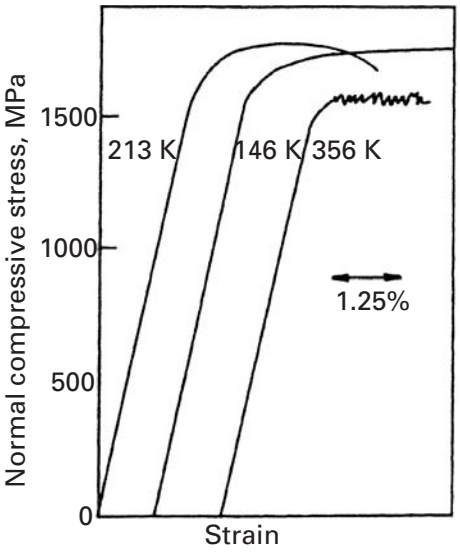


**Fig. 3.22** Compression stress–strain curves for $Pd_{77.5}Cu_6Si_{16.5}$. (Adapted with permission from C. A. Pampillo and H. S. Chen, *Mater. Sci. Eng.*, 13 (1974) 181.)

of the metallic glasses are usually 10 to 30 times higher than the yield stress of the same alloy in the crystalline state.

The micromechanical deformation mechanisms responsible for the unique mechanical properties of metallic glasses are still not very well understood. The absence of crystallinity has a profound effect on the mechanical properties. Grain boundaries, dislocations, mechanical twinning, and other very important components of the deformation of crystalline metals are not directly applicable to metallic glasses. Although the dislocations are not fully described until Chapter 4 (a brief description is given in Section 1.4), the concept is used in this section in an attempt to rationalize the mechanical response of metallic glasses. The lower Young's modulus is probably due to the less efficient packing of atoms, with a consequent larger average interatomic distance. The plastic part of the stress–strain curve also differs from the crystalline one. Here we have to distinguish between the behavior of the metallic glass above and below $T_g$, the glass transition temperature. As in silicate glasses, a temperature is defined above which the glass becomes viscous and deformation occurs by a viscous flow that is homogeneous. Only the deformation at temperatures below $T_g$ will be discussed here. Curves for small cylindrical specimens under compression are shown in Figure 3.22. There is little evidence of work-hardening, and the plastic range is close to horizontal. The surface of the specimens usually exhibits steps produced by shear bands. These shear bands have been found to be 20 nm thick, and the shear offset (step) has been found to be around 200 nm. This shows that deformation is highly inhomogeneous in metallic glasses and that, once shear starts on a certain plane, it tends to continue there. The plane of shear actually becomes softer than the surrounding regions. We can compute

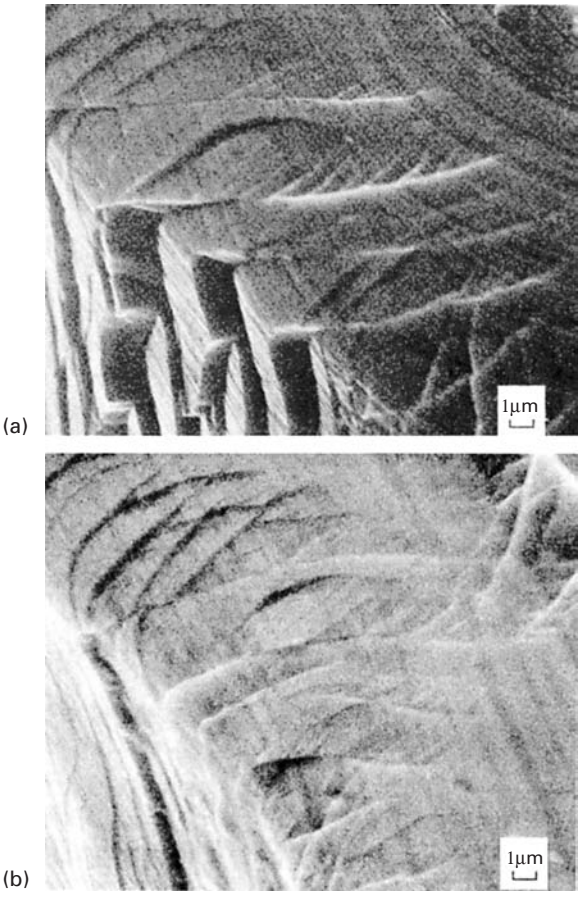


**Fig. 3.23** Shear steps terminating inside material after annealing at 250°C/h, produced by (a) bending and decreased by (b) unbending. Metglas $Ni_{82.4}Cr_7Fe_3Si_{4.5}B_{3.1}$ strip. (Courtesy of X. Cao and J. C. M. Li.)

the amount of shear strain in a band by dividing the band offset by the thickness. In the preceding case, it is equal to 10. This behavior is termed work-softening. The curves of Figure 3.22 provide macroscopic support for the absence of work-hardening. The equivalent of a dislocation can exist in a glass. The slip vector of the dislocation would fluctuate in direction and magnitude along the dislocation line, but its mean value would be dictated by some structural parameter.

Figure 3.23 shows slip lines and steps produced after bending and after unbending. We can see the slip lines terminating inside the metallic glass. The slips decrease in height on unbending. These observations tend to confirm the relevance of some kind of shear localization in the plastic deformation of metallic glasses.

### 3.6.1 Microscopic Deformation Mechanisms

Of the theories explaining the microscopic aspects of plastic deformation of metallic glasses, the best known are the dislocation theory of Gilman and the strain ellipsoid theory of Argon.

Figure 3.24(a) shows dislocation lines in crystalline and vitreous silica. Dislocations in crystalline solids will be studied in Chapter 4.

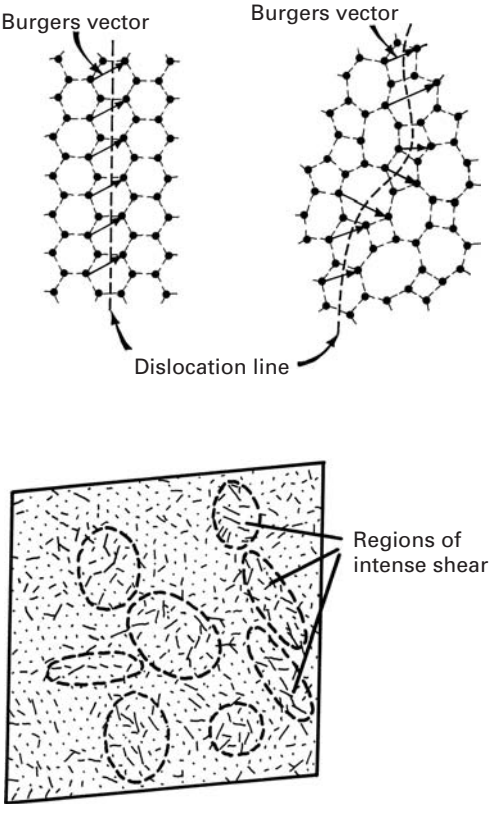


**Fig. 3.24** (a) Gilman model of dislocations in crystalline and glassy silica, represented by two-dimensional arrays of polyhedra. (Adapted from J. J. Gilman, *J. Appl. Phys*. 44 (1973) 675) (b) Argon model of displacement fields of atoms (indicated by magnitude and direction of lines) when assemblage of atoms is subjected to shear strain of $5 \times 10^{-2}$, in molecular dynamics computation. (Adapted from D. Deng, A. S. Argon, and S. Yip, *Phil. Trans. Roy. Soc. Lond*. A329 (1989) 613.)

The two-dimensional picture in the figure is analogous to the Zachariasen model for silica in Figure 1.18. The dislocation line is shown in the two cases, and we are looking at the dislocation "from the top down;" that is, the extra atomic plane is perpendicular to the surface of the paper. For the regular crystalline structure, all Burgers vectors are parallel and have the same magnitude. For the glassy structure, b fluctuates both in magnitude and direction. The dislocation line is not forced to remain in a crystallographic plane (there are no such planes in glasses), but can fluctuate. This is the *Gilman* mechanism for plastic deformation of glasses.

Experiments using "bubble rafts" and computational simulations indicate that there are localized regions of approximately ellipsoidal shape that undergo larger distortions than the bulk of the material and that are the main entities responsible for the plastic deformation of glasses. The ellipsoidal regions do not move, but undergo gradual distortion. Figure 3.24(b) shows the result of a computer simulation, including the positions and displacements of individual atoms. The lengths of the lines represent the displacements of the atoms. One can see regions of the material where the displacements of the atoms are larger. The ellipses become distorted, and the entire body deforms. This is the so-called *Argon* model for deformation of glasses, named after a renowned MIT professor (and not after a gas!).

### 3.6.2 Temperature Dependence and Viscosity

The mechanical response of glasses is often represented by their viscosity, which is a property of liquids. The viscosity, $\eta$ is defined as the velocity gradient that will be generated in a liquid when it is subjected to a specific shear stress, or

$$\tau = \eta \frac{dv}{dy}, \tag{3.28}$$

where $\tau$ is shear stress, $v$ is the velocity and $dv/dy$ is the velocity gradient. For temperature $T > T_m$, the viscosity is very low and the glass is a fluid. A characteristic value is $\eta \cong 10^{-3}$ Pa · s. For $T \sim T_g$, (the glass transition temperature), the viscosity is between $10^{10}$ and $10^{15}$ Pa · s. A common unit of viscosity is the Poise (P). Note that 1 P = 0.1 Pa · s. For $T < T_g$, the viscosity is $\eta > 10^{15}$ Pa · s. Mechanically speaking, the material is solid. Figure 3.25 shows these different regimens of mechanical response as a function of temperature, for soda–lime–silica glass and for some metallic glasses ($Au_{77}Si_{14}Ge_{19}$, $Pd_{77.5}Cu_6Si_{16.5}$, $Pd_{80}Si_{20}$, and $Co_{75}P_{25}$). The temperature is normalized by dividing it by $T_g$. The viscosity decreases at $T > T_g$, as

$$\eta = \eta_0 e^{Q/RT}, \tag{3.29}$$

where $Q$ is the activation energy for viscous flow. This is a classic Arrhenius response. The shear strength of the material can be related to the viscosity by

$$v = \frac{ds}{dt}; \quad \gamma = \frac{ds}{dy}$$

$$\tau = \eta \frac{dv}{dy} = \eta \frac{d}{dy}\left(\frac{ds}{dt}\right) = \eta \frac{d}{dt}\left(\frac{ds}{dy}\right) = \eta \frac{d\gamma}{dt} = \eta \dot{\gamma},$$

where $v$ is the velocity of one part of the material with respect to the other. The velocity is the displacement with time, $ds/dt$. By changing the order of differentiation, we obtain $d\gamma = ds/dy$. The change of strain with time is $\dot{\gamma} = d\gamma/dt$. A general relationship between shear stress, shear strain, and shear strain rate is

$$\boxed{\tau = \tau_0 \gamma^n \dot{\gamma}^m,} \tag{3.30}$$

where $n$ is the work-hardening coefficient and $m$ is the strain rate sensitivity. Since glasses do not work harden, $n = 1$. When $\tau$ is proportional to $\dot{\gamma}$, the strain rate sensitivity is equal to unity, and the material will be resistant to necking in tension. This is why glass can be pulled in tension to extremely high strains. Such behavior is discussed in greater detail in Chapter 13. Another class of materials, called *superplastic* materials, also exhibits this response when the grain size of the material is very small.

Viscosity is a very important characteristic of glassy materials. On the viscosity versus temperature curve of a given glassy material, one can identify certain important points. The *strain point* of glass is the temperature at which internal stresses are reduced significantly in a few hours. This corresponds to $\eta = 10^{13.5}$ Pa · s. The *annealing point* of

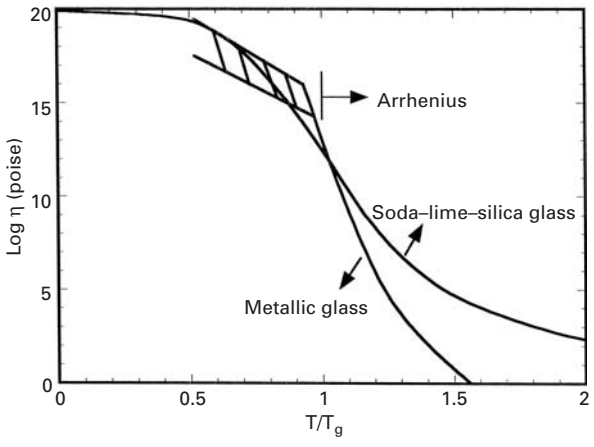


**Fig. 3.25** Viscosity of soda–lime–silica glass and of metallic glasses (Au–Si–Ge, Pd–Cu–Si, Pd–Si, $C_oP$) as a function of normalized temperature. (Adapted from J. F. Shakelford, *Introduction to Materials Science for Engineers*, 4th ed. (Englewood Cliffs, NJ: Prentice Hall, 1991), p. 331, and F. Spaepen and D. Turnbull in *Metallic Glasses*, ASM.) $1P = 0.1$ Pa · s.

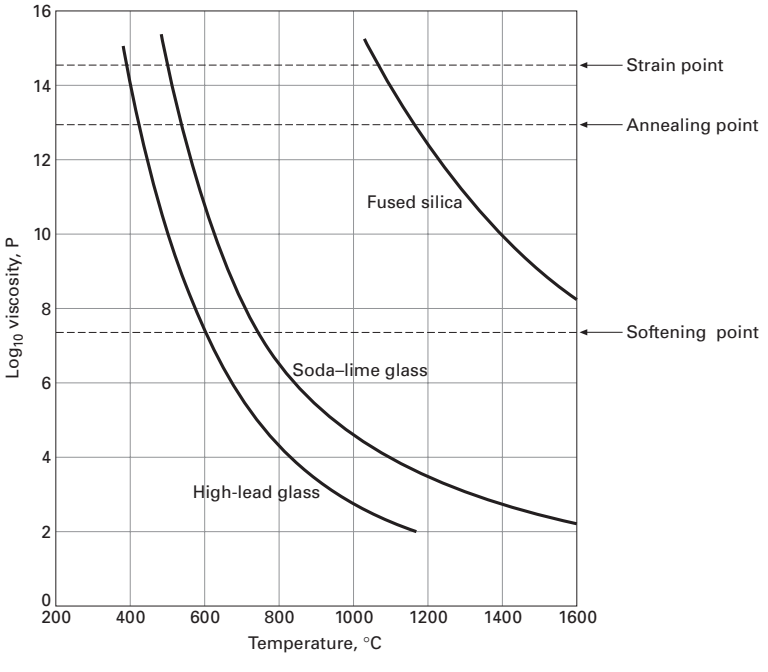


**Fig. 3.26** Viscosity of three glasses as a function of temperature. 1 P = 0.1 Pa · s.

a glass is the temperature at which the internal stresses are reduced in a few minutes such that $\eta = 10^{12}$ Pa · s. The *softening point* of a glass corresponds to $\eta = 10^{6.65}$ Pa · s. At this viscosity, the glass deforms rapidly under its own weight. The *working point* of glass corresponds to $\eta = 10^3$ Pa · s. At this viscosity, the glass is soft enough to be worked.

The viscosity of glasses is dependent on their composition. Soda–lime–silica and high-lead glasses have lower softening temperatures and are easier to work on. Pure silica, on the other hand, has a significantly higher softening point and requires significantly higher temperature. On the other hand, it can be used at higher temperatures. Figure 3.26 shows the temperature dependence of viscosity for these three glasses. Note that the ordinate of plot is in P, not Pa · s.

### Example 3.7

Consider a glass with a strain point of 500 °C and a softening point of 800 °C. Using the preceding viscosity values for the strain point and softening point, estimate the activation energy for the deformation of this glass.

***Solution***: We can write the viscosity as a function of temperature as

$$\eta = A \exp[Q/RT].$$

At the softening point,

$$10^{6.65} = A \ \exp\left[\frac{Q}{8.314 \times 1073}\right],$$

while at the strain point,

$$10^{13.5} = A \ \exp\left[\frac{Q}{8.314 \times 773}\right].$$

From these two expressions, we obtain, by division

$$10^{6.85} = \exp\left[\left(\frac{Q}{8.314}\right)\left(\frac{1}{773} - \frac{1}{1073}\right)\right],$$

or

$$Q = 362\,\text{kJ/mol}.$$

## 3.7 Flow, Yield, and Failure Criteria

The terms *flow criterion, yield criterion*, and *failure criterion* have different meanings. *Failure criterion* has its historical origin in applications where the onset of plastic deformation indicated failure. However, in deformation-processing operations this is obviously not the case, and plastic flow is desired. *Yield criterion* applies only to materials that are in the annealed condition. It is known that, when a material is previously deformed by, for instance, rolling, its yield stress increases due to work-hardening. (See Chapter 6.) The term *flow stress* is usually reserved for the onset of plastic flow in a previously deformed material. *Failure criterion* is applied to brittle materials, in which the limit of elastic deformation coincides with failure. To be completely general, a flow criterion has to be valid for any stress state. In a uniaxial stress state, plastic flow starts when the stress–strain curve deviates from its initial linear range. Uniaxial stress–strain curves are very easily obtained experimentally, and the deformation response of a material is usually known for this situation. The main function of flow criteria is to predict the onset of plastic deformation in a complex state of stress when one knows the flow stress (under uniaxial tension) of the material. Note that the value of the flow stress is strongly dependent on the state of stress, and if this effect is not considered, it can lead

to potentially dangerous errors in design. We next present some of these criteria.

### 3.7.1 Maximum-Stress Criterion (Rankine)

According to the maximum-stress criterion, plastic flow takes place when the greatest principal stress in a complex state of stress reaches the flow stress in uniaxial tension. Since $\sigma_1 > \sigma_2 > \sigma_3$, we have

$$\sigma_0(\text{tension}) < \sigma_1 < \sigma_0 \text{ (compression)},$$

where $\sigma_0$ is the flow stress of the material. Later (Section 3.7.5) we will see the situation where the compressive strength is greater than the tensile strength. The great weakness of this criterion is that it predicts plastic flow of a material under a hydrostatic state of stress; however, this is impossible, as shown by the following example. It is well known that tiny shrimp can live at very great depths. The hydrostatic pressure due to water is equivalent to 1 atm ($10^5$ N/m$^2$) for every 10 m; at 1,000 m below the surface, the shrimp would be subjected to a hydrostatic stress of $10^7$ N/m$^2$. Hence

$$-p = \sigma_1 = \sigma_2 = \sigma_3 = -10^7 \text{ N/m}^2.$$

A quick experiment to determine the yield stress of the shrimp could be conducted by carefully holding it between two fingers and pressing it. By doing the test with a live shrimp, one can define the flow stress as the stress at which the amplitude of the tail wiggling will become less than a critical value. This will certainly occur at a stress of about 0.1 MPa. Hence,

$$\sigma_0 = 0.1 \text{ MPa}.$$

The Rankine criterion would produce shrimp failure at

$$P \equiv -\sigma_0 = -0.1 \text{ MPa}.$$

This corresponds to a depth of only 10 m. Fortunately for all lovers of crustaceans, this is not the case, and hydrostatic stresses do not contribute to plastic flow.

### 3.7.2 Maximum-Shear-Stress Criterion[8] (Tresca)

Plastic flow starts when the maximum shear stress in a complex state of deformation reaches a value equal to the maximum shear stress at the onset of flow in uniaxial tension (or compression). The maximum shear stress is given by (see Section 2.6)

$$\tau_{\max} = \frac{\sigma_1 - \sigma_3}{2}. \tag{3.31}$$

For the uniaxial stress state, we have, at the onset of plastic flow,

$$\sigma_1 = \sigma_0, \quad \sigma_2 = \sigma_3 = 0;$$

so

$$\tau_{\max} = \frac{\sigma_0}{2}.$$

[8] H. Tresca, *Compt. Rend. Acad. Sci. Paris*, 59 (1864) 754; 64 (1867) 809.

Therefore,

$$\sigma_0 = \sigma_1 - \sigma_3. \tag{3.32}$$

This criterion corresponds to taking the differences between $\sigma_1$ and $\sigma_3$ and making it equal to the flow stress in uniaxial tension (or compression). It can be seen that it does not predict failure under hydrostatic stress, because we would have $\sigma_1 = \sigma_3 = p$ and no resulting shear stress.

### 3.7.3 Maximum-Distortion-Energy Criterion (von Mises)[9]

This criterion was originally proposed by Huber as "When the expression

$$\frac{\sqrt{2}}{2}[(\sigma_1 - \sigma_2)^2 + (\sigma_2 - \sigma_3)^2 + (\sigma_1 - \sigma_3)^2]^{1/2} > \sigma_0 \tag{3.33}$$

then the material will plastically flow." The left hand side is known as *effective stress*. The criterion was stated by von Mises without a physical interpretation. It is now accepted that it expresses the critical value of the distortion (or shear) component of the deformation energy of a body. Based on this interpretation, a body flows plastically in a complex state of stress when the distortional (or shear) deformation energy is equal to the distortional (or shear) deformation energy in uniaxial stress (tension or compression). This will be shown shortly. This criterion is also called $J_2$, which is the second invariant of the stress deviator. Students will learn about this in advanced "Mechanics of Materials" courses. $J_2$ is given by:

$$J_2 = \frac{1}{G}\left[(\sigma_1 - \sigma_2)^2 + (\sigma_2 - \sigma_3)^2 + (\sigma_1 - \sigma_3)^2\right]$$

Hence: $J_{\mathrm{n}} \geq \frac{\sigma_0^2}{3}$.

### 3.7.4 Graphical Representation and Experimental Verification of Rankine, Tresca, and von Mises Criteria

There is a convenient way to represent the Rankine, Tresca, and von Mises criteria for a plane state of stress. For this, one makes $\sigma_3 = 0$ and has $\sigma_1$ and $\sigma_2$. It will be necessary to momentarily forget the convention that $\sigma_1 > \sigma_2 > \sigma_3$, because it would not be obeyed for $\sigma_2 < 0$; we have $\sigma_2 < \sigma_3 = 0$. Figure 3.27(a) shows a plot of $\sigma_1$ versus $\sigma_2$. According to the Tresca criterion, plastic flow starts when

$$\tau_{\max} = \frac{\sigma_0}{2}.$$

The four quadrants have to be analyzed separately. In the first quadrant, there are two possible situations. For $\sigma_1$ greater than $\sigma_2$, $\tau_{\max} = (\sigma_1 - \sigma_3)/2$ and $\sigma_1 = \sigma_0$. This is a line passing through $\sigma_1 = \sigma_0$ and parallel to $0\sigma_2$. For $\sigma_2$ greater than $\sigma_1$, we have the converse situation and a line passing through $\sigma_2 = \sigma_0$ and parallel to $\sigma_1$.

[9] R. von Mises, *Göttinger Naehr. Math. Phys. Klasse*, 1913, p. 582.

In the second quadrant, $\sigma_2 > 0$ and $\sigma_1 < 0$. We have

$$\tau_{\max} = \frac{\sigma_1 - \sigma_2}{2} \quad \text{and} \quad \sigma_1 - \sigma_2 = \sigma_0.$$

This equation represents a straight line intersecting the $0\sigma_1$ axis at $\sigma_0$ and the $0\sigma_2$ axis at $-\sigma_0$. The flow criteria for quadrants III and IV are found in a similar way.

For the von Mises[10] criterion, we have, from Equation 3.33 and $\sigma_3 = 0$,

$$\sigma_0 = \tfrac{\sqrt{2}}{2}[(\sigma_1 - \sigma_2)^2 + \sigma_2^2 + \sigma_1^2]^{1/2},$$
$$\sigma_1^2 - \sigma_1\sigma_2 + \sigma_2^2 = \sigma_0^2.$$

This is the equation of an ellipse whose major and minor axes are rotated 45° from the orthogonal axes $0\sigma_1$ and $0\sigma_2$, respectively. It can be easily shown by applying a rotation of axes to the equation of an ellipse referred to its axes:

$$\left(\frac{\sigma_1}{a}\right)^2 + \left(\frac{\sigma_2}{b}\right)^2 = k^2. \tag{3.34}$$

From Equation 3.34, it can be seen that the Tresca criterion is more conservative than von Mises. The criterion would predict plastic flow for the stress state defined by point $P_1$, whereas the von Mises would not. However, both criteria are fairly close. It can be seen from Figure 3.27(a) that plastic flow may require a stress $\sigma_1$ greater than $\sigma_0$ for a combined state of stress. (See point $P_2$). However, there are regions (when one stress is tensile and another is compressive) where plastic flow starts when both stresses are within the interval

$$\sigma_0 < \sigma_1, \quad \sigma_2 < \sigma_0.$$

This occurs in the second and fourth quadrants. Point $P_2$ shows the situation very clearly. The conclusion is that the correct application of a yield criterion is very important for design purposes. For comparison purposes, the maximum-normal stress (Rankine) criterion is also drawn in Figure 3.27(a). It is just a square with sides parallel to the $0\sigma_1$ and $0\sigma_2$ axes and intersecting them at $(\sigma_0, 0)$, $(-\sigma_0, 0)$ $(0, \sigma_0)$, and $(0, -\sigma_0)$. We see that there is a considerable difference between the Rankine criterion, on the one hand, and the Tresca and von Mises criteria, on the other, for quadrants II and IV. This difference is readily explained by the fact that the Rankine criterion applies to brittle solids (including cast irons and steel below the ductile–brittle transition temperature), in which failure (or fracture) is produced by tensile stresses.

Figure 3.27(b) shows the three criteria, together with experimental results for copper, aluminum, steel, and cast iron. While copper and aluminum tend to follow the von Mises criterion (and, in a more conservative way, the Tresca criterion), cast iron clearly obeys the Rankine criterion. This is plainly in line with the low ductility exhibited by

[10] It is also called $J_2$ criterion; in this case, flow occurs at a critical value of $J_2 = \frac{1}{6}[(\sigma_1 - \sigma_2)^2 + \sigma_2^2 + \sigma_1^2]$.

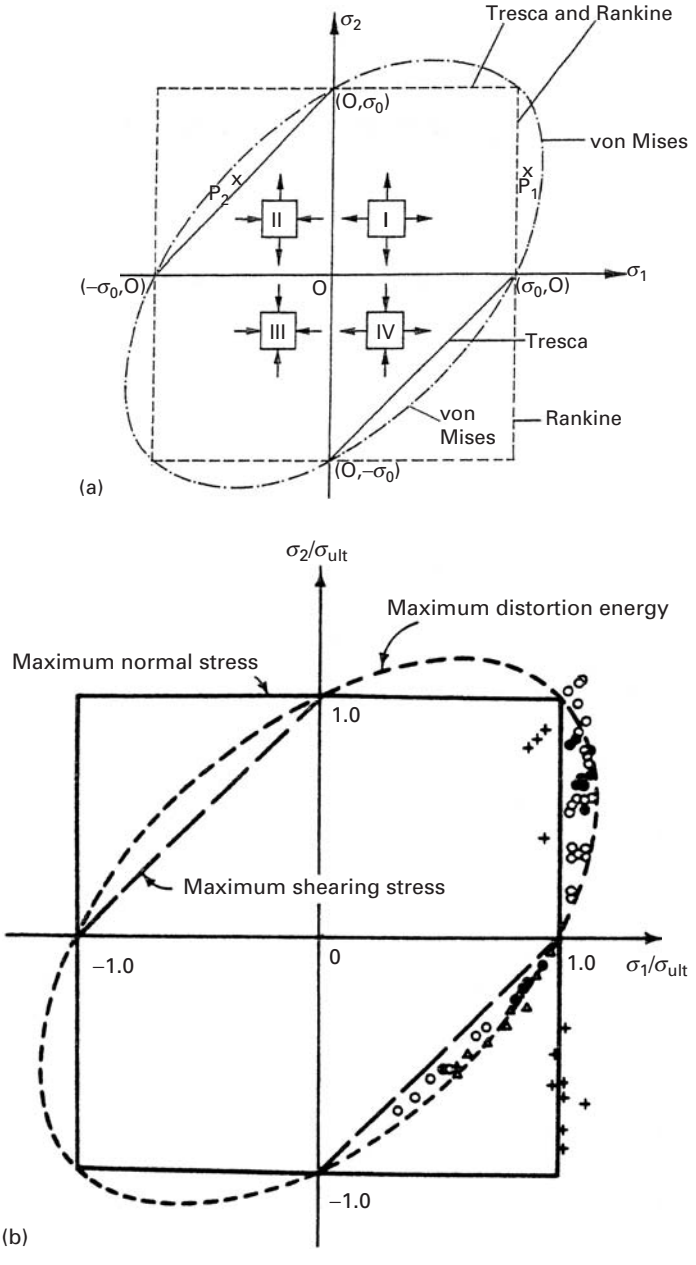


**Fig. 3.27** (a) Comparison of the Rankine, von Mises, and Tresca criteria. (b) Comparison of failure criteria with test. (Reprinted with permission from E. P. Popov, *Mechanics of Materials*, 2nd ed. (Englewood Cliffs, NJ: Prentice-Hall, 1976), and G. Murphy, *Advanced. Mechanics of Materials* (New York: McGraw-Hill, 1964), p. 83.)

cast iron. The reader is warned that the ratio $\sigma/\sigma_{ult}$, and not $\sigma/\sigma_0$, is used in the figure. Nevertheless, it serves to illustrate the difference in response.

The determination of the flow locus is usually conducted in biaxial testing machines, which operate in a combined tension–torsion or tension–hydrostatic-pressure mode. These two modes use tubular specimens, and one has to use the appropriate calculations to find the principal stresses. As the material is plastically deformed, we have an expansion of the flow locus. For the von Mises criterion, we can

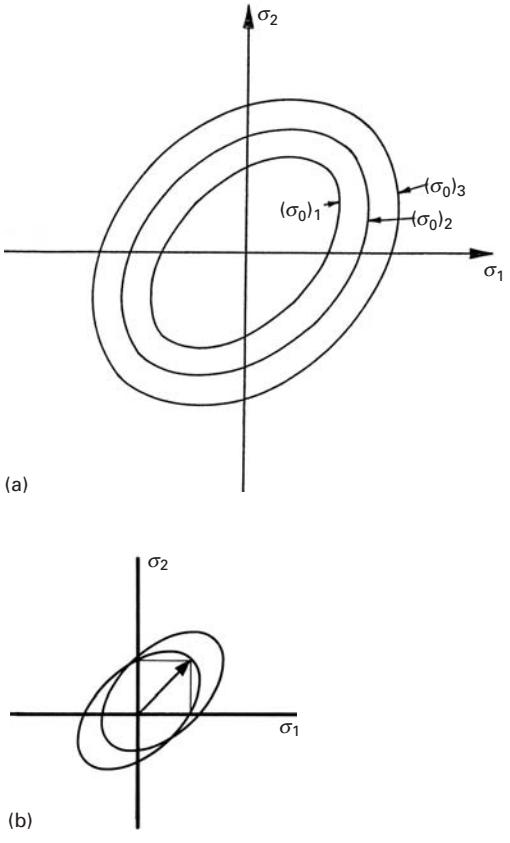


**Fig. 3.28** Displacement of the yield locus as the flow stress of the material due to plastic deformation. (a) Isotropic hardening. (b) Kinematic hardening.

envision concentric ellipses having increasing major and minor axes. This is illustrated in Figure 3.28(a). When the ellipse expands in a symmetric fashion, the hardening is the same in all directions and is called *isotropic*. Often, however, hardening in one direction (the loading direction) causes a change in flow stress in other directions that is different. This is very important in plastic-forming operations (stamping, deep drawing). The extreme case where the ellipse is just translated is shown in Figure 3.28(b). This case is called *kinematic hardening*. (See Section 3.4.)

## Example 3.8

A region on the surface of a 6061-T4 aluminum alloy component has strain gages attached, which indicate the following stresses:

$$\sigma_{11} = 70\,\text{MPa},$$
$$\sigma_{22} = 120\,\text{MPa},$$
$$\sigma_{12} = 60\,\text{MPa}.$$

Determine the yielding for both the Tresca and von Mises criteria, given that $\sigma_0 = 150$ MPa (the yield stress).

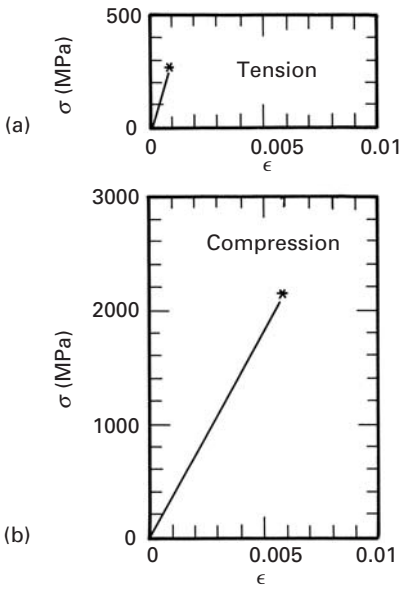


**Fig. 3.29** (a) Tensile strength and (b) Compressive strength of $Al_2O_3$.

***Solution***: We first have to establish the principal stresses. This is easily accomplished by a Mohr circle construction or by its analytical expression (the equation of a circle):

$$\sigma_{1,2} = \frac{\sigma_{11} + \sigma_{22}}{2} \pm \left[ \left( \frac{\sigma_{11} - \sigma_{22}}{2} \right)^2 + \sigma_{12}^2 \right]^{1/2},$$

$$\sigma_1 = 160 \text{ MPa}; \qquad \sigma_2 = 30 \text{ MPa}; \qquad \sigma_3 = 0.$$

According to Tresca, $\tau_{\max} = (160 - 0)/2 = 80$ MPa.

The value $\tau_{\max} = 80$ MPa exceeds the Tresca criterion ($\sigma_0/2 = 75$ MPa) and the alloy would be unsafe. The von Mises criterion gives

$$J_2 = \frac{1}{6}[(\sigma_1 - \sigma_2)^2 + (\sigma_1 - \sigma_3)^2 + (\sigma_2 - \sigma_3)^2]$$

$$= \frac{1}{6}[130^2 + 160^2 + 30^2]$$

$$= 7233 \text{ MPa}^2.$$

The maximum value of $J_2^M = (1/3)\sigma_0^2 = (1/3)150^2 = 7500$ MPa$^2$.

So $J_2 < J_2^M$, and the material does not yield. Plainly, the Tresca criterion is more conservative than von Mises.

### 3.7.5 Failure Criteria for Brittle Materials

As shown in Figure 3.29, the tensile strength of $Al_2O_3$ is approximately one-tenth of its compressive strength. Such is also the case for many brittle materials, such as concrete, rock, etc. Therefore, the Rankine, Tresca, and von Mises criteria have to be modified to incorporate this behavior. This will be done in the rest of the section, with the presentation of the Mohr–Coulomb, Griffith, and McClintock–Walsh criteria.

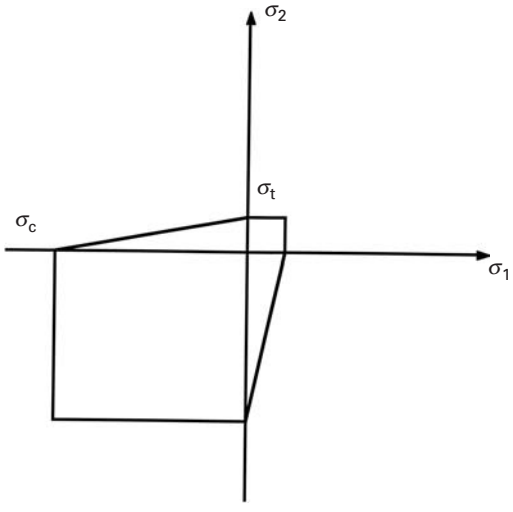


**Fig. 3.30** Schematic two-dimensional representation of Mohr–Coulomb failure criterion.

There are also other criteria (e.g., Babel–Sines), which will *not* be presented here.

**Mohr–Coulomb Failure Criterion**
This is simply the equivalent of the Tresca criterion with different tensile and compressive strengths. Figure 3.30 shows the Mohr–Coulomb criterion in a schematic fashion. The criterion for failure is a maximum shear stress; the compressive strength $\sigma_c$ is much higher than the tensile strength $\sigma_t$.

**Griffith Failure Criterion**[11]
This criterion simply states that failure will occur when the tensile stress tangential to an ellipsoidal cavity and at the cavity surface reaches a critical level $\sigma_0$. The criterion is a classic spin-off of Griffith's work of 1919. Griffith recognized that brittle materials contained flaws and that failure would occur at a specific level of stress at the flaw surfaces. He considered an elliptical crack oriented in a general direction with respect to the compression axis and calculated the stresses generated at the surface of the crack. Tensile stresses are generated by compressive loading; this might appear surprising at first sight, but will become clear in Chapter 7. If $\sigma_0$ is the tensile strength of the material, the following relationship is obtained:

$$\begin{array}{ll} (\sigma_1 - \sigma_2)^2 + 8\sigma_0(\sigma_1 + \sigma_2) = 0 & \text{if } \sigma_1 + 2\sigma_2 > 0, \\ \sigma_2 = \sigma_0 & \text{if } \sigma_1 + 2\sigma_2 < 0. \end{array} \tag{3.35}$$

The criterion proposed by Griffith is shown in Figure 3.31. The compressive failure stress is eight times the tensile failure stress, as is evident from Equation 3.31. This very important result is consistent with the experimental results observed for brittle materials.

[11] A. A. Griffith, *Proc. 1st Int'l. Congress in Appl. Mech.*, 1925, p. 55.

**McClintock–Walsh Criterion**

McClintock and Walsh[12] extended Griffith's criterion by considering a frictional component acting on the flaw faces that had to be overcome in order for the crack to grow. This term is a function of the applied stress. The frictional stress $f$ was considered equal to the product of the frictional coefficient $\mu$ and the normal stress $\sigma_0$ acting on the flaw surface. McClintock and Walsh assumed that there was a stress $\sigma_c$ at infinity necessary to close the flaw so that the opposite surfaces would touch each other. This approach led to the following expression:

$$\sigma_1[(\mu^2+1)^{1/2}-\mu]-\sigma_2[(\mu^2+1)^{1/2}+\mu] = 4\sigma_0\left(1+\frac{\sigma_c}{\sigma_0}\right)^{1/2}-2\mu\sigma_c. \tag{3.36}$$

Assuming that $\sigma_c = 0$, we get the following simple version of this criterion:

$$\sigma_1[(\mu^2+1)^{1/2}-\mu]-\sigma_2[(\mu^2+1)^{1/2}+\mu] = 4\sigma_0 \tag{3.37}$$

McClintock and Walsh's criterion is shown in Figure 3.31 for $\mu = 1$. Griffith's criterion is more conservative, and the compressive strength is 10 times the tensile strength for McClintock and Walsh. The frictional forces retard failure in compression.

## Example 3.9

Determine the fracture stress for SiC in compression in a complex loading situation in which $\sigma_1/\sigma_2 = 2$ if $\sigma_0$ in tension is 400 MN/m$^2$. Perform all calculations assuming (a) no friction between crack surfaces and (b) a friction coefficient of 0.5.

***Solution:*** Applying Equation 3.35 (with no friction), we have

$$\left(\sigma_1-\frac{\sigma_1}{2}\right)^2+8\times 400\left(\sigma_1+\frac{\sigma_1}{2}\right)=0,$$
$$\frac{\sigma_1}{4}+4{,}800=0,$$
$$\sigma_1=-19{,}200\text{ MPa},$$
$$\sigma_1=-19.2\text{ GPa}.$$

Applying Equation 3.37 (with friction), we obtain

$$\sigma_1[(0.5^2+1)^{1/2}-0.5]-0.5\sigma_1[(0.5^2+1)^{1/2}+0.5]=4\times 400,$$
$$\sigma_1(0.618)-\sigma_1(0.809)=1{,}600,$$
$$\sigma_1=\frac{-1{,}600}{0.272},$$
$$\sigma_1=-5.88\text{ GPa}.$$

The very high compressive strengths are due to the confinement. If the ceramic were not confined (i.e., if $\sigma_2 = 0$), the compressive strengths would be −3.2 GPa (Griffith) and −2.5 GPa (McClintock–Walsh).

[12] F. A. McClintock and J. B. Walsh, *Proc. 4th U.S. Nat'l. Cong. of Appl. Mech.* (1962), p. 1015.

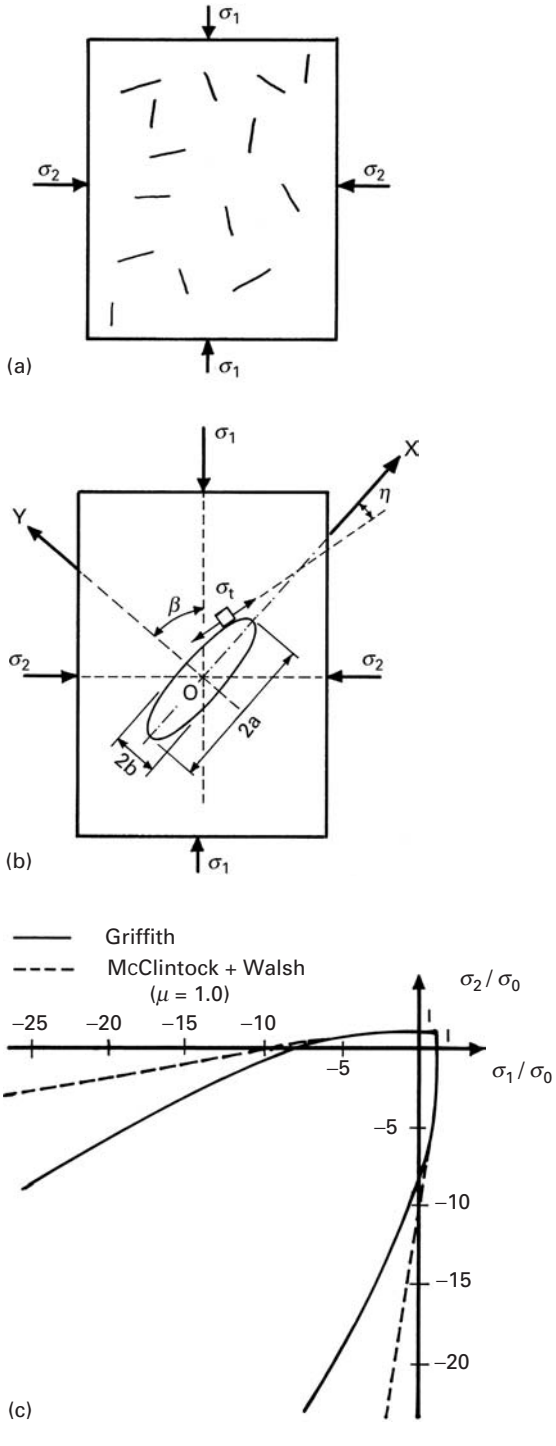


**Fig. 3.31** (a) Simple model for solid with cracks. (b) Elliptical flaw in elastic solid subjected to compression loading. (c) Biaxial fracture criterion for brittle materials initiated from flaws without (Griffith) and with (McClintock and Walsh) crack friction.

### 3.7.6 Yield Criteria for Ductile Polymers

Brittle polymers such as epoxies fail at the end of their linear elastic stage without any significant plastic deformation. Ductile polymers such as thermoplastics undergo plastic deformation. Does this mean that we can use the Tresca or von Mises criteria to describe their yielding? The answer is no, because, unlike the yield strength of metals, that of polymers depends on the hydrostatic component of stress. The Tresca and von Mises criteria, on the other hand, do not show any such dependence. This dependence on hydrostatic stress in polymers stems from the more liquidlike structure of polymers. Specifically, the polymers have some free volume, which makes them highly compressible.

Let us consider the von Mises criterion for isotropic metals. According to this criterion, yielding occurs when the condition

$$(\sigma_1 - \sigma_2)^2(\sigma_2 - \sigma_3)^2 + (\sigma_3 - \sigma_1)^2 \geq 6k^2 = \text{constant}$$

is satisfied, where $\sigma_1$, $\sigma_2$, and $\sigma_3$ are the principal stresses and $k$ is constant equal to the yield stress in torsion $\tau_0$. For metals, we take $k$ or $\tau_0$ to be a constant at room temperature, equal to $\sigma_0/\sqrt{3}$ for uniaxial stress, with $\sigma_0$ the uniaxial yield stress. This equation also implicitly assumes that the tensile and compressive yield strengths are numerically the same, equal to $\sqrt{3}k$ or $\sqrt{3}\,\tau_0$. It turns out that for polymers, yield stress in compression is greater than that in tension by 10 to 20%.[13] This stems from the fact that, again unlike yielding in metals, yielding in polymers shows a strong dependence on any superimposed hydrostatic pressure. That is,

$$k = k(\dot{\varepsilon},\ T,\ \sigma_p),$$

where $\dot{\varepsilon}$ is the strain rate, $T$ is the temperature, and $\sigma_p$ is the hydrostatic pressure. As we mentioned, in molecular terms, this dependence of yield stress on hydrostatic pressure can be traced to the fact that polymers have some *free volume* associated with them, which is diminished by hydrostatic compression. We can modify the yield criterion to take into account this dependence on the hydrostatic compressive stress $\sigma_p$ by using the expression

$$k = k_0 + A\sigma_p,$$

where $k_0$ is a constant and $A$ is another constant that represents the dependence of yield stress on hydrostatic pressure. As $\sigma_p$ increases, the free volume decreases, and molecular motion becomes more difficult. The presence of a hydrostatic component translates the von Mises ellipse from quadrant I to quadrant III, as shown in Figure 3.32. The yield envelopes for a polymer or metal that does not show yield stress dependence on the hydrostatic component is shown in Figure 3.32(a), while that for a polymer showing yield stress dependence on hydrostatic stress takes the shape shown in Figure 3.32(b). Note that

[13] K. Matsushige, S. V. Radcliffe, and E. Baer, *J. Polymer Sci., Polymer Phys.*, 14 (1976) 703.

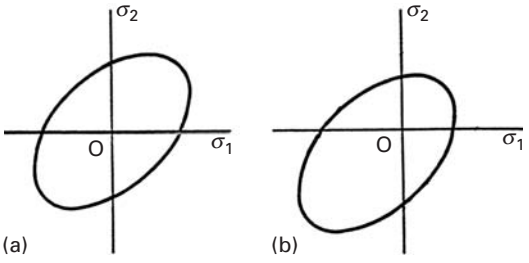


**Fig. 3.32** Translation of von Mises ellipse for a polymer due to the presence of hydrostatic stress. (a) No hydrostatic stress, (b) with hydrostatic stress.

crazing occurs only in tension, not in compression. The yield envelope in Figure 3.32(b) has been translated with respect to that in Figure 3.32(a).

Several glassy polymers, such as polystyrene, polycarbonate, and PMMA, show the phenomenon of crazing. (See Section 8.4.2.) Crazing involves the formation of microvoids and stretched chains or fibrils under tension. The fibril formation depends on shear flow and free volume. A yield criterion that takes crazing into account is

$$\sigma_1 - \sigma_2 = A + \frac{B}{(\sigma_1 + \sigma_2)},$$

where $(\sigma_1 - \sigma_2)$ represents the shear, $(\sigma_1 + \sigma_2)$ represents the hydrostatic component, and $A$ and $B$ are adjustable constants that depend on temperature. Note that as the hydrostatic component $(\sigma_1 + \sigma_2)$ increases, the shear stress $(\sigma_1 - \sigma_2)$ required for yielding decreases.

A better and more complete scenario for yielding in polymers is as follows. Under multiaxial stress, glassy polymers can undergo yielding by shear or crazing. Figure 3.33 shows schematically the yield envelope under a biaxial stress condition. The constants $A$ and $B$ can be chosen to fit the curve to experimental data. The pure-shear line, $\sigma_1 = -\sigma_2$, is the boundary between hydrostatic compression and hydrostatic tension. Below the pure-shear line, crazing (a void-forming process) does not occur because hydrostatic pressure reduces the volume. Above this line, crazing is the main mechanism of failure. The curves for crazing are asymptotic to the pure shear line. The yield envelope shown in the figure also shows the pressure-dependent shear yielding; that is, the envelope has been translated with respect to the conventional von Mises criterion. Note that in the first quadrant the crazing envelope is completely inside the shear yield envelope. This means that for all combinations of biaxial tensile stresses, crazing will precede shear yielding. In the second and fourth quadrants, the two envelopes intersect. The heavy line indicates the overall yielding or failure envelope.

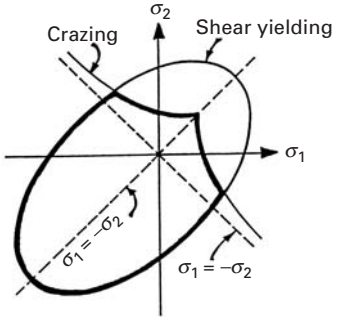


**Fig. 3.33** Envelopes defining shear yielding and crazing for an amorphous polymer under biaxial stress. (After S. S. Sternstein and L. Ongchin, *Am. Chem. Soc., Div. of Polymer Chem., Polymer Preprints*, 10 (1969), 1117.)

A word of caution is in order here. Crazing in *air* does not occur in pure shear or under conditions of compressive hydrostatic stress. The modified criterion just described requires a dilative component of the applied stress for crazing in air. In the presence of an appropriate environmental agent, crazing can be observed under conditions of simple tension and hydrostatic pressure.

### 3.7.7 Failure Criteria for Composite Materials

Unidirectionally aligned fiber reinforced composites are generally quite anisotropic in elastic constants as well as in strength. This, of course, stems from the fact that fibers generally are a lot stiffer and stronger than the matrix and the fact that the fibers are aligned in the matrix. Quite frequently, the strength in the longitudinal direction is as much as an order of magnitude greater than that in the transverse direction. We shall consider the case of laminated composites made by stacking plies of different orientations in an appropriate sequence. We assume that the fiber reinforced lamina is a homogeneous, orthotropic material. We use a continuum mechanics approach, i.e., we treat the fiber reinforced composite as a homogeneous material, i.e., its properties do not change from point to point. We do, however, consider the fiber reinforced composite to be an orthotropic material, i.e., the anisotropic nature of the composite is taken into account. There are many criteria available in the literature; for a summary, see Chawla[14]. Here, we describe one criterion, called *quadratic interaction criterion*, which is quite general and seems to work quite well for laminated composites made by stacking laminae of fiber reinforced composites in different orientations. The thickness of the individual lamina as well as the laminated composite is much smaller than either the length or width, which allows us to use plane stress condition to analyze the failure criterion. In practical terms, it means that we need to worry about the in-plane stress components, viz, two normal components, $\sigma_1$ and $\sigma_2$, and one in-plane shear component, $\sigma_{12}$. In the composite literature, it is customary to use symbol $\sigma_6$ for $\sigma_{12}$. Thus, the reader must keep in mind in what follows that $\sigma_6$ represents the in-plane shear component.

**Quadratic Interaction Criterion**

This criterion, a combination of linear and quadratic terms, takes into account the stress interactions. Tsai and Wu proposed this, a modification of the Hill theory, for a fiber reinforced composite laminate by adding some additional terms. According to this theory, the failure surface in stress space can be described by a function of the form

$$f(\sigma) = f_i\sigma_i + f_{ij}\sigma_i\sigma_j = 1 \quad i, j = 1, 2, 6 \tag{3.38}$$

where $f_i$ and $f_{ij}$ are the strength parameters. For the case of plane stress, $i, j = 1, 2, 6$ and we can expand Equation (3.38) as follows:

$$\begin{aligned} f_1 + \sigma_1 + f_2\sigma_2 + f_6\sigma_6 + f_{11}\sigma_l^2 + f_{22}\sigma_2^2 + f_{66}\sigma_6^2 \\ + 2f_{12}\sigma_1\sigma_2 + 2f_{12}\sigma_1\sigma_2 + 2f_{16}\sigma_1\sigma_6 + 2f_{26}\sigma_2\sigma_6 = 1 \end{aligned} \tag{3.39}$$

For an orthotropic lamina, it is important to distinguish between the signs of normal stresses, i.e., tensile or compressive. The linear stress terms provide for this difference. For the shear stress component, the sign reversal should be immaterial. Thus, terms containing the first degree shear stress must vanish in Equation (3.39). These

[14] K. K. Chawla, *Composite Materials*, 2nd ed. (New York: Springer-Verlag, 1998).

terms are $f_{66}\sigma_6$, $2f_{16}\sigma_1\sigma_6$, and $2f_{26}\sigma_2\sigma_6$. The stress components in general are not zero. Therefore, for these three terms to vanish we must have

$$f_{16} = f_{26} = f_6 = 0$$

Equation (3.39) is now simplified to

$$f_1\sigma_1 + f_2\sigma_2 + f_{11}\sigma_1^2 + f_{22}\sigma_2^2 + f_{66}\sigma_6^2 + 2f_{12}\sigma_1\sigma_2 = 1 \tag{3.40}$$

There are six strength parameters in Equation (3.40). We can measure five of these by the following simple tests.

**Longitudinal (Tensile and Compressive) Tests**
If $X_{1t}$ and $X_{1c}$ are the longitudinal tensile and compressive strengths, respectively, then we can write

$$f_1X_{1t} + f_{11}X_{1t}^2 = 1$$

and

$$-f_1X_{1c} + f_{11}X_{1c}^2 = 1.$$

From these two expressions, with two unknowns, we get

$$f_1 = \frac{1}{X_{1t}} - \frac{1}{X_{1c}}$$

and

$$f_{11} = \frac{1}{X_{1t}X_{1c}}.$$

**Transverse (Tensile and Compressive) Tests**
If $X_{2t}$ and $X_{2c}$ are the transverse tensile and compressive strengths, respectively, then proceeding as above, we get

$$f_2 = \frac{1}{X_{2t}} - \frac{1}{X_{2c}}$$

and

$$f_{22} = \frac{1}{X_{2t}X_{2c}}.$$

**Longitudinal Shear Test**
If $X_6$ is the shear strength, we have

$$f_{66} = \frac{1}{X_6^2}.$$

Thus, we can express all the failure strength parameters in Equation 3.40 except $f_{12}$ in terms of the ultimate intrinsic strength properties of the composite. $f_{12}$ must be evaluated by means of a biaxial test, which is not easy to do. In the absence of other data, we can take $f_{12} \cong -0.5(f_{11}f_{22})^{1/2}$. It turns out, however, that small changes in $f_{12}$ can significantly affect the predicted strength. Equation 3.40 describes the

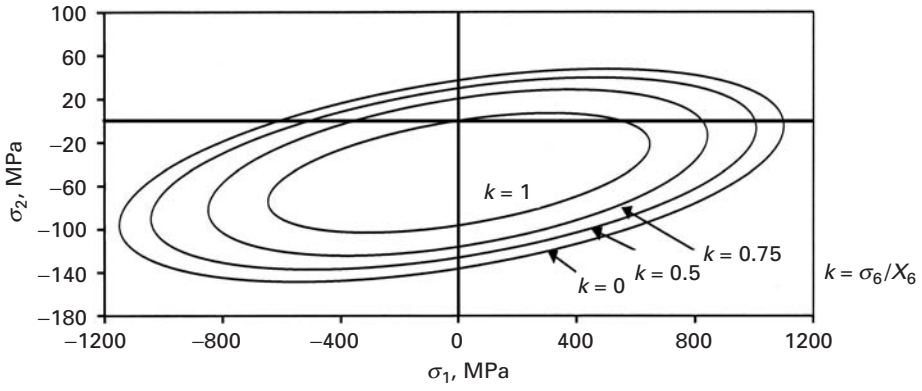


**Fig. 3.34** Failure envelope for unidirectional E-glass/epoxy composite under biaxial loading at different levels of shear stress. (After I. M. Daniel and O. Ishai, *Engineering Mechancis of Composite Materials* (New York: Oxford University Press, 1994), p. 121.)

failure envelope, a three-dimensional ellipsoid, in the $\sigma_1$, $\sigma_2$, and $\sigma_6$ space. For constant values of shear stress, $\sigma_6 = kX_6$, we shall have the failure envelope in the form of a two-dimensional ellipse described by the following equation:

$$f_1\sigma_1 + f_2\sigma_2 + f_{11}\sigma_1^2 + f_{22}\sigma_2^2 + f_{66}\sigma_6^2 + 2f_{12}\sigma_1\sigma_2 = 1 - k_2 \qquad (3.41)$$

Figure 3.34 shows schematically the failure envelopes under biaxial loading for a unidirectionally reinforced glass fiber/epoxy composite, for different values of $k$, where $k = \sigma_6/X_6$. Just as the name quadratic interaction indicates, the stress interaction is clear in all quadrants. The reader should note that the quadratic interaction criterion merely predicts the conditions of failure, it does not tell us anything about the mode of failure, i.e., fiber failure, interface failure in shear, etc.

### 3.7.8 Yield and Failure Criteria for Other Anisotropic Materials

Besides fiber reinforced composites, there are other anisotropic materials. The source of anisotropy in these materials can be one of the following.

- A single crystal can have different properties in different directions due to its inherent crystal symmetry.
- A cold-rolled sheet, tube, or wire of a metal or alloy can show a very high degree of preferred orientation of grains. Polymers are also frequently processed by drawing, extrusion, or injection molding techniques. Such techniques impart a high degree of anisotropy to the polymer. Figure 3.35 shows the change in shape of the yield surface as a function of anisotropy, where $R = \sigma_2/\sigma_1$. For $R = 1$, we have isotropy, and a classical von Mises curve is obtained.

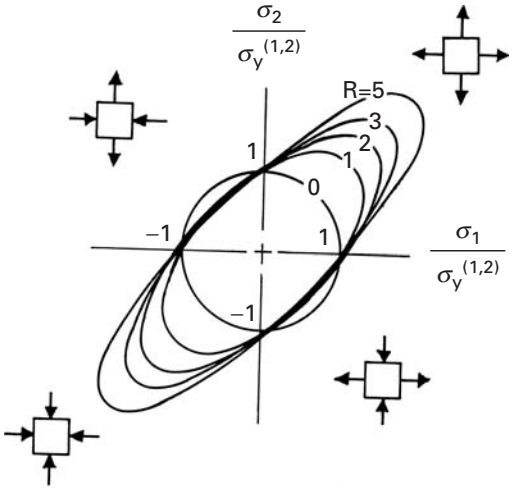


**Fig. 3.35** Plane-stress yield loci for sheets with planar isotropy or textures that are rotationally symmetric about the thickness direction, $x_3$. (Values of $R$ indicate the degree of anisotropy $= \sigma_2/\sigma_1$.)

While the most anisotropic crystal would render the plasticity treatment prohibitively complex, there is one type of anisotropy that can be studied without excessive complications. The type of response displayed by wood is a good illustration of this anisotropy. Wood has different yield stresses along the three directions defined by the wood fibers and by the normals to the fibers. Similarly, a rolled sheet or slab of metal will exhibit orthotropic plastic properties; the rolling direction, transverse direction, and thickness direction define the three axes.

## 3.8 Hardness

The simplest way of determining the resistance of a metal to plastic deformation is through a hardness test. Indentation tests constitute the vast majority of hardness tests. They are essentially divided into three classes, commonly called *nanoindentation*, *microindentation*, and *macroindentation* tests, but improperly referred to as microhardness and macrohardness tests. The division between micro and macro occurs for a load of approximately 200 gf (∼2 N). In nanoindentation testing, the load is of the order of mN. The indentation tests in metals measure the resistance to plastic deformation; both the yield stress and the work-hardening characteristics of the metal are important in determining the hardness. In spite of the theoretical studies done on hardness, hardness cannot be considered a fundamental property of a metal. Rather, it represents a quantity measured on an arbitrary scale.[15] Hardness measurements should not be taken

[15] M. C. Shaw, in *The Science of Hardness Testing and its Research Applications*, J. H. Westbrook and H. Conrad, eds. (Metals Park, OH: ASM, 1973), p. 1.

**Table 3.2** Approximate Hardness Conversions for Steels†

| Vickers HV | HB (Brinell) (10-mm ball, 3,000 kgf) | | Rockwell | | | | Rockwell Superficial | | Shore Sclero-scope | Approximate Tensile Strength (MPa) |
|---|---|---|---|---|---|---|---|---|---|---|
| | *Stand.* | *WC* | A (Brale 60 kgf) | B (1Brale 100 kgf) | C (Brale 150 kgf) | D (Brale 100 kgf) | 15N | 45N | | |
| 940 | | | 85.6 | | 68.0 | 76.9 | 93.2 | 75.4 | 97 | |
| 900 | | | 85.0 | | 67.0 | 76.1 | 92.9 | 74.2 | 95 | |
| 860 | | 757 | 84.4 | | 65.9 | 75.3 | 92.5 | 73.1 | 92 | |
| 820 | | 733 | 83.8 | | 64.7 | 74.3 | 92.1 | 71.8 | 90 | |
| 780 | | 710 | 83.0 | | 63.3 | 73.3 | 91.5 | 70.2 | 87 | |
| 740 | | 684 | 82.2 | | 61.8 | 72.1 | 91.0 | 68.6 | 84 | |
| 700 | | 656 | 81.3 | | 60.1 | 70.8 | 90.3 | 66.7 | 81 | |
| 660 | | 620 | 80.3 | | 58.3 | 69.4 | 89.5 | 64.7 | 79 | 2199 |
| 620 | | 582 | 79.2 | | 56.3 | 67.9 | 88.5 | 62.4 | 75 | 2061 |
| 580 | | 545 | 78.0 | | 54.1 | 66.2 | 87.5 | 59.9 | 72 | 1923 |
| 540 | 496 | 507 | 76.7 | | 51.7 | 64.4 | 86.3 | 57.0 | 69 | 1792 |
| 500 | 465 | 471 | 75.3 | | 49.1 | 62.2 | 85.0 | 53.9 | 66 | 1655 |
| 460 | 433 | 433 | 73.6 | | 46.1 | 60.1 | 83.6 | 50.4 | 62 | 1517 |
| 420 | 397 | 397 | 71.8 | | 42.7 | 57.5 | 81.8 | 46.4 | 57 | 1379 |
| 380 | 360 | 360 | 69.8 | | 38.8 | 54.4 | 79.8 | 41.7 | 52 | 1241 |
| 340 | 322 | 322 | 67.6 | | 34.4 | 51.1 | 77.4 | 36.5 | 47 | 1110 |
| 300 | 284 | 284 | 65.2 | | 29.8 | 47.5 | 74.9 | 31.1 | 42 | 972 |
| 260 | 247 | 247 | 62.4 | | 24.0 | 43.1 | 71.6 | 24.3 | 37 | 834 |
| 220 | 209 | 209 | | 95.0 | | | | | 32 | 696 |
| 200 | 190 | 190 | | 91.5 | | | | | 29 | 634 |
| 180 | 171 | 171 | | 87.1 | | | | | 26 | 579 |
| 160 | 152 | 152 | | 81.7 | | | | | 24 | 517 |
| 140 | 133 | 133 | | 75.0 | | | | | 21 | 455 |
| 120 | 114 | 114 | | 66.7 | | | | | | |
| 100 | 95 | 95 | | 62.3 | | | | | | |
| 85 | 81 | 81 | | 41 | | | | | | |

†Tables for other metals and alloys can be found in ASTM 140 (*Standard Hardness Conversion Tables for Metals*). Adapted with permission from E. R. Petty, in *Techniques of Metals Research*, Vol. 5, Pt. 2, R. F. Bunshah, ed. (New York: Wiley-Interscience, 1971), p. 180.

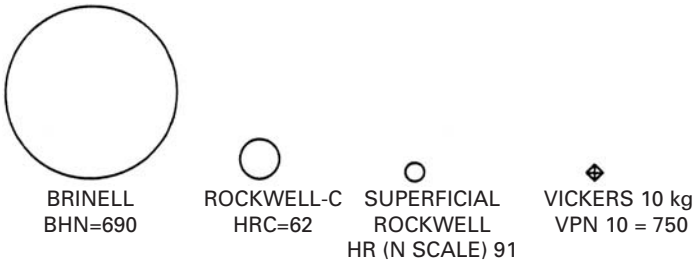


**Fig. 3.36** Comparison of the impression sizes produced by various hardness tests on material of 750 HV. BHN = Brinell hardness number, HRC = Rockwell hardness number on C scale, HRN = Rockwell hardness number on N scale, VPN = Vickers hardness number. (Adapted with permission from E. R. Petty, in *Techniques of Metals Research*, Vol. 5, Pt. 2, R. F. Bunshah, ed. (New York: Wiley-Interscience, 1971), p. 174.)

to mean more than what they are: an empirical, comparative test of the resistance of the metal to plastic deformation. Any correlation with a more fundamental parameter, such as the yield stress, is valid only in the range experimentally determined. Similarly, comparisons between different hardness scales are meaningful only through experimental verification. For steels, Table 3.2 gives a fair conversion of hardness and the tensile strength equivalents.

The most important macro-, micro-, and nanoindentation indentation tests are described in Sections 3.8.1–3.8.3.

## 3.8.1 Macroindentation Tests

The impressions caused by macroindentation tests are shown in Figure 3.36. The Brinell test produces by far the largest indentation. The Vickers test may produce very small indentations, depending on the load used.

**Brinell Hardness Test**

In this test, a steel sphere is pressed against a metal surface for a specified period of time (10 to 15 s, according to the ASTM), and the surface of the indentation is measured. The load (in kgf) divided by the area (in $mm^2$) of the curved surface gives the hardness HB, or

$$\boxed{\text{HB} = \frac{P}{\pi D \times \text{depth}}} \tag{3.42}$$

$$= \frac{2P}{\pi D(D - \sqrt{D^2 - d^2})}, \tag{3.43}$$

where $D$ and $d$ are the diameters of the sphere and impression, respectively. The parameters are indicated in Figure 3.37. Since $d = D \sin \phi$, we have

$$\text{HB} = \frac{2P}{\pi D^2(1 - \cos\phi)}. \tag{3.44}$$

Different spheres produce different impressions, and if we want to

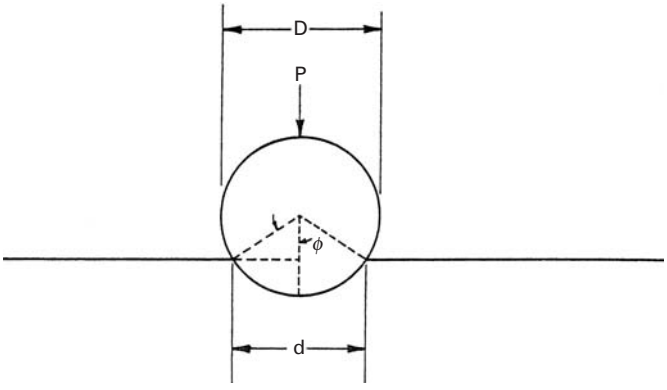


**Fig. 3.37** Impression caused by spherical indenter on metal plate.

maintain the same HB, independent of the size of the sphere, the load has to be varied according to the relationship

$$\frac{P}{D^2} = \text{constant}. \tag{3.45}$$

This assures the same geometrical configuration (the same $\phi$). The diameter of the impressions between $0.25D$ and $0.5D$ gives good, reproducible results. The target sought is $d = 0.375D$. If the same $d/D$ ratio is maintained (constant $\phi$), the Brinell test is reliable. Spheres with diameters of 1, 2, 5, and 10 mm have been used, and some of the ratios $P/D^2$ that provide good $d/D$ ratios for different metals are: steels and cast irons (30), Cu and Al (5), Cu and Al alloys (10), and Pb and Sn alloys (1). The softer the material, the lower is the $P/D^2$ ratio required to produce $d/D = 0.375$.

One of the problems of the Brinell test is that HB is dependent on the load $P$ for the same sphere. In general, HB decreases as the load is increased. ASTM standard E10–78 provides details and specifications for Brinell hardness tests. It states that the standard Brinell test is conducted under the following conditions:

Ball diameter: 10 mm
Load: 3000 kgf
Duration of loading: 10 to 15 s

In this case, 360 HB indicates a Brinell hardness of 360 under the foregoing testing conditions. For different conditions, the parameters have to be specified. For example, 63 HB 10/500/30 indicates a Brinell hardness of 63, measured with a ball of 10 mm diameter and a load of 500 kgf applied for 30 s. Brinell tables and additional instructions are provided in ASTM E10–78. Meyer[16] was aware of this problem and proposed a modification of the Brinell formula. He found out that the load divided by the *projected* area of the indentation ($\pi d^2/4$) was constant. Hence, he proposed, in place of Equation 3.42, the equation

$$\text{Meyer} = \frac{4P}{\pi d^2}, \tag{3.46}$$

[16] E. Meyer, *Z. Ver. Dtsch. Ing.*, 52 (1980) 645, 740, 835.

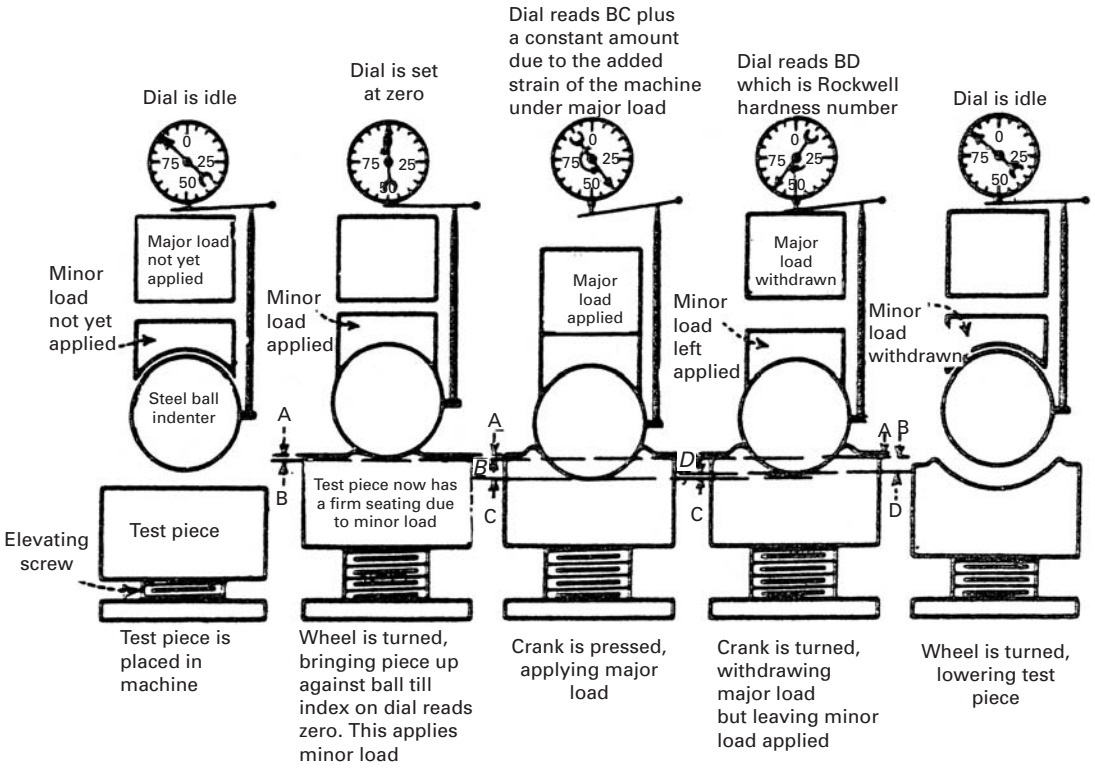


AB = Depth of hole made by minor load.
AC = Depth of hole made by major load and minor load combined.
DC = Recovery of metal upon withdrawal of major load. This is caused by elastic recovery of the metal under test, and does not enter the hardness reading.
BD = Difference in depth of holes corresponds to Rockwell hardness number.

**Fig. 3.38** Procedure in using Rockwell hardness tester. (Reprinted with permission from H. E. Davis, G. E. Troxel, and C. T. Wiscocil, *The Testing and Inspection of Engineering Materials*, (New York: McGraw-Hill, 1941), p. 149.)

where $P$ is expressed in kilograms force and $d$ in millimeters. The Meyer hardness never gained wide acceptance, in spite of being more reliable than the Brinell hardness. For work-hardened metals, it seems to be independent of $P$.

### Rockwell Hardness Test

The most popular hardness test is also the most convenient, since there is no need to measure the depth or width of the indentation optically. This testing procedure is illustrated in Figure 3.38. A preload is applied prior to the application of the main load. The dial of the machine provides a number that is related to the depth of the indentation produced by the main load. Several Rockwell scales are used, and the numbers refer to arbitrary scales and are not directly related to any fundamental parameter of the material. Two different types of indenters are used. The A, C, D, and N scales use the Brale indenter, which is a diamond cone with a cone angle of 120°. The other scales use either 1/8-in. (3.175-mm) or 1/16-in. (1.587-mm)-diameter steel spheres. The loads also vary, depending on the scale.

Table 3.3 Details of the More Important Scales Available for the Rockwell Hardness Tester

| Scale Designation | Type of Indenter | Major Load (kgf) | Typical Field of Application |
|---|---|---|---|
| A | Brale | 60 | The only continuous scale from annealed brass to cemented carbide, but is usually used for harder materials |
| B | 1.587 mm-diameter steel ball | 100 | Medium-hardness range (e.g., annealed steels) |
| C | Brale | 150 | Hardened steel > HRB100 |
| D | Brale | 100 | Case-hardened steels |
| E | 3.175 mm-diameter steel ball | 100 | Al and Mg alloys |
| F | 1.587 mm-diameter steel ball | 60 | Annealed Cu and brass |
| L | 6.35 mm-diameter steel ball | 60 | Pb or plastics |
| N | N Brale | 15, 30, or 45 | Superficial Rockwell for thin samples or small impressions |

Table 3.3 shows the various loads and typical applications. Usually, the C scale is used for harder steels and the B scale for softer steels; the A scale covers a wider range of hardness. Because of the nature of the measurement, any sagging of the test piece will produce changes in hardness. Therefore, it is of utmost importance to have the sample well supported; specimens embedded in Bakelite cannot be tested. The Brinell and Vickers tests, on the other hand, which are based on optical measurements, are not affected by the support.

For very thin samples, there is a special superficial Rockwell test. The testing procedure is described in detail in the ASTM Standard E18–74, and conversion tables for a number of alloys are given in ASTM Standard E140–78. The symbol used to designate this hardness is, according to the ASTM, HR; 64HRC corresponds to Rockwell hardness number 64 on the C scale.

The following precautions are recommended for reproducible results in Rockwell testing.[17]

1. The indenter and anvil should be clean and well seated.
2. The surface to be tested should be clean, dry, smooth, and free from oxide. A rough-ground surface is usually adequate for the Rockwell test.
3. The surface should be flat and perpendicular to the indenter.
4. Tests on cylindrical surfaces will give low readings, the error depending on the curvature, load, indenter, and hardness of the material. Corrections are given in ASTM E140–78.

[17] G. E. Dieter, *Mechanical Metallurgy*, 2nd ed. (New York: McGraw-Hill, 1976), p. 398.

5. The thickness of the specimen should be such that a mark or bulge is not produced on the reverse side of the piece. It is recommended that the thickness be at least 10 times the depth of the indentation. Tests should be made on only a single thickness of material.
6. The spacing between indentations should be three to five times the diameter of the indentation.
7. The speed of application of the load should be standardized. This is done by adjusting the dashpot on the Rockwell tester. Variations in hardness can be appreciable in very soft materials, unless the rate of application of the load is carefully controlled. For such materials, the operating handle of the Rockwell tester should be brought back as soon as the major load has been fully applied.

**Vickers (or Diamond Pyramid) Hardness Test**

This test uses a pyramidal indenter with a square base, made of diamond. The angle between the faces is 136°. The test was introduced because of the problems encountered with the Brinell test. One of the known advantages of the Vickers test is that one indenter covers all the materials, from the softest to the hardest. The load is increased with hardness, and there is a continuity in scale. The angle of 136° was chosen on the basis of results with spherical indenters. For these, the best results were obtained when $d/D = 0.375$. If we take the points at which the sphere touches the surface of the specimen and draw perpendiculars to the radii, their intersection will form an angle of 136°. This exercise is left to the student. The description of the procedures used in testing is given in ASTM Standard E92–72. The Vickers hardness (HV) is computed from the equation and is equal to the load divided by the area of the depression

$$\boxed{\text{HV} = \frac{2P\,\sin(\alpha/2)}{d^2} = \frac{1.8544P}{d^2},} \tag{3.47}$$

where $P$ is the applied load (in kgf), $d$ is the average length of the diagonals (in mm), and $\alpha$ is the angle between the opposite faces of the indenter (136°). Conversion to MPa is accomplished by multiplying this value by 9.81. The Vickers test described by ASTM E92–72 uses loads varying from 1 to 120 kgf. For example, 440HV30 represents a Vickers hardness number of 440, measured with a load of 30 kgf. Vickers testing requires a much better preparation of the material's surface than does Rockwell testing; hence, it is more time-consuming. The surface has to be ground and polished, care being taken not to work-harden it. After the indentation, both diagonals of impression are measured, and their average is taken. If the surface is cylindrical or spherical, a correction factor has to be introduced. ASTM Standard E92 (Tables 4 through 6) provide correction factors. As with other hardness tests, the distance between the indentations has to be greater than two-and one-half times the length of the indentation diagonal, to avoid interaction between the work-hardening regions.

The manner in which the material flows and work-hardens (or work-softens) beneath the indenter affects the shape of the impression. The sides of the square impression can be deformed into concave or convex curves, depending on the nature of the deformation process, and this results in reading errors.

**Relationships Between Yield Stress and Hardness**

For non-work-hardening materials, one has (this will be derived in Example 3.10):

$$\boxed{H = 3\sigma_y.} \tag{3.48}$$

Since there is a lot of plastic deformation under the indenter, in work-hardening materials we cannot use $\sigma_y$. Tabor[18] gives the following equation for the mean plastic strain under the indenter:

$$\varepsilon_p = \frac{d'}{5D},$$

where $d'$ is the diameter at the top of the pileup and $D$ is the diameter of the indenter. For $d'/D = 0.375$, a reasonable value for indentation, the plastic strain, $\varepsilon_{\mathrm{p}} = 0.075$. Hence, for work-hardening metals one should take the flow stress at a plastic strain of 0.375 before multiplying it by 3 for a good correlation with the hardness.

### 3.8.2 Microindentation Tests

Microindentation hardness tests — or microhardness tests — utilize a load lighter than 200 gf, and very minute impressions are thus formed; a load of 200 gf produces an indentation of about 50 $\mu$m for a medium-hardness metal. These tests are ideally suited to investigate changes in hardness at the microscopic scale. One can measure the hardness of a second-phase particle and identify regions within a grain where differences in hardness occur. Microhardness tests are also used to perform routine tests on very small precision components, such as parts of watches.

The results shown in Figure 3.39 illustrate well an application of microindentation testing. When a metal is alloyed, the distribution of the solute is not even throughout the grain, due to the stress fields produced by the solute atom. (See Chapter 7.) The solute atoms often tend to segregate at the grain boundaries. Figure 3.39(a) shows how the addition of aluminum to zinc is reflected by an increase in the hardness in the grain-boundary region, and the addition of gold results in a lowering of the grain-boundary hardness. This effect can be noted at extremely low concentrations of solute (a few parts per million). Figure 3.39(b) shows how this "excess" hardening increases with the concentration of aluminum.

In spite of the attempts made, several problems have arisen in the standardization of microindentation testing and its extrapolation to macroindentation results. There are several reasons for this.

[18] D. Tabor, *The Hardness of Metals*, (Oxford: Oxford Univesity Press, 1951).

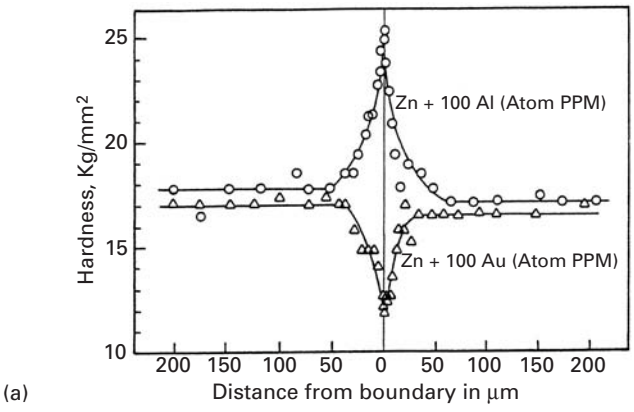


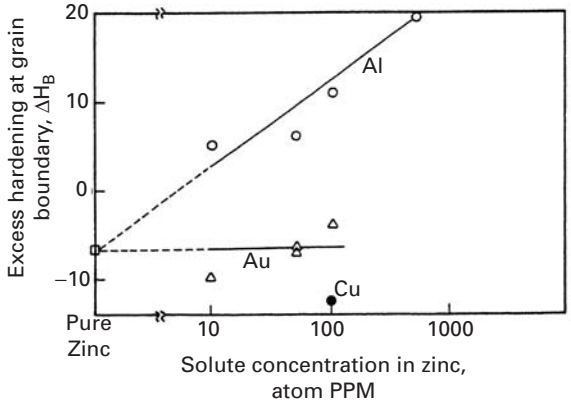


**Fig. 3.39** (a) Hardness–distance profiles near a grain boundary in zinc with 100-atom ppm of Al and zinc with 100-atom ppm of Au (1-gf load). (b) Solute concentration dependence of percent excess boundary hardening in zinc containing Al, Au, or Cu (3-gf load). (Adapted with permission from K. T. Aust, R. E. Hanemann, P. Niessen, and J. H. Westbrook, *Acta Met.*, 16 (1968) 291.)

First, almost invariably, the microhardness of any material is higher than its standard macrohardness. Additionally, the microhardness varies with load. Second, there is a tendency for the microhardness to increase (up to a few grams); then the hardness value drops with load. At very low loads, one is essentially measuring the hardness of a single grain; the indenter "sees" a single crystal, and the plastic deformation produced by the indentation is contained in this grain. As the load is increased, plastic deformation of adjoining grains is involved, and a truly polycrystalline deformation regimen is achieved. As we know well (see Chapter 5), the grain size has a marked effect on the yield strength and work-hardening characteristics of metals. Yet another source of error is the work-hardening introduced in the surface by polishing. The effect of crystallographic orientation, when the impression is restricted to a single grain, is of utmost importance. It is well known that both the yield stress and the work-hardening are dependent on the crystallographic orientation of the material. The Schmid law relates the applied stress to the shear stress "seen" by the various slip systems. The Schmid relation is discussed in Section 6.2.2.

The two most common microindentation tests are the Knoop and Vickers tests. The Knoop indenter is an elongated pyramid, shown in

Figure 3.40. The hardness is obtained from the surface area of the impression and is given by

$$\text{KHN} = \frac{14.228P}{L^2}, \tag{3.49}$$

where $P$ is the load of kgf and $L$ is the length of the major diagonal, in mm. The ratio between the dimensions of the impression is

$$h/W/L = 1 : 4.29 : 30.53.$$

This results in an especially shallow impression, making the technique very helpful for testing brittle materials. Indeed, that was the purpose of introducing the test. The ratio between the major and minor diagonal of the impression is approximately 7:1, resulting in a state of strain in the material that can be considered to be plane strain; the strain in the $L$ direction may be neglected. This subject is treated in Section 3.3. The very shallow Knoop impression is also helpful in testing thin components, such as electrodeposits or hardened layers. The Vickers microhardness test uses the same 136° pyramid with loads of a few grams. Both Knoop and Vickers indenters require prepolishing of the surface to a microscopic grade.

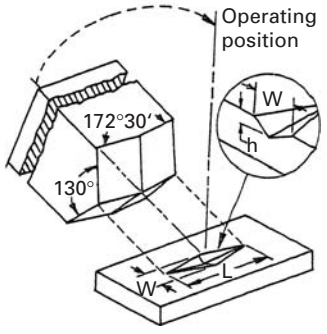


**Fig. 3.40** Some of the details of the Knoop indenter, together with its impression.

## Example 3.10 | (Inspired by M. F. Ashby and D. R. H. Jones)

Obtain, for a simple two-dimensional case, a relationship between the hardness $H$ and flow stress $\sigma_0$ of a material.

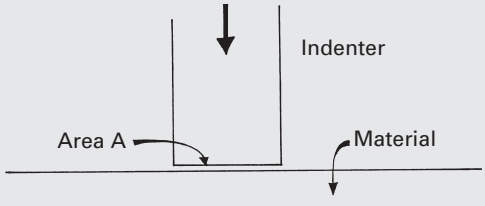


**Fig. E.3.10.1**

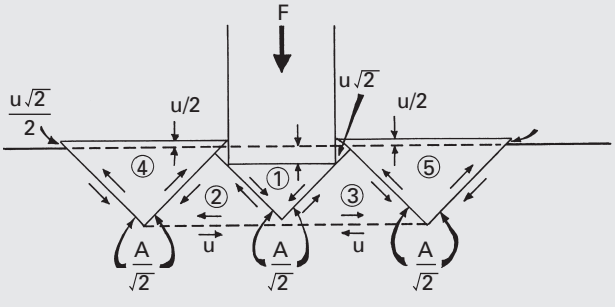


**Fig. E.3.10.2**

***Solution:*** We assume a flat indenter and deformation on one plane only, as shown in Figure E.3.10.1. Deformation is assumed to occur by the movement of blocks. We assume a total displacement $u$ of the punch, shown in Figure E.3.10.2. Block ① moves down by $u$. Blocks ② and ③ move sideways by $u$. Blocks ④ and ⑤ are pushed upward by $u/2$ and we compute the forces on two of their surfaces. The shear yield strength is $\tau_0$. We set the work done by the punch, $Fu$, equal to the energy dissipated at the various interfaces. Student should compute the areas of triangles and assume that the resistance to motion is $\tau_0$. The frictional forces between blocks is $\tau_0$ times the areas ($A$ or $A/\sqrt{2}$). We have

$$F u = 2 \times \frac{A\tau_0}{\sqrt{2}} \times u\sqrt{2} + 2 \times A\tau_0 \times u + 4 \times \frac{A\tau_0}{\sqrt{2}} \times \frac{u\sqrt{2}}{2},$$

$$| \leftarrow (\text{block } 1) \rightarrow || \leftarrow (\text{blocks } 2, 3) \rightarrow || \leftarrow (\text{block } 4, 5) \rightarrow |$$

central triangle  two lateral triangles  two end triangles

where F is the applied force, $u$ is the displacement of the punch, and $A$ is the area of the indentation (Figure E.3.10.1).

$$F u = u 6 A \tau_0,$$

$$\frac{F}{A} = 6\tau_0.$$

But $\tau_0 = \sigma_0/2$; hence,

$$\boxed{\frac{F}{A} = H = 3\sigma_0.}$$

This is, indeed, Equation 3.48. Thus, the derivation above is a proof for Equation 3.48.

## Example 3.11

Estimate the flow stress of the material shown in Figure E.3.11 if the indentation was done with a load of 1,000 g and the magnification of the photograph is 100×.

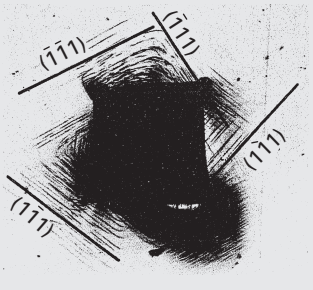


**Fig. E.3.11** Indentation into iron-nickel single crystal; notice {111} traces of slip planes with specimen surface.

***Solution:*** This is a Vickers microindentation. We measure the sides of the square, which are more visible (in this case) than the diagonal:

$$a = \frac{26 + 28}{2} = 27 \text{ mm}.$$

The diagonal is $d = a\sqrt{2} = 38.2$ mm. Dividing this value by the magnification, we obtain $d' = 0.382$ mm. So

$$H = \frac{1.8544P}{d^2} = \frac{1.8544}{0.145},$$

$$H = 12.80\,\text{kg/mm}^2.$$

We will convert this value to a yield stress, assuming that the material does not work-harden. We have (see Example 3.10)

$$H = 3\sigma_0, \quad \text{so} \quad \sigma_y = 4.25\,\text{kg/mm}^2.$$

But 1 kg/mm$^2$ $= 9.8 \times 10^6$ Pa; thus,

$$\sigma_y = 41.8\,\text{MPa}.$$

### 3.8.3 Nanoindentation

An instrumented indentation test, the apparatus for which is sometimes called a *nanoindenter*, was developed in the last quarter of the twentieth century, and is readily available commercially. The instrument is essentially a computer-controlled depth-sensing indentation system that allows extremely small forces and displacements to be measured. Very small volumes of a material can be studied and local characterization of microstructural features such as grain boundary regions, coatings, or reinforcement/matrix interface can be obtained. It can be regarded as a general microstructural investigation technique.

A schematic of a nanoindenter apparatus is shown in Figure 3.41. Commonly, a triangular pyramid or Berkovich indenter is used,

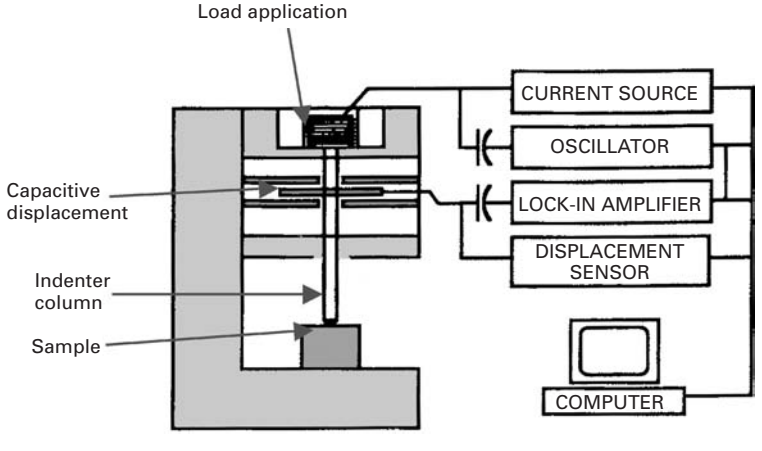


**Fig. 3.41** A schematic of a nanoindenter apparatus.

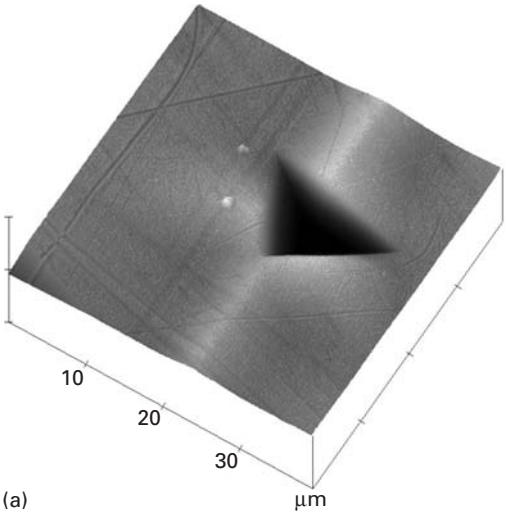


(a)

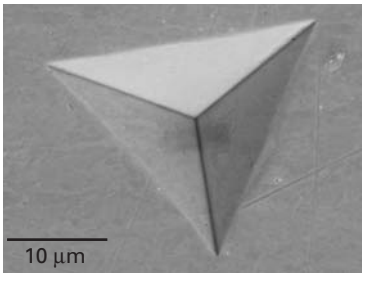


(b)

**Fig. 3.42** An impression made by means of Berkovich indenter in a copper sample. (From X. Deng, M. Koopman, N. Chawla, and K. K. Chawla, *Acta Mater.*, 52 (2004) 4291.) (a) An atomic force micrograph, which shows very nicely the topographic features of the indentation on the sample surface. The scale is the same along the three axes. (b) Berkovich indentation as seen in an SEM.

although other types of indenters can also be used. An impression made by means of Berkovich indenter in a copper sample is shown in Figure 3.42. Figure 3.42(a) is an atomic force micrograph, which shows very nicely the topographic features of the indentation on the sample surface, while Figure 3.42(b) shows a view of the indentation as seen in an SEM micrograph. The penetration of the indenter into the specimen is measured by a very sensitive capacitance gage. The resolution of the applied load may be less than 50 nN while displacement resolutions can be $<0.02$ nm. Remote position control is done by means of a joystick (motorized in *x*-, *y*-, and *z*- directions).

Generally, a series of load/unload curves is obtained, Figure 3.43. A nanoindenter records the total penetration of an indenter into the sample. The indenter may be moved toward the sample or away from the sample by means of a magnetic coil assembly. One can measure the hardness or elastic modulus of a phase in a material. As the indenter penetrates the specimen, the indentation load and displacement are recorded continuously during a load/unload cycle. The maximum load and the corresponding displacement are calculated from the plastic depth of the indentation. The hardness, $H$, is given by

$$H = P_{max/A},$$

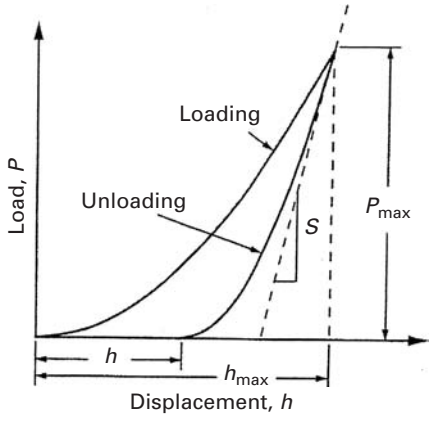


**Fig. 3.43** A schematic representation of load vs. indenter displacement.

where $P_{max}$ is the load and $A$ is the projected area of contact at peak load. The contact area at the peak load is determined by the geometry of the indenter and the depth of contact, $h_c$. Assuming that the indenter does not deform significantly, we can write $A = f(h_c)$. The form of function $f$ must be established experimentally. The area $A$ can be calculated by means of the following expression:

$$A = a + bh_i^{1/2} + ch_i + dh_i^{3/2} + 24.56h_i^2 \tag{3.50}$$

where $h_i$ is the plastic depth of the indentation and $a$, $b$, $c$, and $d$ are adjustable coefficients. For a perfect tip, $a = b = c = d = 0$, and the only coefficient is 24.56.

The stiffness, $S$, can be obtained from the load, $P$ vs. penetration depth, $h$ by the following expression relating the reduced modulus, $E_r$, the contact area $A$, and the stiffness, $S$:[19,20,21]

$$S = dP/dh = (2/\sqrt{\pi})E_r\sqrt{A}.$$

The reduced modulus $E_r$ of indenter–sample combination takes into account the fact that elastic deformation under load occurs in the sample as well as in the indenter. The reduced modulus is given by

$$E_r = (1 - \nu_i^2)/E_i + (1 - \nu_s^2)/E_f$$

where $E_i$ and $E_s$ are the Young's moduli, and $\nu_i$ and $\nu_s$ are the Poisson's ratio of the indenter and sample, respectively. The initial unloading slope gives us the reduced modulus provided one can measure the contact area at the peak load.

Modulus and hardness of a material can be obtained more accurately by measuring contact stiffness throughout the test. This technique is called continuous stiffness measurement (CSM). In this technique, a small harmonic force is superimposed on the primary load, $P$. This technique enables the instrument to determine the contact stiffness throughout the experiment. The displacement of the

[19] M. F. Doerner and W. D. Nix, *J. Mater. Res.*, 1 (1986) 601.
[20] W. C. Oliver, *MRS Bull.*, 11 (1985) 15.
[21] W. C. Oliver and G. M. Pharr, *J. Mater. Res.*, 7 (1992) 1564.

indenter at the excitation frequency and the phase angle between force and displacement are measured continuously as a function of depth. The stiffness, $S$, is given by the following relationship:

$$S = \left[ \frac{1}{\frac{P_{os}}{h_{(\omega)}} \cos \Phi - (K_s - m\omega^2)} - {K_f}^{-1} \right]^{-1} \tag{3.51}$$

where $P_{os}$ is the magnitude of the force oscillation, $h_{(\omega)}$ is the magnitude of the resulting displacement oscillation, $\omega$ is the frequency of the oscillation, $\Phi$ is the phase angle between the force and displacement, $K_s$ is the spring constant of the leaf springs that support the indenter, $K_f$ is the stiffness of the indenter frame, $C_f$ is the compliance of the load frame, and $m$ is the mass of the indenter.

The nanoindentation technique has been successfully used to measure the interfacial strength in a variety of fiber reinforced composites.[22]

## Example 3.12

A copper specimen was tested in a commercial nanoindentation machine. A Berkovich indenter (pyramid with triangular base) was used. The specimen was loaded to different load levels shown in Figure E.3.12, then unloaded. For each maximum load, determine the hardness. Establish whether the hardness changes with depth of indentation.

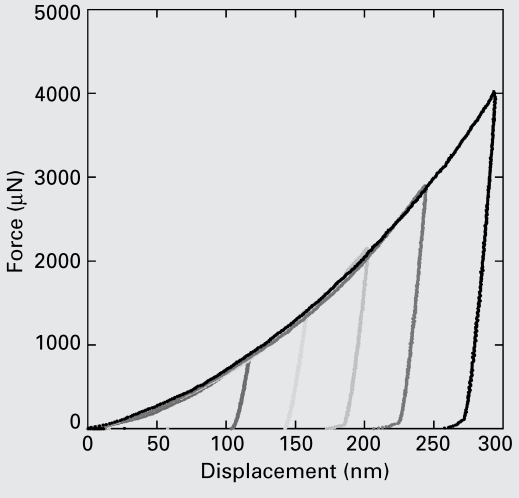


**Fig. E.3.12** Load vs. displacement curves obtained for copper specimen in a TriboIndenter machine. (Courtesy of Andrea Hodge, USC.)

[22] K. K. Chawla, *Ceramic Matrix Composites*, 2nd ed. (Boston: Kluwer Academic Publishers, 2003), p. 176.

***Solution:*** The relationship between depth of indentation, $h_i$, and area of a perfectly sharp Berkovich tip, is (Equation 3.50):

$$A = 24.56h_i^2$$

We find the forces and displacements at the top of the five loading cycles. We obtain the corresponding displacements (depths of indentation).

| Load, $P$ (μN) | Displacement, $h$ (nm) | Area, $A$ (nm$^2$) | Hardness (GPa) |
|---|---|---|---|
| 760 | 115 | 324,012 | 2.34 |
| 1350 | 165 | 667,012 | 2.02 |
| 2150 | 205 | 1,029,612 | 1.99 |
| 2850 | 243 | 1,446,700 | 1.97 |
| 3900 | 295 | 2,132,112 | 1.83 |

There is a slight but consistent decrease in nanoindentation hardness as the load is increased.

## 3.9 Formability: Important Parameters

*Deep drawing* and *stretching* are the two main processes involved in most sheet-metal-forming operations. An excellent introductory overview on sheet-metal forming is provided by Hecker and Ghosh.[23] In a stamping operation, one part of the blank might be subjected to a deformation process similar to deep drawing (thickness increasing with time). In deep drawing the material is required to contract circumferentially, while in stretching the stresses applied on the sheet are tensile in all directions. Sheet-metal forming has evolved from an art into a science, and important material parameters have been identified. These material properties are obtained in special tests and allow a reasonable prediction of the blank in the actual sheet-forming operation.

The work-hardening rate $n$ is important, because it determines the onset of necking (tensile instability), an undesirable feature. According to Considère's criterion (see Section 3.2.2), $n$ is equal to $\varepsilon_u$, the uniform strain. Hence, the higher $n$, the higher $\varepsilon_u$. The strain-rate sensitivity $m$ is an important parameter, too, because it also helps to avoid necking. If $m$ is positive, the material becomes stronger at incipient necks because the strain rate in the necked region is higher. (See Section 3.2.3.) The parameter $R$ (the through-thickness plastic anisotropy) is also important; it is equal to the ratio between the strain in the "stretching" direction and the strain in the thickness direction. The greater the resistance to "thinning" in stretching, the better is the formability of the metal. This resistance to thinning corresponds

[23] S. S. Hecker and A. K. Ghosh, *Sci. Am.*, Nov. (1976), p. 100.

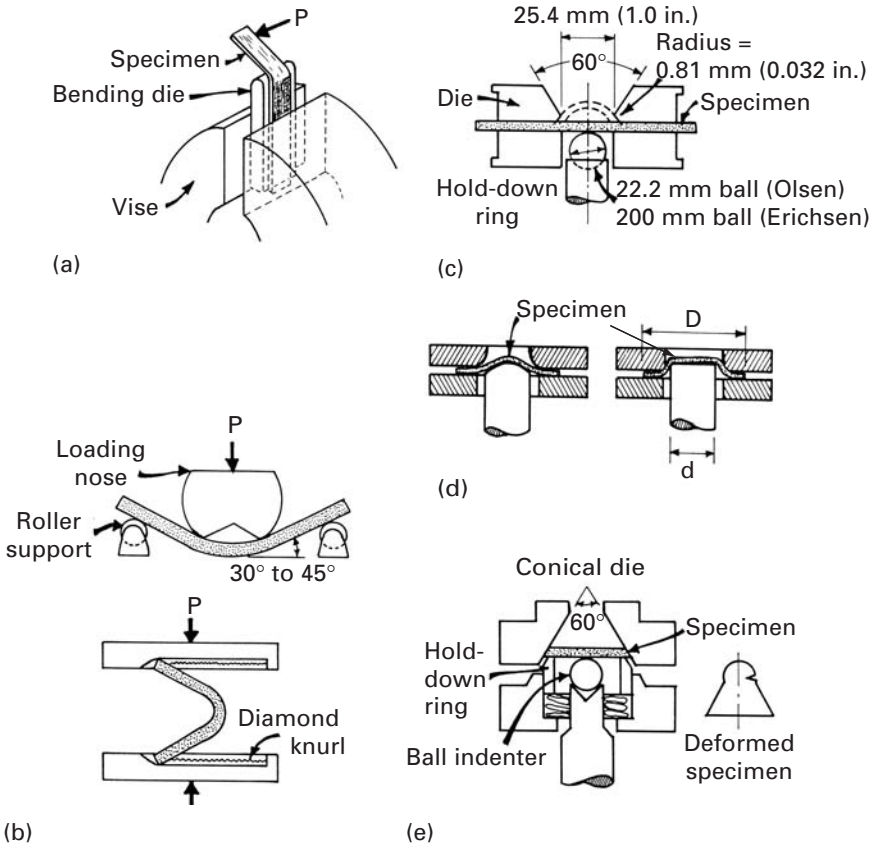


**Fig. 3.44** Simple formability tests for sheets. (a) Simple bending test. (b) Free-bending test. (c) Olsen or Ericksen cup test. (d) Swift cup test. (e) Fukui conical cup test.

to a value of $R$ larger than 1: the strength in the thickness direction is greater than the strength in the plane of the sheet. The three parameters $n$, $m$, and $R$ are readily obtained in a tensile test. (See Sections 2.2 and 3.2).

Additional important information on the workability of sheets is provided by the yield and flow loci. Section 3.7.8 gives a description of yield criteria and how they are graphically presented in a plane-stress situation. The experimental determination of the yield locus and its expansion as plastic deformation takes place is conducted in biaxial tests. (See Section 3.7.4, Figure 3.28.)

Figure 3.44 shows the most simple formability tests applied to metals. In the simple bending test, the specimen is attached to a die, and one end is clamped in a vise. The other end is bent to a specific radius. Specimens are bent to 180° using bending dies with smaller and smaller bending radii. Observations are made to see whether cracks are formed. In the free-bending test, the specimen is first bent between two rollers until an angle between 30° and 45° is achieved. It is then further bent between two grips, such as a vise.

The Olsen and Erichsen tests are typical stretch tests. A hardened steel sphere (diameter of 22.2 mm for the Olsen test, 20 mm for the Erichsen test) is pushed into the clamped metal, forming a bulge.

The depth of the bulge at the fracture point is measured. The clamp-down pressure is very high (>70 kN), to minimize the drawing of the material.

The Swift and Fukui tests (Figure 3.44(d) and (e)) are drawing tests. The clamp-down pressure in the Swift test allows the sheet to slip inward. The overall diameter of the part is decreased in the process. This test simulates the deep drawing of parts. The drawability is expressed as the limiting draw ratio

$$\text{LDR} = \frac{\text{maxmimum blank diameter}}{\text{punch diameter}} = \frac{D}{d}.$$

There are two geometries for the Swift test, shown in Figure 3.44(d): the round-bottomed cup test and the cup test. The latter test causes stretching of the center of the cup in addition to drawing. The Fukui test (Figure 3.44(e)) is the Japanese (JIS Z 2249) equivalent of the US stretch-drawing Swift test. A sphere 12.5 to 27 mm in diameter is pushed into a disk and advanced until either failure results or necking occurs in the cup. A hold-down ring maintains the specimen in place. The ratio between the diameters of the base of the deformed cup and the original disk provides the Fukui conical cup value. The modern counterpart of these older, but reliable, tests is the forming-limit curve, described in Section 3.9.2. The circle-grid analysis, which consists of applying a circle grid to the blank and measuring the strains in the critical regions of the stamped part, is also described in that section.

### 3.9.1 Plastic Anisotropy

Elastic deformation under anisotropic conditions is described by elastic constants, whose number can vary from 21 for the most anisotropic solid to 3 for one exhibiting cubic symmetry. (For isotropic solids, the number of independent elastic constants is 2.) In a similar way, plasticity increases in complexity as the anisotropy of the solid increases. Sections 3.2–3.3 cover only the isotropic case, and even that in a very superficial way. In polycrystals, anisotropy in plasticity is more the rule than exception. Essentially, there are two sources of anisotropy. First is texture, in which the grains are not randomly oriented, but have one or more preferred orientations. Texturing is often introduced by deformation processing. Well-known and well-characterized textures accompany cold rolling, wire drawing, and extrusion. This type of anisotropy is also called *crystallographic anisotropy*. Second, anisotropy is produced by the alignment of inclusions or second-phase particles along specific directions. When steel is produced, the inclusions existing in the ingot take the shape and orientation of the deformation process (rolling). These inclusions, such as MnS, produce mechanical effects called fibering. This type of anisotropy is also known as *mechanical anisotropy*. Whereas crystallographic anisotropy can strongly affect the yield stress, mechanical anisotropy usually manifests itself only in the later stages of deformation, influencing fracture.

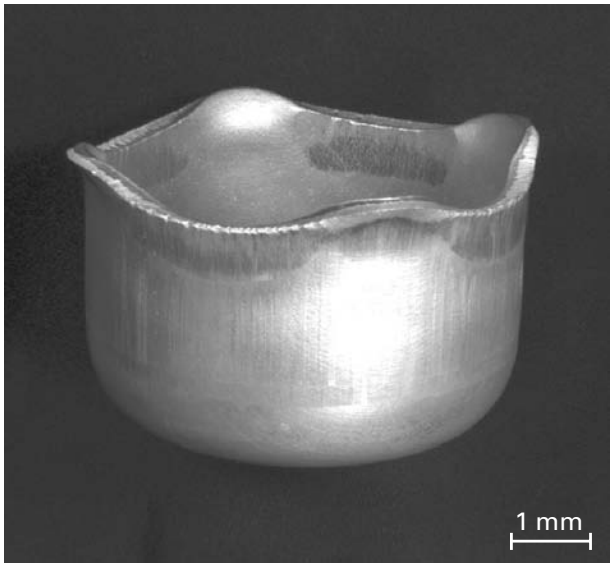


**Fig. 3.45** "Ears" formed in deep-drawn cups due to in-plane anisotropy. (Courtesy of Alcoa, Inc.)

Figure 3.45 shows the effect of texture on a deep-drawn cup. This effect is known as "earing." Prior to drawing, the sheet exhibited different yield stresses along different directions. The orientation in which the sheet is softer is drawn in faster than the harder direction, resulting in "ears." The number of ears (four) actually shows the type of texture. Figure 3.46 on the other hand, illustrates the effect of inclusions on the formability of an alloy. Fracture is much more probable if the sheet is bent along the second-phase strings than if it is bent perpendicular to them.

Section 3.7.8 shows the yield locus for anisotropic materials; this equation is an ellipse essentially identical to that described by the von Mises yield criterion in plane stress. (See Section 3.7.4.) The ellipse is distorted, however.

### 3.9.2 Punch–Stretch Tests and Forming-Limit Curves (or Keeler–Goodwin Diagrams)

An ideal test is the one that predicts exactly the performance of a material. The $m$, $n$, and $R$ values are insufficient to predict the formability, and tests more closely resembling the actual plastic-forming operations have been used for a long time. The main parameter that they can provide is the strain to fracture. These tests are called punch–stretch tests, or simply, "cupping" tests.

The punch–stretch test consists of clamping a blank firmly on its edges between two rings or dies; the next step is to force a plunger or punch through the center area of the specimen enclosed by the area of the ring, until the blank fractures. Several punch–stretch tests have been developed over the years, including the Olsen, Erichsen, Guillery, and Wazau tests. These "cupping" tests are routinely used for inspection purposes, since they provide a quick indication of ductility;

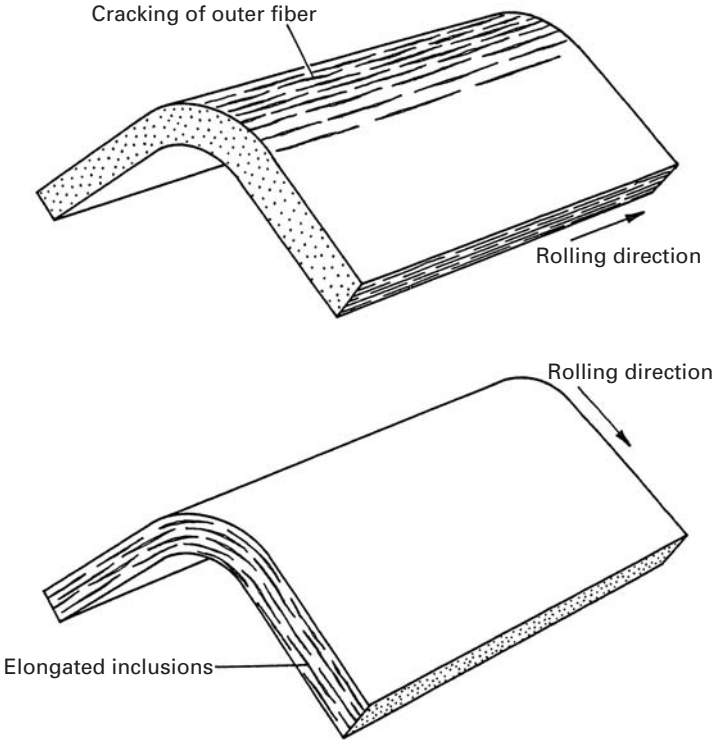


**Fig. 3.46** Effect of "fibering" on formability. The bending operation is often an integral part of sheet-metal forming, particularly in making flanges so that the part can be attached to another part. During bending, the fibers of the sheet on the outer side of the bend are under tension, and the inside ones are under compression. Impurities introduced in the metal as it was made become elongated into "stringers" when the metal is rolled into sheet form. During bending, the stringers can cause the sheet to fail by cracking if they are oriented perpendicular to the direction of bending (top). If they are oriented in the direction of the bend (bottom), the ductility of the metal remains normal. (Adapted with permission from S. S. Hecker and A. K. Ghosh, *Sci. Am.*, Nov. (1976), p. 100.)

they also show the change in surface appearance of the sheet upon forming. Two important defects appear in stamping:

1. The orange-peel effect (surface rugosity) is due to the large grain size of the blank. The anisotropy of plastic deformation of the individual grains results in an irregular surface, perfectly visible to the naked eye, when the grain size is large.
2. Stretcher strains are produced when Lüders bands appear in the forming process. The interface between the Lüders band and undeformed materials exhibits a step easily visible to the naked eye. This is an undesirable feature that can be eliminated either by prestraining the sheet prior to forming (beyond the Lüders band region) or by alloying the material in such a way as to eliminate the yield drop and plateau from the stress–strain curve. In low-carbon steels, Lüders bands are formed by the interactions of carbon and

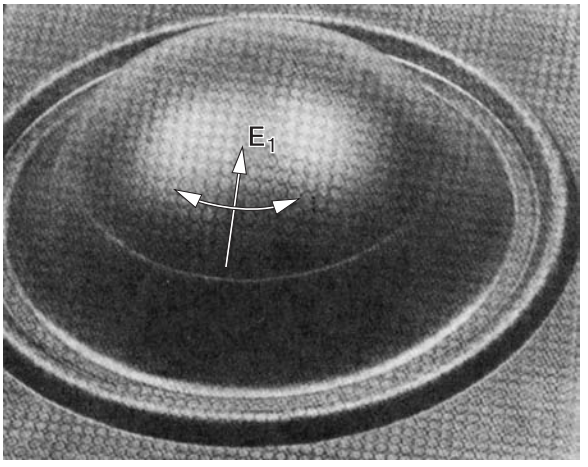


**Fig. 3.47** Sheet specimen subjected to punch–stretch test until necking; necking can be seen by the clear line. (Courtesy of S. S. Hecker.)

nitrogen atoms with dislocations. After a process called temper rolling, the susceptibility is eliminated; however, it can return following aging. This problem is easily solved by flexing the sheet by effective roller leveling just prior to forming.[24]

The poor correlation between the common "cupping" test and the actual performance of the metal led investigators to look at some more fundamental parameters. The first breakthrough came in 1963, when Keeler and Backofen[25] found that the localized necking required a critical combination of major and minor strains (along two perpendicular directions in the sheet plane). This concept was extended by Goodwin to the negative strain region, and the resulting diagram is known as the Keeler–Goodwin,[26] or forming-limit, curve (FLC). The FLC is an important addition to the arsenal of techniques for testing formability and is described after the description of Hecker's testing technique, presented next.[27]

Hecker developed a punch–stretch apparatus and technique well suited for the determination of FLC. The device consists of a punch with a hemispherical head with a 101.6-mm (4-in.) diameter. The die plates are mounted in a servohydraulic testing machine with the punch mounted on the actuator. The hold-down pressure on the die plates (rings) is provided by three hydraulic jacks. (The hold-down load is 133 kN.) The bead-and-groove arrangement in the rings eliminates any possible drawing in. The specimens are all gridded with 2.54-mm circles by a photoprinting technique. The load versus displacement is measured and recorded during the test, and the maximum load is essentially coincident with localized instability and the onset of fracture. A gridded specimen after failure is shown in Figure 3.47. The

[24] H. E. McGannon (ed.), *The Making, Shaping, and Treating of Steel*, 9th ed. (Pittsburgh, PA: US Steel, 1971), pp. 1126, 1260.

[25] S. P. Keeler and W. A. Backofen, *Trans. ASM, 56* (1963) 25.

[26] G. M. Goodwin, "Application of Strain Analysis to Sheet Metal Forming Problems in the Press Shop," *SAE Automotive Eng. Congr.*, Detroit, Jan. 1968, SAE Paper No. 680093.

[27] S. S. Hecker, *Metals Eng. Quart.*, 14 (1974) 30.

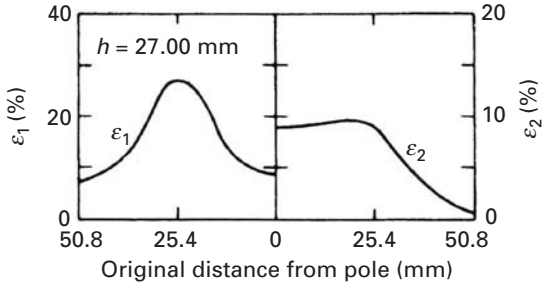


(a)

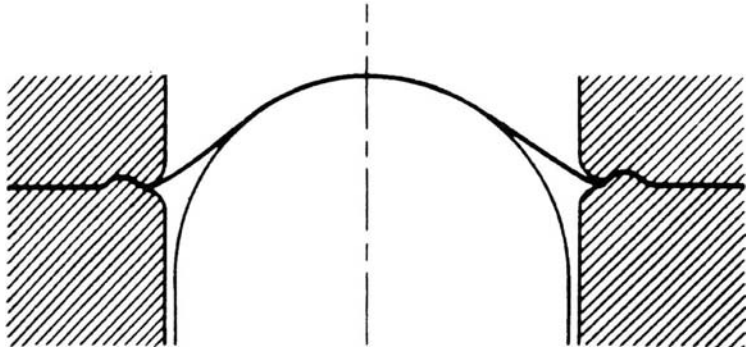

(b)

**Fig. 3.48** Schematic of sheet deformed by punch stretching. (a) Representation of strain distribution: $\varepsilon_1$, meridional strains; $\varepsilon_2$, circumferential strains; $h$, cup height. (b) Geomety of deformed sheet.

circles become distorted into ellipses. The clear circumferential mark is due to necking. The strains $\varepsilon_1$ and $\varepsilon_2$ are called meridian and circumferential strains, respectively, and are measured at various points when the test is interrupted. Figure 3.48(a) shows how these strains vary with distance from the axis of symmetry of the punch, at the point where the punch has advanced a total distance of $h = 27$ mm. $\varepsilon_1$, the meridional strain, is highest at about 25 mm from the center ($\varepsilon_1 \approx 0.25$); $\varepsilon_2$, the circumferential strain, shows a definite plateau. By using sheets with different widths and varying lubricants between the sheet and the punch, different strain patterns are obtained. (Figure 3.48(b) shows the geometry of the deformed sheet.) The tests are conducted to obtain different combinations of minor–major strains leading to failure. Figure 3.49 shows how the FLC curve is obtained. The minor strain (circumferential) is plotted on the abscissa, and the major strain (meridional) is plotted on the ordinate axis. Four different specimen geometries are shown. The V-shaped curve (FLC) marks the boundary of the safe–fail zone. The region above the line corresponds to failure; the region below is safe. In order to have both major and minor strains positive, we use a full-sized specimen. By increasing lubrication, the major strain is increased; a polyurethane spacer is used to decrease friction. The drawings on the lower left- and right-hand corners of the figure show the deformation undergone by a circle of the grid. When both strains are positive, there is a net increase in area. Consequently, the thickness of the sheet has to decrease proportionately. On

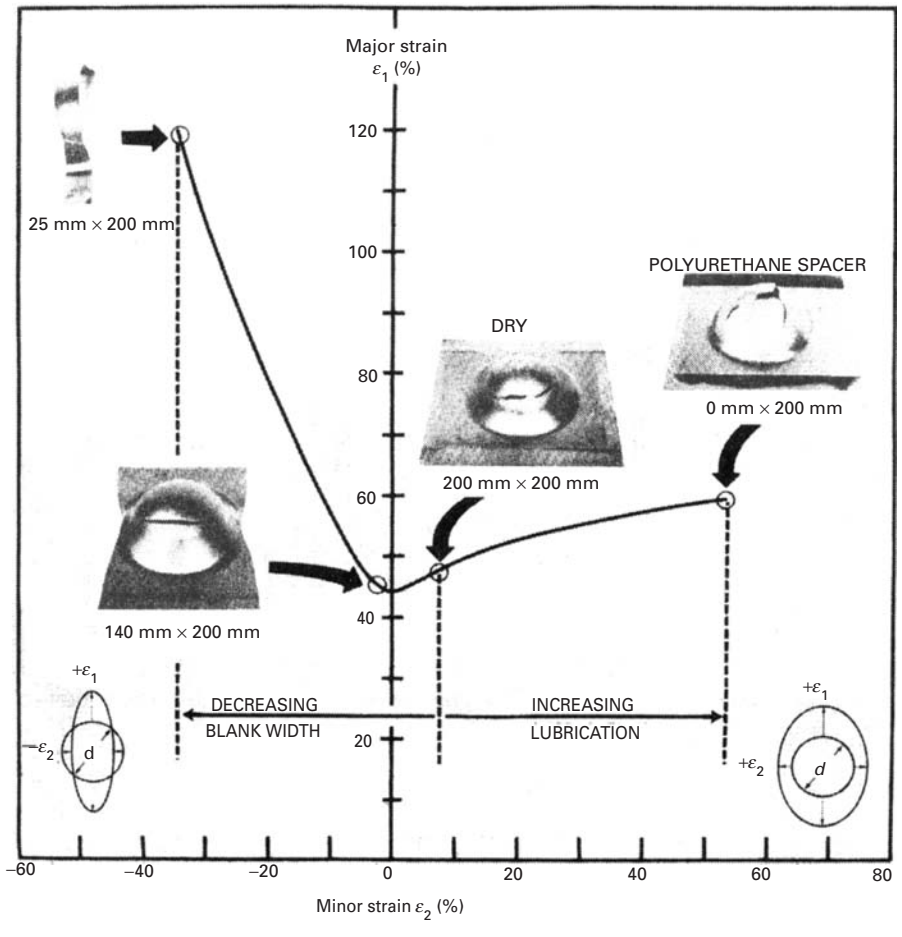


**Fig. 3.49** Construction of a forming-limit curve (or Keeler–Goodwin diagram). (Courtesy of S. S. Hecker.)

the left-hand side of the plot, negative strains are made possible by reducing the lateral dimension of the blank. This allows free contraction in this dimension. The strains in an FLC diagram are obtained by carefully measuring the dimensions of the ellipses adjacent to the neck-failure region. It is interesting to notice that diffuse necking (thinning) starts immediately after deformation, whereas localized necking occurs only after substantial forming. Semiempirical criteria for localized necking that agree well with experimental results have been developed.

FLCs provide helpful guidelines for press-shop formability. Coupled with circle-grid analysis, they can serve as a guide in modifying the shape of stampings. Circle-grid analysis consists of photoprinting a circle pattern on a blank and stamping it, determining the major and minor strains in its critical areas. The strain pattern in the stamping is then compared with the FLC to verify the available safety margin. The strain pattern can be monitored with changes in lubrication, hold-down pressure, and size and shape of drawbeads and the blank; such monitoring can lead to changes in the experimental procedure.

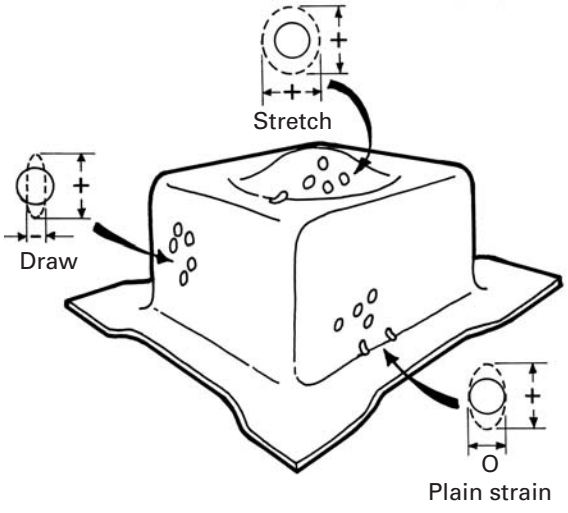


**Fig. 3.50** Different strain patterns in stamped part. (Adapted from W. Brazier, *Closed Loop*, 15, No. 1 (1986) 3.)

Circle-grid analysis also serves, in conjunction with the FLC, to indicate whether a certain alloy might be replaced by another one, possibly cheaper or lighter. During production, the use of occasional circle-grid stampings provides valuable help with respect to wear, faulty lubrication, and changes in hold-down pressure. Hecker and Ghosh[28] claim that the circle-grid analysis has replaced the craftsman's "feel" for the proper flow of the metal.

The strain pattern undergone by a stamped part is shown schematically in Figure 3.50. Different portions exhibit different strains, and this is evident by observing the distortion of circles at different regions.

## 3.10 Muscle Force

The maximum force that a muscle fiber can generate depends on the velocity at which it is activated. Figure 3.51 shows the stress that can be generated as a function of strain rate for "slow-twitch" and "fast-twitch" muscles. We use slow-twitch muscles for long-range events (e.g., distance running) and fast-twitch muscles for explosive activities, such as sprinting or throwing a punch at our professor. Both muscles show a decreasing ability to generate stress as the strain rate is increased. However, the fast-twitch muscles show a lower decay.

The plot shown in Figure 3.51 is only schematic and represents the rat *soleus* (slow-twitch) and extensor *digitorum longus* (fast-twitch). The equation that describes the response in Figure 3.51 is called the Hill[29] equation. It has the form:

$$\boxed{(\sigma + a)(\dot{\varepsilon} + b) = (\sigma_0 + a)b,}$$

[28] S. S. Hecker and A. K. Ghosh, *Sci. Am.*, Nov. (1976), p. 100.
[29] A. V. Hill, *Proc. Roy. Soc. London*, 126 (1938), 136–195.

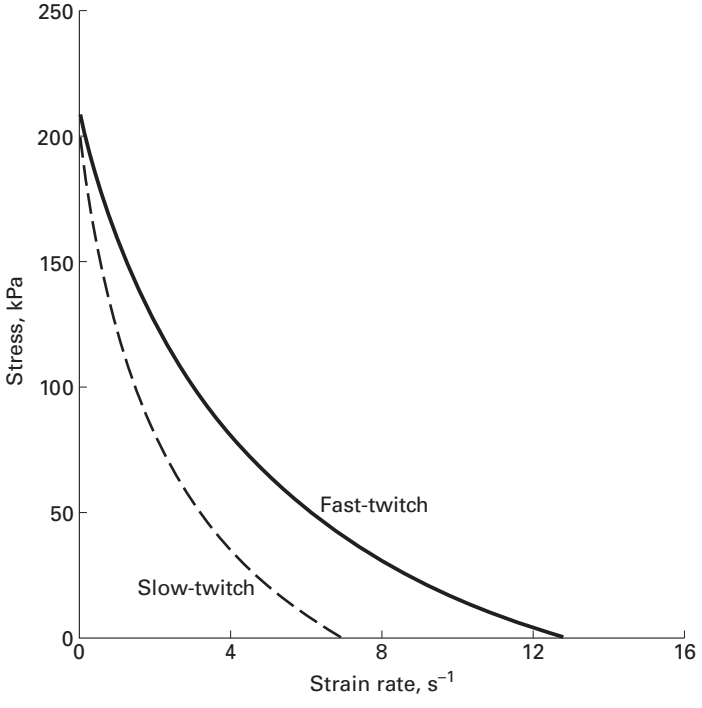


**Fig. 3.51** Stress vs. strain rate for slow-twitch and fast-twitch muscles.

where $\sigma_0$ is the stress at zero velocity (equal to 200 kPa in Figure 3.51). The range of $\sigma_0$ is usually between 100 and 300 kPa; $a$ and $b$ are parameters and $\dot{\varepsilon}$ is the strain rate (obtained from the velocity).

## Example 3.13

A person is lifting a weight by contracting the biceps muscles. Assuming that each muscle fiber has the capacity to lift 300 μg, and that each muscle fiber has a diameter of 5 μm, what is the required cross section of biceps muscle needed to lift a mass of 20 kg?

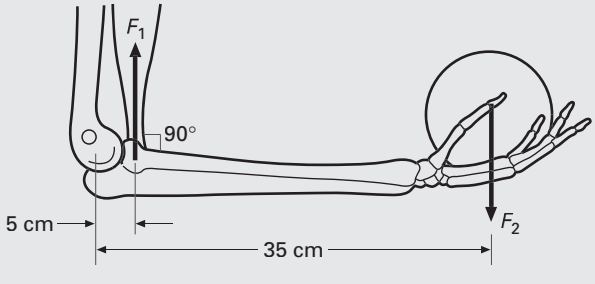


**Fig. E3.13** Forearm and force $F_2$ exerted by weight and reaction $F_1$ applied by biceps.

***Solution:*** The cross section of each fiber is:

$$A = \frac{\pi}{4} \times 5^2 = 19.625\ \mu m^2.$$

We can see from Figure E3.13 that we need to apply a lever rule to calculate the force that the muscle has to exert. Distances given in Figure E3.13 are typical. Students should check by measuring their arms. Equating the sum of the moments to zero,

$$\Sigma M_0 = 0$$
$$F_1 X_1 - F_2 X_2 = 0.$$

We have, for typical values: $X_1 = 5$ cm; $X_2 = 35$ cm.
But:

$$F_2 = 20 \times 9.8 = 196 \text{ N}.$$

Thus:

$$F_1 = \frac{196 \times 35}{5} = 1372 \text{ N}.$$

The maximum force that each muscle fiber can lift is:

$$F_f = 300 \times 10^{-6} \times 9.8 \times 10^{-3} = 2940 \times 10^{-9} \text{ N}.$$

The ratio $F_1/F_f$ gives the number of fibers:

$$N = 4.66 \times 10^8.$$

The total area is equal to:

$$A_t = N \times A = 91.425 \times 10^8\ \mu\text{m}^2.$$

This may be converted into $\text{cm}^2$:

$$A_t = 91.4\ \text{cm}^2.$$

This is indeed a biceps with a diameter of:

$$D = \left(\frac{4A_t}{\pi}\right)^{1/2} = 10.7 \text{ cm}.$$

This corresponds to Arnold on steroids!

## Example 3.14

Determine the safety factor built into the Achilles' tendon of a person weighing 80 kg, assuming a cross-sectional area of 1.5 $\text{cm}^2$, if the person can jump up to a height of 1 m, then land with a deceleration time of 0.3 s. Assume that the tensile strength of the tendon is 60 MPa. Dimensions are given in Figure E3.14.

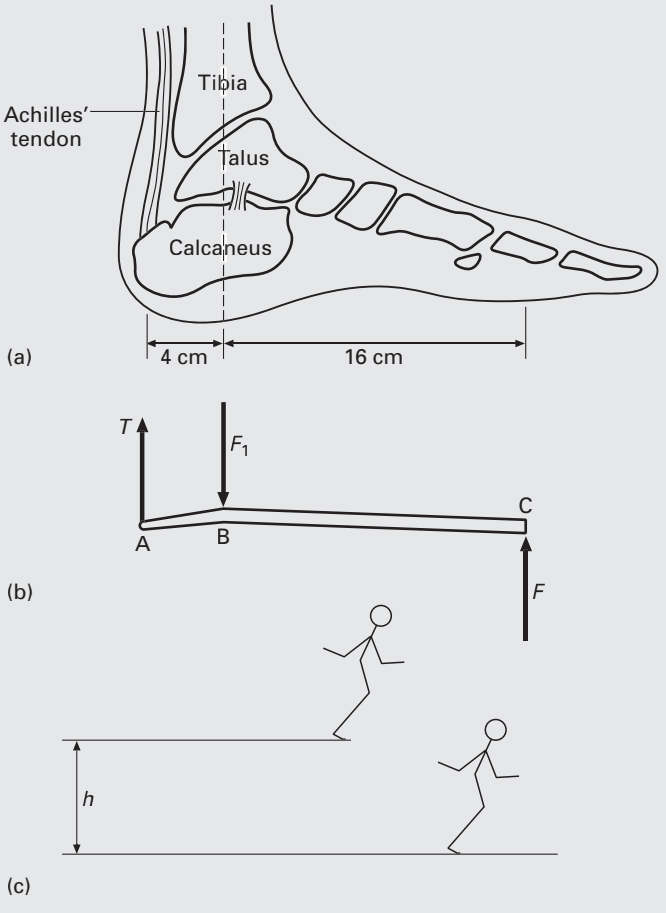


**Fig. E3.14** (a) Structure of foot with Achilles' tendon shown; (b) force *T* on tendon; (c) jump from a height *h*.

***Solution:*** We first calculate the relationship between $T$, the tension in the Achilles' tendon, and $F$, the force exerted on the ground. We assume that the person is standing on the ball of the foot.

Setting the sum of moments equal to zero,

$$\Sigma M_B = 0,$$

$$BC \times F - AB \times T = 0,$$

$$T = \frac{BC \times F}{AB}.$$

The forces and distances are defined in Figure E3.14(b). We now calculate F for the static and dynamic cases. For the static case, we simply have:

$$F_s = 80 \times 9.8 = 784 \text{ N}.$$

For the dynamic case, we have to consider the kinetic energy gained by the person, when jumping down from a height of 1 m. The potential

energy is converted into kinetic energy

$$mgh = \frac{1}{2}\, mv^2,$$

The velocity is:

$$v = (2gh)^{1/2} = 4.43 \text{ m/s}.$$

In order to find the dynamic force, $F_d$, we set the impulse equal to the change in momentum:

$$mv - m \times 0 = F_d \times t.$$

The deceleration time is given: $t = 0.3$ s.
Thus:

$$F_d = 707 \text{ N}.$$

The total force is:

$$F = F_s + F_d = 1492 \text{ N}.$$

From the figure we obtain the values of AB and BC

$$T = 5968 \text{ N}.$$

Assuming a round section, the area of the tendon is:

$$A = \frac{\pi}{4}(1.5 \times 10^{-2}) = 1.7 \times 10^{-4} \text{ m}^2.$$

Thus, the stress is:

$$\sigma = \frac{T}{A} = 35.1 \text{ MPa}.$$

The safety factor is:

$$SF = \frac{60}{35.5} = 1.7.$$

This is indeed a small number, and a weakened Achilles' tendon could easily rupture. Indeed, this happened to one of the coauthors (MAM) while playing soccer (his last game). The tendon was operated upon and reconnected through stitches. The foot was immobilized in the stretched position for 4 months enabling the tendon to repair itself. Interestingly, the operated tendon now has a cross section twice as large as the other one. Hence, nature somehow remembers the trauma and overcorrects for it. The same thing happens in bones. The healed portion becomes stronger than the original bone.

## 3.11 Mechanical Properties of Some Biological Materials

Figure 3.52 shows the stress–strain response of a number of biological materials. It may be seen that the properties vary widely. As is the case with synthetic materials, the strength increases as the

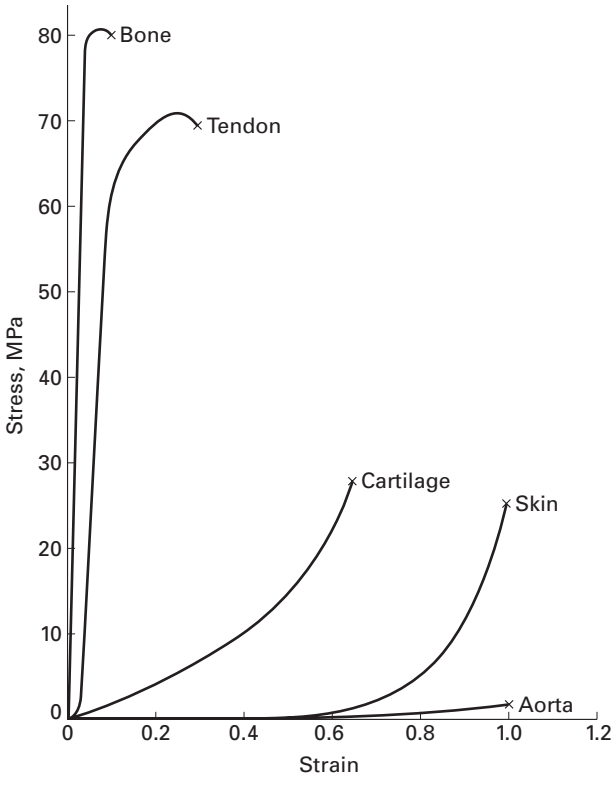


**Fig. 3.52** Stress–strain response for a number of biological materials.

ductility decreases. The strongest materials in our body are the cortical bone, followed by tendons and ligaments. The wide range in properties is due to differences in structure and constituents, presented in Chapter 1. Table 3.4 provides some important mechanical properties for a number of biological materials.

Elastin, which is described in Chapter 1, is an important component in skin and arteries. As the name implies, it provides elasticity. Figure 3.53 gives the stress–strain response from elastin taken from *ligamentum nuchae* (a long ropelike fiber running along the top of a horse's neck and holding it upright). The material is approximately linearly elastic with a Young's modulus of approximately 0.6 MPa.

Bone is the structural component of our body. It also has other functions, but we will concentrate on the mechanical performance here. There are two principal types of bone: cortical (or compact) and cancellous (or porous). Figure 3.54 shows the structure of a long bone. The surface regions consist of cortical bone; the inside is porous and is cancellous bone. The porosity reduces the strength of the bone, but also reduces its weight. Bones are shaped in such a manner that strength is provided only where it is needed. The porosity of cancellous bone provides interesting mechanical properties, which are quantitatively treated in Chapter 12. The pores also perform other physiological functions and contain the marrow. Thus, bone is a true multifunctional material. Researchers are developing synthetic

**Table 3.4** Mechanical Properties of Some Biological Materials

| Material | E (MPa) | Fracture Stress (MPa) | Strain at Fracture |
|---|---|---|---|
| Elastin | 0.6 | | |
| Resilin | 1.8 | | |
| Collagen | 1,000 | 70 | 0.09 |
| Fibroin | 10,000 | | |
| Cortical bone – | | | |
| Longitudinal | $(14–24) \times 10^3$ | 150 | ~0.015 |
| Transverse | $(8–18) \times 10^3$ | 50 | |
| Cancellous (porous) bone | 10–200 | | |
| Cellulose | 80,000 | 1000 | 0.024 |
| Tendon | 1,300 | 75 | 0.09 |
| Keratin | 2,500 | 50 | 0.02 |
| Alpha (mammalian) Beta (birds) | 2,000 | 20 | |
| Dentine | | 300 | |
| Spider Silk (radial) | | 1,500 | 0.06 |
| Silkworm Silk | | 500 | |

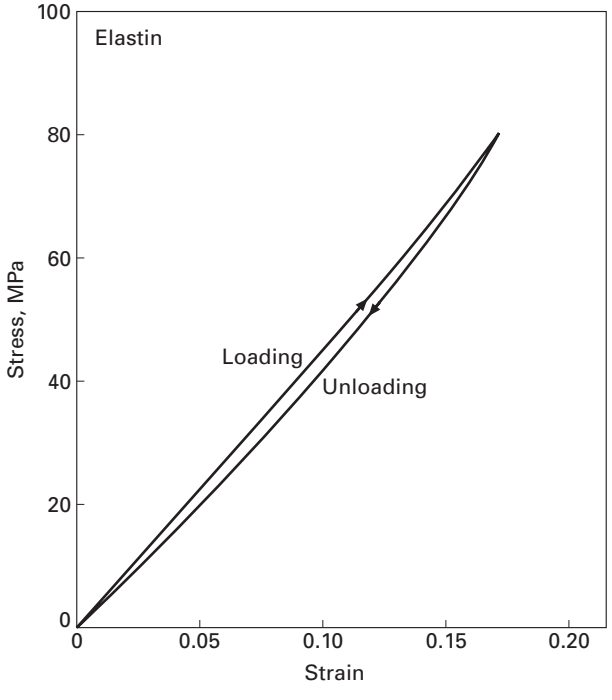


**Fig. 3.53** Stress–strain response for elastin; it is the *ligamentum nuchae* of cattle (Adapted from Y. C. Fung and S. S. Sobin, *J. Biomech. Eng.*, 1103 (1981) 121. Also in Y. C. Fung, *Biomechanics: Mechanica properties of Living Tissues* (New York: Springer, 1993) p. 244.)

multifunctional materials that have more than one function; this particular area of research is based on biological systems and is called "biomimetics" (mimicking nature).

Cortical bone is found in long bones (femur, tibia, fibula, etc.). The longitudinal mechanical properties (strength and stiffness) are higher than the transverse ones. Thus, cortical bone can be

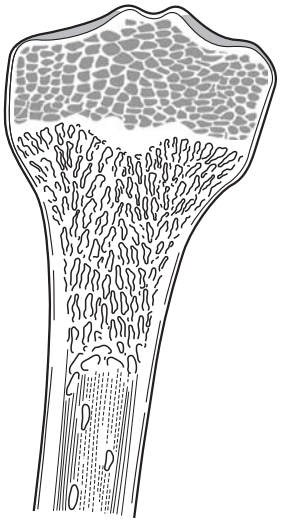

**Fig. 3.54** Longitudinal section of a femur. (From S. Mann, *Biomineralization* (New York: Oxford University Press, 2001).)

considered as transversely isotropic. Figure 3.55 provides the tensile and compressive stress–strain curves for cortical bone in longitudinal and transverse directions. The anisotropy is clearly visible. The bone is stronger in the longitudinal direction.

Bone is a composite of collagen, hydroxyapatite, and water. Hydroxyapatite is a calcium phosphate with the composition: $3Ca_3(PO_4)2Ca(OH)_2$. Water corresponds to 15–25 vol.% of the bone in mammals. The Young's modulus of cortical bone varies from 14 to 24 GPa (see Table 3.4). This is much lower than that of hydroxyapatite, which has a Young's modulus of approximately 130 GPa and a tensile strength of 100 MPa. Although collagen is not linearly elastic, we can define a tangent modulus; it is approximately 1.25 GPa. The strength achieved in bone is therefore higher than both hydroxyapatite (100 MPa) and collagen (50 MPa), demonstrating the synergistic effect of a successful composite. Hydroxyapatite is the major mineral component of bone. The hydroxyapatite content of bone varies from animal to animal, depending on function. For instance, an agile animal like a gazelle has bones that have to be highly elastic. Thus, the hydroxyapatite level is fairly low (around 50% by weight). Collagen provides the elasticity. On the other hand a whale has bones with a much higher mineral content (~80% by weight). We are somewhere in between. A young athletic student has more compliant bones than a sedentary professor!

The mechanical response of bone is also quite strain-rate sensitive. As the velocity of loading increases, both the elastic modulus and the fracture stress increase. Hence, the stiffness increases with strain rate. This is shown in Figure 3.56.

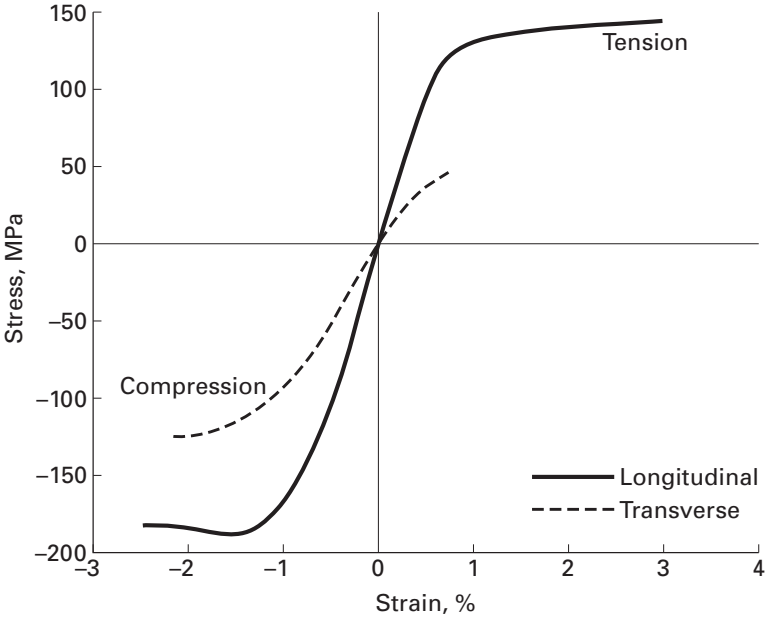


**Fig. 3.55** Tensile and compressive stress–strain curves for cortical bone in longitudinal and transverse directions. (Adapted from G. L. Lucas, F. W. Cooke, and E. A. Friis, *A Primer on Biomechanics* (New York: Springer, 1999).)

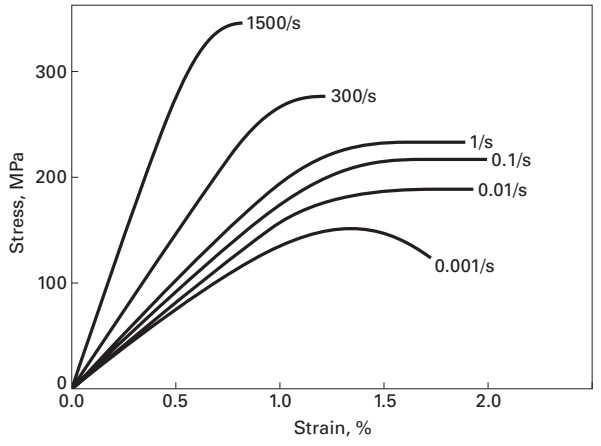


**Fig. 3.56** Strain-rate dependence of tensile response of cortical bone. (Adapted from J. H. McElhaney, *J. Appl. Physiology*, 21(1966) 1231.)

An equation called the the Ramberg–Osgood equation is used to describe this strain-rate dependence of the elastic modulus:

$$\boxed{E = \frac{\sigma}{\varepsilon} = C\,(\dot{\varepsilon})^d,}$$

where $\sigma$ is the stress, $\varepsilon$ is the strain, $\dot{\varepsilon}$ is the strain rate, and $C$ and $d$ are experimental parameters. The following are typical values:

Human cranium: $C = 15$ GPa; $d = 0.057$
Bovine cortical bone (longitidinal): $C = 12$ GPa; $d = 0.018$.

## Suggested Reading

### Plasticity

J. E. Gordon, *The New Science of Strong Materials, or Why You Don't Fall Through the Floor*. Princeton, NJ: Princeton University Press, 1976.
E. P. Popov, *Engineering Mechanics of Solids*. Englewood Cliffs, NJ: Prentice Hall, 1990.
D. Roylance, *Mechanics of Materials*. New York, NY: J. Wiley, 1996.
J. B. Wachtman, *Mechanical Properties of Ceramics*. New York, NY: J. Wiley, 1996.
R. H. Wagoner and J. L. Chenot, *Fundamentals of Metal Forming*. New York, NY: J. Wiley, 1996.

### Hardness

H. E. Boyer, ed. *Hardness Testing*. Metals Park, OH: ASM Intl., 1987. *Metals Handbook, Vol. 8: Mechanical Testing*. Metals Park, OH: ASM Int., 1985.
A. C. Fischer-Cripps, *Nanoindentation*. New York, NY: Springer, 2002.
M. C. Shaw, *Mechanical Behavior of Materials*. F. A. McClintock and A. S. Argon, eds. Reading, MA: Addison-Wesley, 1966, p. 443.
D. Tabor, *The Hardness of Metals*. London: Oxford University Press, 1951.
J. H. Westbrook and H. Conrad, eds., *The Science of Hardness Testing and Its Research Applications*. Metals Park, OH: ASM Intl., 1973.

### Formability

W. Brazier, *Closed Loop (MTS Journal)*, 15, No. 1 (1986) 3.

K. S. Chan, *J. Met.*, Feb. (1990) 6.
S. S. Hecker, in *Constitutive Equations in Viscoplasticity: Computational and Engineering Aspects*. New York, NY: ASME, 1976, p. 1.
S. S. Hecker and A. K. Ghosh, *Sci. Am.*, Nov. (1976), 100.
S. S. Hecker, A. K. Ghosh, and H. L. Gegel, eds. *Formability: Analysis, Modeling, and Experimentation*. New York, NY: TMS-AIME, 1978.
W. F. Hosford and R. M. Caddell, *Metal Forming—Mechanics and Metallurgy*. Englewood Cliffs, NJ: Prentice-Hall, 1983.

## Exercises

**3.1** A polycrystalline metal has a plastic stress–strain curve that obeys Hollomon's equation,

$$\sigma = K\,\varepsilon^n.$$

Determine $n$, knowing that the flow stresses of this material at 2% and 10% plastic deformation (offset) are equal to 175 and 185 MPa, respectively.

**3.2** You are traveling in an airplane. The engineer who designed it is, casually, on your side. He tells you that the wings were designed using the von Mises criterion. Would you feel safer if he had told you that the Tresca criterion had been used? Why?

**3.3** A material is under a state of stress such that $\sigma_1 = 3\sigma_2 = 2\sigma_3$. It starts to flow when $\sigma_2 = 140$ MPa.

**(a)** What is the flow stress in uniaxial tension?
**(b)** If the material is used under conditions in which $\sigma_1 = -\sigma_3$ and $\sigma_2 = 0$, at which value of $\sigma_3$ will it flow, according to the Tresca and von Mises criteria?

**3.4** A steel with a yield stress of 300 MPa is tested under a state of stress where $\sigma_2 = \sigma_1/2$ and $\sigma_3 = 0$. What is the stress at which yielding occurs if it is assumed that:

**(a)** The maximum-normal-stress criterion holds?
**(b)** The maximum-shear-stress criterion holds?
**(c)** The distortion-energy criterion holds?

**3.5** Determine the maximum pressure that a cylindrical gas reservoir can withstand, using the three flow criteria. Use the following information:

Material: AISI 304 stainless steel — hot finished and annealed, $\sigma_0 = 205$ MPa
Thickness: 25 mm
Diameter: 500 mm
Length: 1 mm
*Hint*: Determine the longitudinal and circumferential (hoop) stresses by the method of sections.

**3.6** Determine the value of Poisson's ratio for an isotropic cube being plastically compressed between two parallel plates.

**3.7** A low-carbon-steel cylinder, having a height of 50 mm and a diameter of 100 mm, is forged (upset) at 1,200°C and a velocity of 1 m/s, until its height is equal to 15 mm. Assuming an efficiency of 60%, and assuming that the flow

stress at the specified strain rate is 80 MPa, determine the power required to forge the specimen.

**3.8** Obtain the work-hardening exponent $n$ using Considère's criterion for the curve of Example 3.4.

**3.9** The stress–strain curve of a 70–30 brass is described by the equation

$$\sigma = 600\varepsilon_p^{0.35} \text{ MPa}$$

until the onset of plastic instability.

**(a)** Find the 0.2% offset yield stress.
**(b)** Applying Considère's criterion, find the real and engineering stress at the onset of necking.

**3.10** The onset of plastic flow in an annealed AISI 1018 steel specimen is marked by a load drop and the formation of a Lüders band. The initial strain rate is $10^{-4}$ s$^{-1}$, the length of the specimen is 5 cm, and the Lüders plateau extends itself for a strain equal to 0.1. Knowing that each Lüders band is capable of producing a strain of 0.02 after its full motion, determine:

**(a)** The number of Lüders bands that traverse the specimen.
**(b)** The velocity of each Lüders band, assuming that only one band exists at each time.

**3.11** A tensile test on a steel specimen having a cross-sectional area of 2 cm$^2$ and length of 10 cm is conducted in an Instron universal testing machine with stiffness of 20 MN/m. If the initial strain rate is $10^{-3}$ s$^{-1}$, determine the slope of the load-extension curve in the elastic range ($E = 210$ GN/m$^2$).

**3.12** Determine all the parameters that can be obtained from a stress–strain curve from the load-extension curve (for a cylindrical specimen) shown in Figure E.3.12, knowing that the initial cross-sectional area is 4 cm$^2$, the crosshead velocity is 3 mm/s, the gage length is 10 cm, the final cross-sectional area is 2 cm$^2$, and the radius of curvature of the neck is 1 cm.

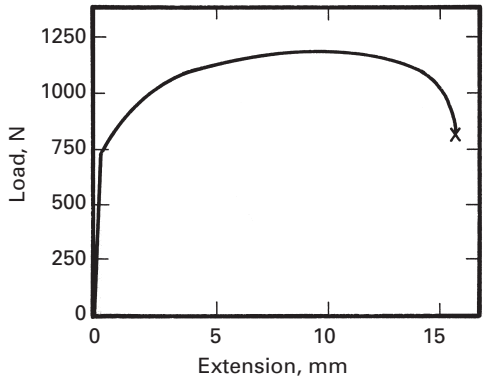


**Fig. Ex.3.12**

**3.13** Draw the engineering-stress–engineering-strain and true-stress–true-strain (with and without Bridgman correction) curves from the curve in Exercise 3.12.

**3.14** What is the strain-rate sensitivity of AISI 1040 steel at a strain of 0.02 and a strain of 0.05 (Obtain your data from Figure 3.12(a).)

**3.15** From the load-extension curve shown in Example 3.4, draw the true-stress–true-strain curve.

**3.16** An AISI 1045 steel obeys the following relationship relationship between stress ($\sigma$) and strain ($e$) in tension:

$$\sigma(\text{MPa}) = 300 + 450e^{0.5}.$$

Obtain the compressive stress–strain curve, considering the Bauschinger effect. Use the data from Figure 3.17.

**3.17** The PMMA specimens, Figure Ex.3.17, were deformed in uniaxial tension at different temperatures. (a) Plot the total elongation, ultimate tensile stress, and Young's modulus as a function of temperature. (b) Discuss changes in these properties in terms of the internal structure of the specimen.

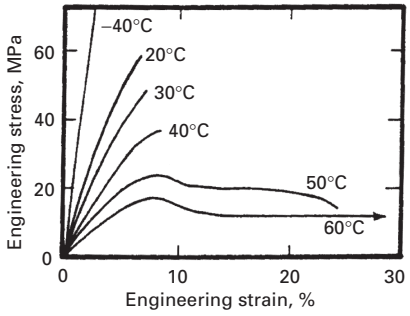


**Fig. Ex.3.17**

**3.18** For the force–displacement curve of Figure Ex.3.18, obtain the engineering and true-stress–strain curves if the specimen were tested in compression.

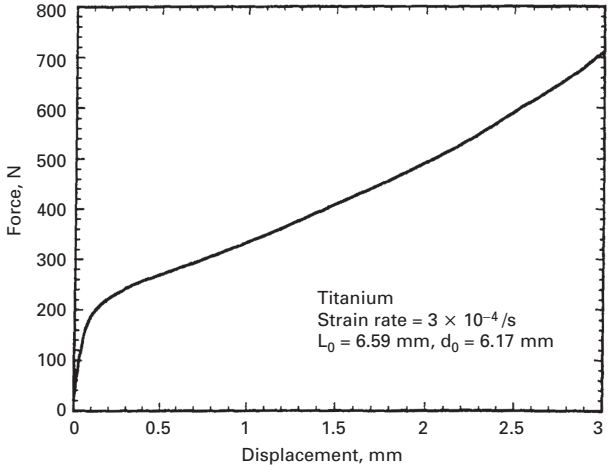


**Fig. Ex.3.18**

**3.19** Calculate the softening temperature for a soda–lime silica glass at which the viscosity is equal to $10^7$ Pa · s if the activation energy for viscous flow is 250 kJ/mol and the viscosity at 1,000°C is $10^3$ Pa · s.

**3.20** The viscosity of a $SiO_2$ glass is $10^{14}$ P at 1,000 °C and $10^{11}$ P at 1,300 °C. What is the activation energy for viscous flow in this glass? Note: 1 P = 0.1 Pa · s.

**3.21** When tested at room temperature, a thermoplastic material showed a yield strength of 51 MPa in uniaxial tension and 55 MPa in uniaxial compression. Compute the yield strength of this polymer when tested in a pressure chamber with a superimposed hydrostatic pressure of 300 MPa.

**3.22** From Equation 3.35, obtain Equation 3.34. Then prove that Equation 3.34 represents an ellipse rotated 45° from its principal axis.

**3.23** An annealed sheet of AISI 1040 steel (0.85 mm thick and with in-plane isotropy) was tested in uniaxial tension until the onset of necking, to determine its formability. The initial specimen's length and width were 20 and 2 cm, respectively. At the onset of necking, the length and width were 25 and 1.7 cm, respectively.

**(a)** Determine the ratio between the through-thickness and the in-plane yield stress, assuming that $R$ does not vary with strain.
**(b)** Draw the flow locus of this sheet, assuming that $\sigma_{y(1,2)} = 180$ MN/m$^2$.

**3.24** Repeat Exercise 3.23 if the final width of the specimen is 1.9 cm, and explain the differences. Which case has a better formability?

**3.25** Imagine that you want to perform a circle-grid analysis, but you do not have the facilities for photoprinting. Hence, you decide to make a grid of perpendicular and equidistant lines. After plastic deformation of the material, can you still determine the major and minor strains from the distorted grid? (*Hint*: Use the method for determining principal strains.)

**3.26** Determine the activation energy for deformation for the three glasses shown in Figure 3.26. (Hint: plot ln viscosity vs. 1/$T$.)

**3.27** You are given a 2.5 mm diameter cylindrical specimen 180 mm long. If the specimen is subjected to a torque of 50 N · m.

**(a)** Calculate the deflection of the specimen end, if one end is fixed.
**(b)** Will the specimen undergo plastic deformation?

**3.28** Calculate the resulting rod diameter for 1040 carbon steel subjected to a 4000 N compressive load, with an initial diameter of 15 cm.

**3.29** You are asked to design a spherical pressure vessel for space application. The weight has to be minimized. Given that $\sigma = Pr/T$, among materials below, which one you would select?

| Alloy | Density (kg/m$^3$) | Y. S. (MPa) |
|---|---|---|
| 304 SS | $7.8\times10^3$ | 400 |
| Ti6Al4V | $4.46\times10^3$ | 850 |
| 2024 Al | $2.7\times10^3$ | 400 |

**3.30** You have a piece of steel, and you are able to measure its hardness: HV = 250 kg/mm$^2$. What is its estimated yield stress, in MPa?

**3.31** You received a piece of cast iron, and you want to estimate its yield strength. You are able to make a hardness indentation using a 10 mm diameter tungsten carbide sphere. The diameter of the indentation is 4 mm. What is the estimated yield strength?

**3.32** Describe the similarities and differences in the phenomena of Lüders band formation in low-carbon steels and tensile drawing of a polymer.

**3.33** The shear yield strength of a polymer is 30% higher in compression than in tension. Determine the coefficient $A$ that represents the dependence of yield stress on hydrostatic pressure.

**3.34** Looking at Figure 3.3, give reasons as to why the ultimate tensile stress (UTS) of AISI 1040 steel decreses with increased heat treatment.

**3.35**

**(a)** Describe the changes that occur at a microstructural level when a thin semicrystalline polymer begins to neck.

**(b)** Why does the strength increase in the load direction? Does the necking region become more or less transparent if the material is made of a semi-transparent material?

**3.36** The following stresses were measured on a metal specimen:

$\sigma_{11}$ = 94 MPa
$\sigma_{22}$ = 155 MPa
$\sigma_{12}$ = 85 MPa.

Determine the yielding for both the Tresca and von Mises criteria, given that $\sigma_0$ = 180 MPa (yield stress). Which criterion is more conservative?

**3.37** A flat indenter strikes the surface of an iron block and sinks into the material by 0.4 cm. Assuming that the surface of a piece of iron ($\tau_0$ = 6.6 GPa, $\sigma_0$ = 12.6 GPa, $A$ = 0.5 cm$^2$) can be modeled as triangular blocks as in Figure E2.10.2, determine the force with which the indenter hits the material.

**3.38** Determine the hardness of the copper specimen from the nanoindentation SEM image in Figure 3.42(b) knowing that the applied load is 2000 μN.

**3.39** Calculate the projected area of an indentation made in keratin, the penetration depth $h$ is 600 nm. Assume we used the Berkovich tip ($A = 24.5h^2$).

**3.40** You are designing a kinetic energy penetrator for the M1 tank. This penetrator is made of depleted (non-radioactive but highly lethal!) uranium-0.75%Ti. Plot the stress–strain curve, from 0 to 1:

**(a)** At the following strain rates: $10^{-3}$ s$^{-1}$, $10^{3}$ s$^{-1}$ (ambient temperature).

**(b)** At a strain rate of $10^{-3}$ s$^{-1}$ and the following temperatures: 77 K, 100 K, 300 K.

Given:
$T_m$ = 1473 K
$\sigma_0$ = 1079 MPa
$K$ = 1120 MPa
$n$ = 0.25
$C$ = 0.007
$m$ = 1
$\dot{\varepsilon}$ = $10^{-4}$ s$^{-1}$

Chapter 4

# Imperfections: Point and Line Defects

## 4.1 Introduction

The mechanical properties of materials are often limited by their imperfections. The theoretical cleavage and shear strengths of materials are given by (see Section 4.2):

$$\sigma_{\text{th}} = \sqrt{\frac{E\gamma}{a}} \approx \frac{E}{\pi} \quad \text{and} \quad \tau_{\text{th}} = \frac{Gb}{2\pi a} \approx \frac{G}{2\pi},$$

where $E$ and $G$ are the Young's and shear moduli, respectively; $a$ is the interatomic spacing, and $\gamma$ is the surface energy of the material. These equations predict exceedingly high strengths (on the order of GPas), and few materials reach such strengths. (See Chapter 1.) Indeed, this is somehow the Holy Grail of materials science: If materials were perfect, those values could be reached. However, all materials contain imperfections, either by design or inadvertently produced during processing. We review these in this and subsequent chapters. They are classified, according to their dimensions, into four kinds, each discussed in a separate section as follows:

- Point (atomic or electronic) defects (Section 4.3)
- Line (or one-dimensional) defects (Section 4.3)
- Interfacial (or two-dimensional) defects (Chapter 5, Section 5.1)
- Volume (or three-dimensional) defects (Chapter 5, Section 5.2).

Cracks are discussed in chapters 7 and 8, on fracture.

Imperfections determine the mechanical response of materials, and the manner in which the response is used to enhance performance in a material will be analyzed in considerable detail in chapters 5 through 9. Note that the dimensional scale of defects covers a wide spectrum, $10^{-14}$ m, as shown schematically in Figure 4.1. Electronic point defects do not affect mechanical properties significantly and will therefore not be discussed in this text.

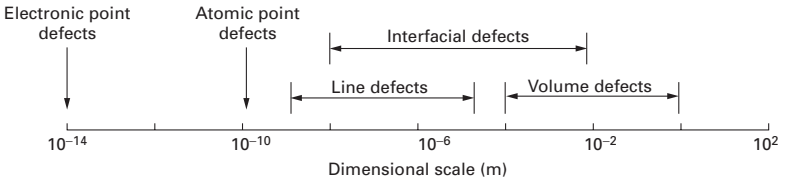


**Fig. 4.1** Dimensional ranges of different classes of defects.

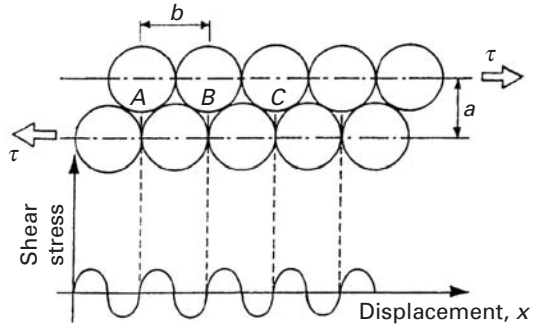


**Fig. 4.2** Stress required to shear a crystal.

## 4.2 Theoretical Shear Strength

Frenkel[1] performed a simple calculation of the theoretical shear strength of crystals by considering two adjacent and parallel lines of atoms subjected to a shear stress; this configuration is shown in Figure 4.2 where $a$ is the separation between the adjacent planes and $b$ is the interatomic distance. Under the action of the stress $\tau$, the top line will move in relation to the bottom line; the atoms will pass through successive equilibrium positions $A$, $B$, $C$, for which $\tau$ is zero. When the applied shear stress is enough to overcome these barriers, plastic deformation will occur, and the atoms will move until a shear fracture is produced. The stress is also zero when the atoms are exactly superimposed; in that case, the equilibrium is metastable. Between these values the stress varies cyclically with a period $b$. Frenkel assumed a sine function, as one would expect:

$$\tau = k \sin \frac{2\pi x}{b}, \tag{4.1}$$

where $x$ is the displacement, $b$ is the Burgers vector, and $k$ is the constant to be determined (see below).

For small displacements,

$$\tau = k \frac{2\pi x}{b}. \tag{4.2}$$

Since, for small displacements, one can consider the material to deform elastically, we have

$$\tau = G \frac{x}{a}, \tag{4.3}$$

where $x/a$ is the shear strain and $G$ is the shear modulus. Substituting Equation 4.3 into Equation 4.2, we have

$$k = \frac{G b}{2\pi a}. \tag{4.4}$$

[1] J. Frenkel, *Z. Phys.*, 37 (1926) 572.

**Table 4.1** Theoretical Shear Strength[a]

| Element | $G$ (GPa) | $\tau_{max}$ (GPa) | $\tau_{max}/G$ |
|---|---|---|---|
| Iron | 60.0 | 6.6 | 0.11 |
| Silver | 19.7 | 0.77 | 0.039 |
| Gold | 19.0 | 0.74 | 0.039 |
| Copper | 30.8 | 1.2 | 0.039 |
| Tungsten | 150.0 | 16.5 | 0.11 |
| Diamond | 505.0 | 121.0 | 0.24 |
| NaCl | 23.7 | 2.8 | 0.12 |

[a] From A. Kelly, *Strong Solids* (Oxford, U.K.: Clarendon Press, 1973), p. 28.

Substituting Equation 4.4 into Equation 4.1 yields

$$\tau = \frac{G\,b}{2\pi\,a} \sin \frac{2\pi\,x}{b}.$$

The maximum of $\tau$ occurs for $x = b/4$:

$$\boxed{\tau_{\max} = \frac{G\,b}{2\pi\,a}.} \tag{4.5}$$

For FCC materials, the relationship between $a_0$ (the lattice parameter), $a$, and $b$ can be calculated. Drawing a unit cell, the student will be able to show that $b = a_0/2$; the spacing between adjacent planes is given by (see crystallography textbooks):

$$d_{hkl} = \frac{a_0}{\sqrt{h^2 + k^2 + \ell^2}}.$$

For (111) planes:

$$d_{111} = a_0/\sqrt{3}.$$

This is equal to $a$ in Figure 4.2.

Substituting $b$ and $a$ into Equation 4.5, we obtain

$$\tau_{\max} \approx \frac{G}{5.1}. \tag{4.6}$$

More complex models have been advanced in which the sine function is replaced by more precise curves expressing the interaction energy. The method used by Kelly (Mackenzie's method) is an example. Kelly took into account the distortion of the planes. Table 4.1 shows the stresses calculated by Mackenzie's method. Note that the ratio $\tau_{max}/G$ varies between 0.039 and 0.24. Consequently, it is fairly close to Frenkel's ratio (0.18), obtained by the simpler method.

The theoretical strength derived above is on the order of gigapascals; unfortunately, the actual strength of materials is orders of magnitude below that. We derive an expression for theoretical cleavage strength in Chapter 7.

### Example 4.1

Estimate the theoretical shear and cleavage strength for copper and iron. From Table 2.5 in Chapter 2, we have the following data:

| | | |
|---|---|---|
| Iron | $E = 211.4$ GPa | $G = 81.6$ GPa |
| Copper | $E = 129.8$ GPa | $G = 43.3$ GPa |

For the shear strength, we assume, to a first approximation, that $b = a$. Thus,

$$\boxed{\tau_{\max} = \frac{G}{2\pi}}$$

and

Fe: $\tau_{\max} = 13.0$ GPa

Cu: $\tau_{\max} = 7.7$ GPa.

For the cleavage strength,

$$\sigma_{\max} = \sqrt{\frac{E\gamma}{a_0}} \quad \text{and} \quad \gamma \approx \frac{E a_0}{10};$$

So

$$\sigma_{\max} \approx \sqrt{\frac{E^2}{10}} \approx \boxed{\frac{E}{3.16}}.$$

Therefore, we have

Fe: $\sigma_{\max} = 66.9$ GPa

Cu: $\sigma_{\max} = 41.1$ GPa.

The actual tensile strength of pure Fe and Cu is on the order of 0.1 GPa. Since these metals fail by shear, the actual shear strength is equal to 0.05 GPa.

## 4.3 Atomic or Electronic Point Defects

These defects exist on an atomic scale. These defects can have a diameter of approximately $10^{-10}$ m. Although relatively small compared to other imperfections, atomic defects do generate a stress field in the crystal lattice and affect the properties of the material. Figure 4.3 shows the following three types of atomic point defects.

1. *Vacancy*. When an atomic position in the Bravais lattice is vacant.
2. *Interstitial point defect*. When an atom occupies an interstitial position. This interstitial position can be occupied by an atom of the material itself or by a foreign atom; the defect is called a self-interstitial and an interstitial impurity, respectively, for the two cases.

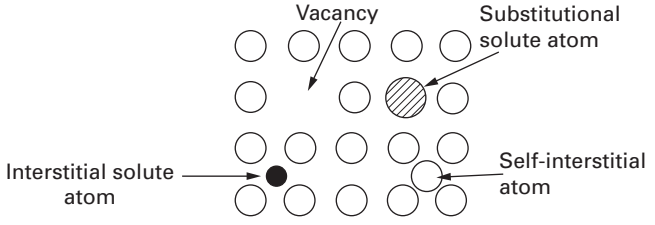


**Fig. 4.3** Atomic point defects.

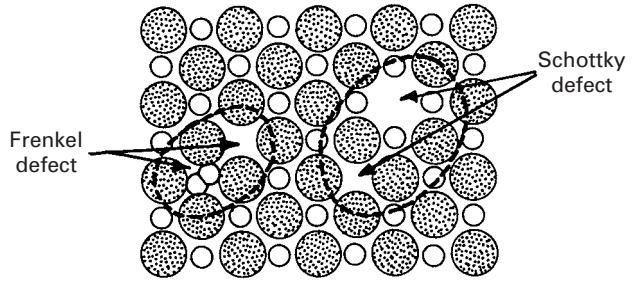


**Fig. 4.4** Two most common point defects in compounds: Schottky and Frenkel defects.

3. *Substitutional point defect*. When a regular atomic position is occupied by a foreign atom.

The vacancy concentration in pure elements is very low at low temperatures. The probability that an atomic site is a vacancy is approximately $10^{-6}$ at low temperatures, rising to $10^{-3}$ at the melting point. In spite of their low concentration, vacancies have a very important effect on the properties of a material, because they control the self-diffusion and substitutional diffusion rates. The movement of atoms in the structure is coupled to the movement of vacancies. In Section 4.3.1, the equilibrium concentration of vacancies is calculated.

In compounds (ceramics and intermetallics), defects cannot occur as freely as in metals, because we have additional requirements, such as electrical neutrality. Two types of defects are prominent in compounds and are shown in Figure 4.4: the Schottky defect, which is a pair of vacancies that have opposite sign (one cation and one anion); and the Frenkel defect, which consists of a vacancy–self-interstitial pair.

The self-interstitial and interstitial impurities lodge themselves in the "holes" that the structure has. There is more than one type of hole in the FCC, BCC, and HCP structures, and their diameters and positions will be determined in what follows.

The FCC structure, shown in Figure 4.5 has two types of voids: the larger, called octahedral, and the smaller, called tetrahedral. The names are derived from the nearest neighbor atoms; they form the vertices of the polyhedra shown. If we consider the atoms as rigid spheres, we can calculate the maximum radius of a sphere that would fit into the void without straining the lattice. The reader is encouraged to engage in this exercise; with some luck, he or she will find radii of 55 and 31 pm for octahedral and tetrahedral voids, respectively, in $\gamma$-iron. Hence, carbon ($r = 80$ pm) and nitrogen ($r = 70$ pm) produce distortions in the lattice when they occupy the voids.

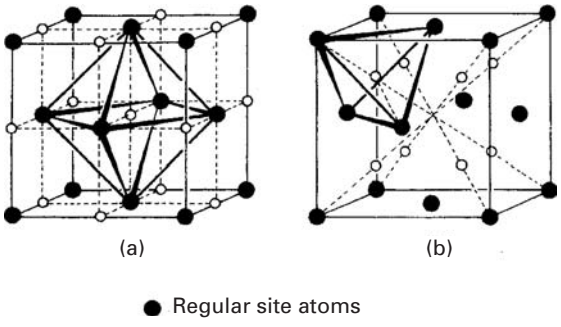


**Fig. 4.5** Interstices in FCC structure. (a) Octahedral void. (b) Tetrahedral void.

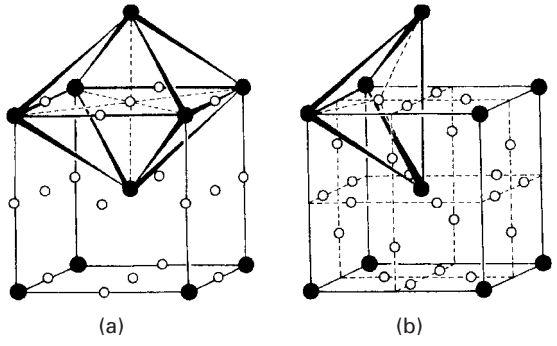


**Fig. 4.6** Interstices in the BCC structure. (a) Octahedral void. (b) Tetrahedral void.

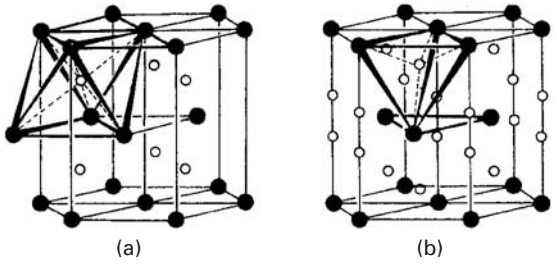


**Fig. 4.7** Interstices in the HCP structure. (a) Octahedral void. (b) Tetrahedral void.

In BCC metals there are also octahedral and tetrahedral voids, as shown in Figure 4.6. In this case, however, the larger void is tetrahedral. For rigid spheres in $\alpha$-iron, the void radii are 36 and 19 pm for tetrahedral and octahedral interstices, respectively. Hence, a solute atom is accommodated in an easier way in FCC than in BCC iron, in spite of the fact that the FCC structure is more closely packed.

Analogously, the HCP structure presents tetrahedral and octahedral voids, shown in Figure 4.7; the reader is reminded of the similarity between the FCC and HCP structures, which explains the presence of the same voids.

### 4.3.1 Equilibrium Concentration of Point Defects

A very important characteristic of vacancies and self-interstitial atoms, in contrast to line and surface defects, is that they can exist in thermodynamic equilibrium at temperatures above 0 K. The thermodynamic equilibrium in a system of constant mass, at a constant pressure and temperature, and that does not execute any work in addition

to the work against pressure, is reached when the Gibbs free energy is minimum. The formation of point defects in a metal requires a certain quantity of heat $\delta q$ (as there is no work being executed, except against pressure). Hence, if $dH = \delta q$, the enthalpy $H$ of the system increases. The configurational entropy $S$ also increases, because there are a certain number of different ways of putting the defects into the system.

The Gibbs free energy is, by definition,

$$G = H - TS. \tag{4.7}$$

One can thus see that the free energy will reach a minimum for a certain value of $n$ (the number of point defects) different from zero; at 0 K, the entropic term is zero and the equilibrium concentration is zero.

The equilibrium concentration of point defects can be calculated from statistical considerations and is given by

$$\boxed{\frac{n}{N} = \exp(-G_f/kT)} \tag{4.8}$$

where $n$ and $N$ are the number of point defects and sites, respectively, $G_f$ is the free energy of formation of the defects, and $k$ is Boltzmann's constant. For copper, the formation of vacancies and interstitials are

$$G_v = 83 \text{ kJ/mol}, \quad G_i = 580 \text{ kJ/mol}.$$

We have, approximately, the following ratio:

$$\frac{G_i}{G_v} \approx 7.$$

Therefore, for copper, the free energy of formation of a vacancy is approximately one-seventh that of a self-interstitial defect. Using Equation 4.8, we can obtain the ratio between the vacancy ($X_v$) and interstitial ($X_i$) concentrations:

$$\frac{X_v}{X_i} \approx \exp\left(\frac{G_i - G_v}{kT}\right). \tag{4.9}$$

For copper at 1,000 K (we have to convert molar quantities or use $R = 8.314$ J/(mol K):

$$\frac{X_v}{X_i} \approx 10^{26}.$$

It can be concluded that, at least in close-packed structures, the concentration of interstitials is negligible with respect to that of the vacancies. Using Equation 4.9 for copper at 1,000 K, we obtain

$$X_v \cong 4.5 \times 10^{-5}.$$

Hence, there is only one vacancy for each $2 \times 10^4$ copper atoms at 1,000 K. This number is very small; in spite of this, it corresponds to approximately $10^{14}$ vacancies/cm$^3$. The low concentration of self-interstitials in close-packed structures is a consequence of the

small diameter of the interstitial voids. (See Figures 4.5 and 4.6.) In more open structures these concentrations can be higher. Even so, high interstitial concentrations are not observed in equilibrium structures.

## Example 4.2

If, at 400 °C, the concentration of vacancies in aluminum is $2.3 \times 10^{-5}$, what is the excess concentration of vacancies if the aluminum is quenched from 600 °C to room temperature? What is the number of vacancies in one cubic $\mu$m of quenched aluminum?

We are given:

$$G_v = 0.62\,\text{eV},$$
$$k = 86.2 \times 10^{-6}\,\text{eV/K},$$
$$r_{\text{Al}} = 0.143\,\text{nm}.$$

***Solution***: We have

$$\frac{n_v}{N} = e^{-Gv/kT}.$$

At 400 °C (= 673 K),

$$2.3 \times 10^{-5} = e^{-0.62/86.2\times10^{-6}\times673},$$

Thus,

$$\frac{n_v}{n} = e^{-0.62/86.2\times10^{-6}\times873} = 2.6 \times 10^{-4}.$$

Aluminum has the FCC structure, with four atoms per unit cell. The lattice parameter $a$ is related to the unit cell by

$$a = 2\sqrt{2r} = 0.404\ \text{nm}.$$

The corresponding volume is

$$V = a^3 = 0.0662\ \text{nm}^3.$$

In one $\mu$m$^3$, the number of atoms is

$$n = \frac{4 \times 10^9}{0.0662} = 6.04 \times 10^{10},$$
$$n_v = (2.6 \times 10^{-4})n = 1.6 \times 10^7.$$

Hence, there are about $1.6 \times 10^7$ vacancies per cubic $\mu$m of the quenched aluminum.

Point defects can group themselves in more complex arrangements (for instance, two vacancies form a divacancy, two interstitials form a diinterstitial, etc.) The energy of formation of divacancies has been determined for several metals. For example, for copper (with $G_f = 5.63 \times 10^{-19}$ J), it is: $0.96 \times 10^{-19}$ J. The energy of formation of divacancies in noble metals in on the order of $0.48 \times 10^{-19}$ J. It is thought that divacancies are stable, in spite of the fact that their enthalpies of bonding are not very well known.

Diinterstitials also exist, and their energies can be calculated by the same processes as for monointerstitials. Similarly, the vacancies can bind themselves to atoms of impurities when the binding energy is positive.

### 4.3.2 Production of Point Defects

Intrinsic point defects in a metal – either vacancies or self-interstitials – exist in well-established equilibrium concentrations. (See Section 4.3.1.) By appropriate processing, the concentration of these defects can be increased. Quenching, or ultra-high-speed cooling, is one of these methods. The concentration of vacancies in BCC, FCC, and HCP metals is greatly superior to that of interstitials and on the order of $10^{-3}$ when the metal is at a temperature close to the melting point; it is only $10^{-6}$ when the metal is at a temperature of about half the melting point. Hence, if a specimen is cooled at a high enough rate, the high-temperature concentration can be retained at low temperatures. For this to occur, the rate of cooling has to be such that the vacancies cannot diffuse to sinks – grain boundaries, dislocations, surface, and so on. Theoretically, gold would have to be cooled from 1,330 K to ambient temperature at a rate of $10^{11}$ K/s to retain its high-temperature vacancy concentration. The fastest quenching technique to cool thin wires produces cooling rates lower than $10^5$ K/s; nevertheless, a significant portion of the high-temperature point defects is retained.

Another method of increasing the concentration of point defects is by plastic deformation. The movement of dislocations generates point defects by two mechanisms: the nonconservative motion of jogs, and the annihilation of parallel dislocations of opposite sign, producing a line of vacancies or interstitials. *Jogs* are created by dislocation intersections; since they cannot glide with dislocations, they have to climb as the dislocation moves. In a screw dislocation, they are small segments having the character of an edge. The slip plane of this segment is not compatible with that of the dislocation. The climb is possible only by continuous emission of vacancies or interstitials. The second mechanism is depicted schematically in Figure 4.8. When the two dislocations cancel each other, they create a row of interstitials or vacancies if their slip planes do not coincide.

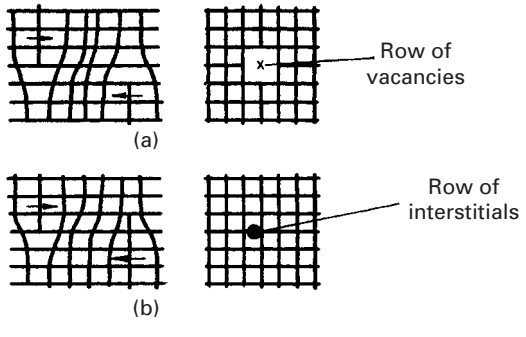


**Fig. 4.8** Formation of point defects by the annihilation of dislocations. (a) Row of vacancies. (b) Row of interstitials.

Quenching produces mostly vacancies and vacancy groups. The concentrations obtained are lower than $10^{-4}$. Deformation, on the other hand, can introduce higher concentrations of vacancies and equivalent ones of interstitials; the problem is that it also introduces a number of other substructural changes that complicate the situation. Dislocations are introduced, and they interact strongly with point defects. One method of producing point defects does not present these problems: *Irradiation* of the metal by high-energy particles allows the introduction of a high concentration of point defects. The radiation displaces the electrons, or ionizes, displaces atoms by elastic collisions, and produces fission and thermal spikes. This subject is treated in greater detail in Section 4.3.4. The displacement of atoms is produced by the elastic collision of the bombarding particles with the lattice atoms, transferring the kinetic energy of the particles to the atoms. This may cause the atoms to travel through the lattice. In the majority of cases, an atom travels a few atomic distances and enters an interstitial site. Consequently, a vacancy is produced, together with a self-interstitial. The energy transferred in the collision has to be well above the energy required to form an interstitial--vacancy pair in a reversible thermodynamic process (3 to 6 eV, or $4.8 \times 10^{-19}$ to $9.6 \times 10^{-19}$ J). It is believed that the energy transferred to the atom has to be approximately 25 eV ($40 \times 10^{-19}$ J). Different particles can be used in the bombardment process: neutrons, electrons, $\gamma$ rays, and $\alpha$ particles.

### 4.3.3 Effect of Point Defects on Mechanical Properties

Point defects have a marked effect on the mechanical properties of a material. For this reason, the effect of radiation is of great importance. Maddin and Cottrell[2] used aluminum single crystals with various purity levels, observing that the yield stress increased with quenching. Quenching was accomplished by taking the specimens from 600 °C and throwing them into a water–ice mixture, while annealed material was slowly cooled in the furnace. The yield stress increased from 550 to 5,900 kPa, on average. The effect of impurity atoms could be neglected because the increase in yield stress was consistent throughout the specimens. The effect of possible residual stresses due to quenching was also neglected. With the purpose of obtaining evidence that was still more convincing, a single crystal was tested immediately after quenching, while another was tested after staying a few days at ambient temperature. The yield stress increased from 5.9 MPa to 8.4 MPa in the aged condition. The strengthening by quenching is due to the interaction of dislocations and vacancies or groups thereof. The effect of jogs, formed by the condensation of vacancies on the dislocations, can also be considerable. During aging, the excess concentration of vacancies forms groups and/or annihilates preexisting dislocations.

[2] R. Maddin and A. H. Cottrell, *Phil. Mag.*, 46 (1955) 735.

There are also alterations in the plastic portion of the stress-versus-strain curve seen in Figure 4.9. The initial work-hardening rate of the quenched aluminum is lower than that of slowly (furnace) cooled aluminum. At greater strains, however, the two work-hardening rates become fairly similar. Hence, the effect of quenching disappears at higher strains. This is thought to be because the excess concentrations of point defects are eliminated during plastic deformation; at the same time, excess vacancies are generated by dislocation motion, so that the concentrations in the quenched and furnace cooled materials become the same.

The increase in hardness in many quenched metals is negligible, in spite of the obvious changes in the stress-versus-strain curve. This is explained by the fact that the effect of quenching disappears after a certain amount of plastic deformation. Since the indenter deforms the metal plastically (in an extensive way), the effect of quenching is minimal.

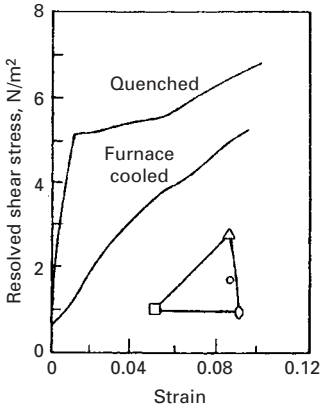


**Fig. 4.9** Stress-versus-strain curves for aluminum single crystals. The crystallographic orientation is shown in the stereographic triangle. (Adapted with permission from A. H. Cottrell, *Phil. Mag.*, 46 (1955) p. 737.)

### 4.3.4 Radiation Damage

Irradiation of solids by high-energy particles may produce one or more of the following effects:

1. Displaced electrons (i.e., ionization).
2. Displaced atoms by elastic collision.
3. Fission and thermal spikes.

Ionization has a much more important role in nonmetals than it has in metals. The high electrical conductivity of metals leads to a very quick neutralization of ionization, and there is no observable change in properties due to this phenomenon. Electronic excitations in metals are also eliminated almost instantaneously. Such would not be the case in semiconductors and dielectrics, where electronic excitation configurations are almost permanent. Thus, in the case of metals, only collisions among incident particles and atomic nuclei are of importance. The basic mechanism in all processes of radiation damage is the transfer of energy and motion from the incident particle beams to the atoms of the material. The incident particle beam may consist of positive particles (protons, for example), negative particles (which are invariably electrons), or neutral particles (X-rays, $\gamma$-rays, neutrons, etc.). Irradiation by neutrons results in a large spectrum of constant energy until the maximum energy that a particle can transmit to an atom which suffered the impact. A neutron of 1 MeV (0.16 pJ) can transfer about $10^5$ eV (0.016 pJ) to an atom. High-energy transfers can also be obtained by means of positive particles, but such energy transfers are less common. In the case of electrons, only low-energy transfers are possible. We shall consider here mainly the effects of neutron radiation on metals. The primary collision has the function of transferring energy to the atomic system. The subsequent events that occur are as follows.

1. Displacement of an atom from its normal position in the lattice to a position between the normal lattice sites.
2. Creation of defects by displacements and their migrations and interactions.

When an atom is displaced from its normal lattice site, two defects are created: an interstitial atom referred to as autointerstitial or self-interstitial, and a vacant lattice site called a vacancy. More complex configurations can be regarded as having started from this fundamental step. When an atom receives an energy impulse greater than a certain value $E_e$, called the *effective displacement energy*, some atom is displaced from its normal position to an interstitial position. In the most simple case, if an atom receives the primary impact of energy $E_e$, the atom itself is displaced. This, however, is not inevitable; sometimes another atom, a neighboring one, is displaced. With an increase in the energy imparted to the affected atom, various events can occur. At low energies, but higher than $E_e$, only an interstitial and its connected vacancy are possible. At high energies, the affected atom becomes an important particle for creating more damage. This leads to cascade elements.

Near the end of its trajectory, an energetic atom displaces all the atoms that it encounters; this is called a "displacement spike." Through a cascade effect, damage propagates through the lattice. Many atoms that spread about by displacement spikes will become situated along the atomic packing lines, and thus these lines will be a most efficient manner of transporting energy far away from the spike. The impact transferred along a crystallographic direction is called a *Focuson* (analogous to *photon* and *phonon*). If the energy is not well above the energy required for atomic displacement, it will be transferred into a chain of exchange collisions that makes the atom travel far away from the spike before it comes to a stop as an interstitial. The efficiency of this process is much higher in the close-packed directions (the <110> directions in FCC crystals). The atomic configuration in the <110> direction in which an interstitial is propagated along a line is called a *dynamic crowdion*. The efficiency of the focusing processes is directly proportional to the interatomic potential, being higher for heavy metals and lower for light metals (such as Al). According to the Seeger model, at zero kelvin, for each initially displaced atom, one would have one or more regions in which a good fraction of atoms (about 30%) disappear. These regions are surrounded by interstitial clouds that extend a few hundreds of atomic distances in noble metals and perhaps a few atomic distances in a metal such as Al. Seeger called the region of lost atoms in the center of a cascade a "depleted zone" and estimated that its typical size would be less than 1 nm. Figure 4.10 shows the Seeger model of damage produced by irradiation.

Vacancies generated during exposure to radiation often condense and form voids inside the material. An illustration of this is provided in Figure 4.11, which shows Ni irradiated by a high dosage of

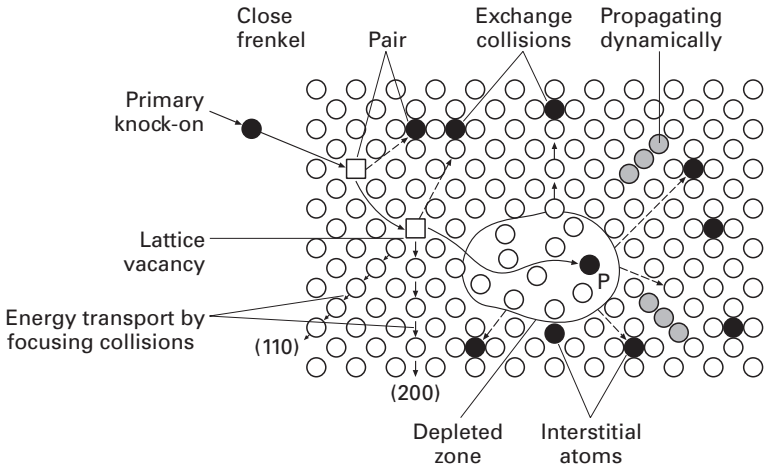


**Fig. 4.10** Seeger model of damage produced by irradiation. *P* indicates the position where the first "knock-on" terminates. (Reprinted with permission from A. Seeger, in *Proc. Symp. Radiat. Damage Solids React.*, Vol. 1, (Vienna, IAEA, 1962) pp. 101, 105.)

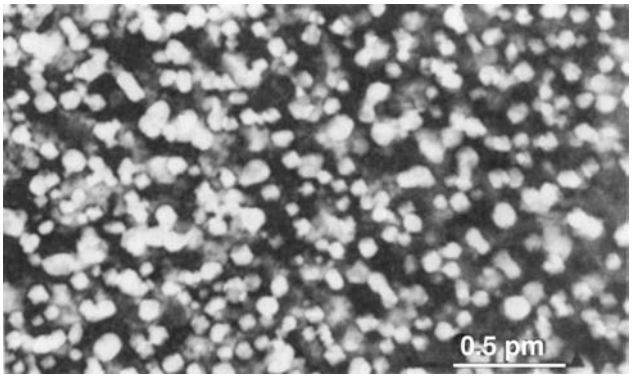


**Fig. 4.11** Voids formed in nickel irradiated using 400 keV $^{14}N_2^+$ ions to a dose of 40 dpa at 500 °C; notice the voids with polyhedral shape; dpa = displacements per atom. (Courtesy of L. J. Chen and A. J. Ardell.)

$N_2^+$ ions. A high concentration of voids is produced. The voids have polyhedral shapes because the surface energy is anisotropic and this shape, rather than a sphere, minimizes the overall surface energy.

In any event, a major portion of radiation damage in common metals caused by neutrons in reactors consists of a large number of interstitials and vacancies produced in a cascade process that follows after a primary knock-on impact. These point defects act as small obstacles to dislocation movement and result in a hardening of the metals. Besides this direct effect on mechanical properties, some indirect effects are possible. These indirect effects, which arise from the fact that irradiation by neutrons changes the rates and mechanisms of atomic interchange, are as follows.

**1.** Destruction of order of lattice.
**2.** Fractionating of precipitates.
**3.** Acceleration of nucleation.
**4.** Acceleration of diffusion.

These processes have their origin, directly or indirectly, in the kinetic energy exchanges between energetic neutrons and atoms. According to Seeger's model, atoms can be transported long distances by "cooperative" focalization along the more densely packed

directions, and the collision processes create simple defects, such as interstitials and vacancies, and complex defects, such as displacement spikes. If an alloy is ordered, focalization and displacement spikes may destroy the order. If the alloy contains precipitates, a displacement spike may break the precipitates if they are smaller than the spike and thus return the precipitates into solution. In an alloy that can have precipitates, the damaged regions caused by spikes can serve as nucleation sites. The excess vacancies produced by irradiation can accelerate the diffusion rate. All these effects influence significantly the mechanical properties. At ordinary temperatures (i.e., ambient or slightly above) one or both the defects (interstitials and vacancies) are mobile, and thus, the ones that survive the annihilation, due to recombination or loss of identity at sinks such as dislocations or interfaces, group together. It is well established that in a majority of metals, irradiation at low temperatures ($<0.2T_m$, where $T_m$ is the melting point, in kelvins) results in joining of vacancies and interstitials to form groups that are surrounded by dislocations (i.e., loops and tetrahedral packing defects). These groups impede dislocation motion, as well as increase the strength and reduce the ductility of the material. At high temperatures, the vacancies can group together to form voids. The formation of such groups of defects can cause important and undesirable changes in mechanical properties and result in a dimensional instability of the material. Damage accumulated during irradiation by neutrons (and other particles) can cause significant changes in important properties. For example, the yield stress or the flow stress increases, and frequently there is a loss of ductility.

The problem of mechanical and dimensional stability is a very serious one for structural components in fast reactors. In 1967, it was discovered that nuclear fuel cladding consisting of austenitic stainless steel, when exposed to high doses of fast neutrons, showed internal cavities (~10 nm). These cavities, called *voids*, result in an increase in the dimensions of the material. It is estimated that the maximum possible dilation in the structural components is of the order of 10%. However, as neutron flux and the temperature of the sodium coolant are not uniform in the core, the swelling of the component will be nonuniform. This nonuniformity can influence the component's behavior.

Irradiation by neutrons causes marked changes in the properties of the zirconium alloys Zircaloy-2 and Zircaloy-4 (both very much used in light water reactors) and in 304 and 316 stainless steels (used in liquid metal fast-breeder reactors). Figure 4.12 shows the increase in strength (yield strength and ultimate tensile strength) of Zircaloy after neutron radiation. The exact nature of the defects introduced by radiation that are responsible for these changes in Zircaloy are not well characterized. There is a considerable variation in the observed microstructures. One of the few observations about which there exists general agreement is the absence of radiation-induced vacancies in Zircaloy, which is a significant difference compared with, say, the behavior of stainless steels. Stainless steels show swelling due to

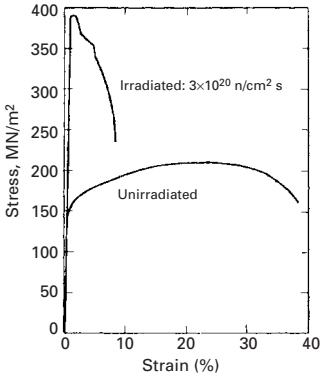


**Fig. 4.12** Stress–strain curves for irradiated and unirradiated Zircaloy. (Adapted with permission from J. T. A. Roberts, *IEEE Trans. Nucl. Sci.*, NS-22, (1975) 2219.)

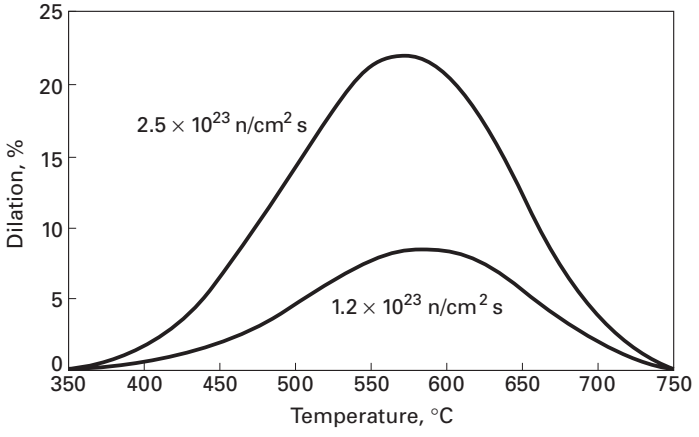


**Fig. 4.13** Stress-free dilation in AISI 316 steel (20% cold-worked). (Adapted with permission from J. T. A. Roberts, *IEEE Trans. Nucl. Sci.*, NS-22, (1975) 2219.)

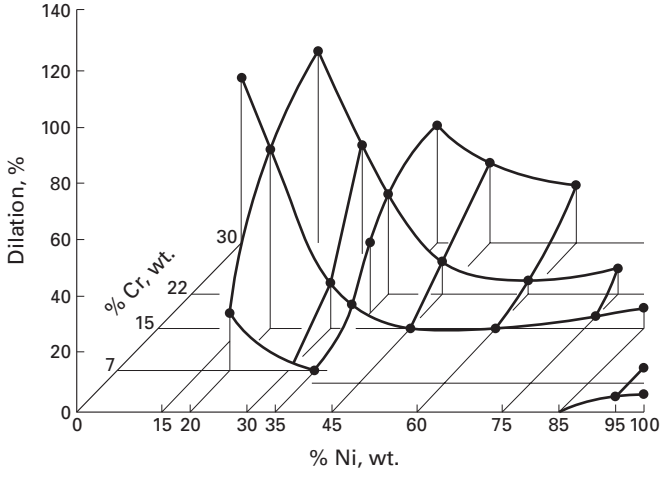


**Fig. 4.14** Dependence of fast neutron-induced dilation in stainless steel (Fe–Cr–Ni) as a function of Ni and Cr amounts. (Adapted with permission from W. B. Hillig, *Science*, 191 (1976) 733.)

neutron irradiation. The dilation induced by neutron irradiation in stainless steel depends on the neutron flux and the temperature, as shown in Figure 4.13. It is believed that the vacancies introduced by irradiation combine to form voids, while the interstitials are preferentially attracted to dislocations. According to Shewmon[3] this dilation of stainless steel does not affect the viability or security of breeder-type reactors, but will have a significant effect on core design and economy of reproduction. It would appear that, in spite of not being able to eliminate the effect completely, cold work, heat treatments, or changes in composition can reduce the swelling by a factor of two or more. Figure 4.14 shows the change in dilation of stainless steel as a function of Cr and Ni content.

### 4.3.5 Ion Implantation

An interesting technological application using charged particles is called *ion implantation*. Charged ions are accelerated in an electric field (e.g., in a linear accelerator) to very high energies (~200 keV) and

[3] P. G. Shewmon, *Science*, 173 (1971) 987.

allowed to strike the target solid in a moderate vacuum (~1 mPa). It is worth emphasizing that the selected species of ions is *implanted* into, and not deposited on, the target surface. The technique, originally developed for preparing semiconductor devices in a controlled fashion, has been made into a sophisticated tool for altering the composition and structure of surfaces for any number of purposes – for example, modifying the surface chemistry for better corrosion and oxidation resistance, tribological properties, and superconductivity. The reader can well imagine the power of the technique by the fact that it allows one to introduce elements into a surface, which may not be possible in conventional heat treatment because of low diffusivity. Depending on the dose, $B^+$, $N^+$, and $Mo^+$ ions implanted into steel can reduce the wear of a tool by an order of magnitude.

The ion implantation technique of modifying the composition and structure of surfaces has a number of advantages over conventional techniques:

1. The process is essentially a cold one; therefore, there is no loss of surface finish and dimensions (i.e., the process can be applied to finished parts).
2. One can implant a range of metallic and nonmetallic ions, individually or combined.
3. One can implant selected critical areas.

Ion implantation is particularly suited for the selected modification of small, critical parts. Oil burners used for injecting a mixture of fuel oil and air into boilers of oil-fired power plants face rather severe erosion conditions. Ti and B implantation of oil-burner tips improved erosion properties and increased the service life of the boilers.

Another very important aspect of ion implantation has to do with the fact that it is basically a nonequilibrium process. There are thus no thermodynamic constraints, such as solubility limits. In other words, we are able to produce metastable alloys with new and unusual characteristics, amorphous alloys, and so on. Hence, the technique offers a novel way of producing surfaces, in a controlled manner, for scientific studies.

## 4.4 Line Defects

Bands in the surface of plastically deformed metallic specimens were reported as early as the 19th century. With the discovery of the crystalline nature of metals, these bands were interpreted as being the result of the shear of one part of the specimen with respect to the other. Similar slip bands (or markings) were observed by geologists in rocks. However, calculations of the theoretical strength of crystals based on the simultaneous motion of all atoms along the slip band showed systematic deviations of several orders of magnitude with respect to the experimental values. (See Section 4.2.) This discrepancy led to the concept of line imperfections in crystals called *dislocations*.

Later, the actual existence of such imperfections was verified by a variety of techniques.

Figures 4.15 and 4.16 present two analogies that help us to visualize dislocations. The displacement of a rug can be accomplished by applying a much lower force if a wave is created in the rug and moved from the back to the front. This displacement, *b*, is indicated in Figure 4.15. In a similar manner, caterpillars move by creating a "dislocation" and displacing it from the back to the front. (See Figure 4.16.) Sidewinders use a similar principle: these snakes generate "waves" along their bodies. The movement of the wave propels the snake sideways. Having understood this concept, the diligent student can readily comprehend how the movement of a dislocation in a body can produce plastic deformation.

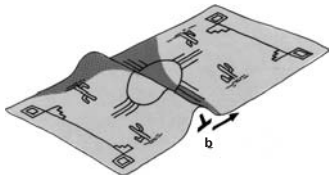


**Fig. 4.15** (a) Rug with a fold.

Figure 4.17 shows two distinct types of dislocations encountered in crystalline solids: edge and screw dislocations. The atomic arrangement surrounding these dislocations is distorted from the regular periodicity of the lattice. The edge dislocation (Figure 4.17(a)) may be visualized as an extra half plane of atoms terminating at the dislocation line (perpendicular to the plane of the paper and passing through the symbol "⊥".) The screw dislocation can be visualized as a "parking garage:" a car, driving around the dislocation line will go up or down the building. Another analogy is the screw. Figure 4.17(a) shows the atomic arrangement. The distortion of the periodic atomic arrangement is represented by the Burgers vector **b**. A circuit is created around the dislocation line, as indicated by *ABCDE*. *AB* and *CD* correspond to 4*a*, where *a* is the interatomic spacing. *BC* and *DE* correspond

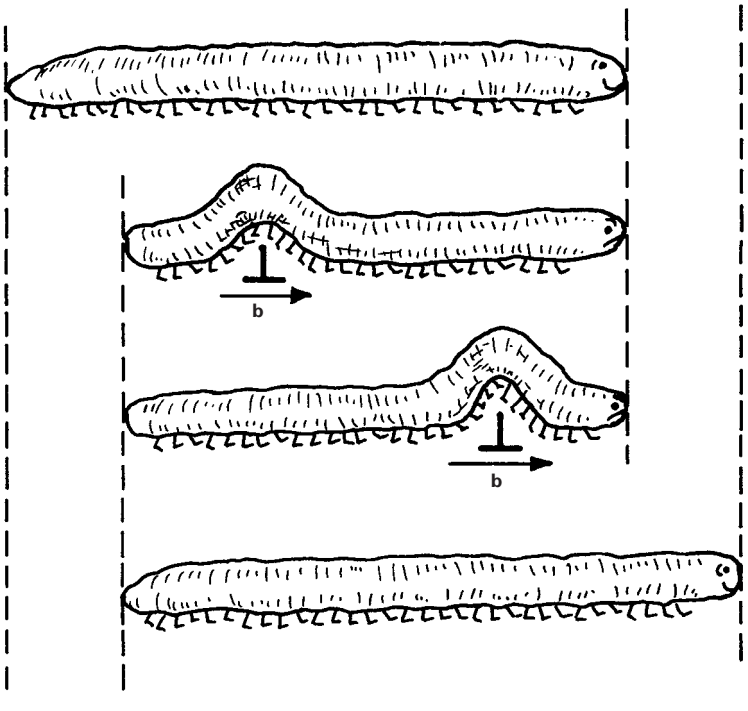


**Fig. 4.16** Caterpillar with a hump.

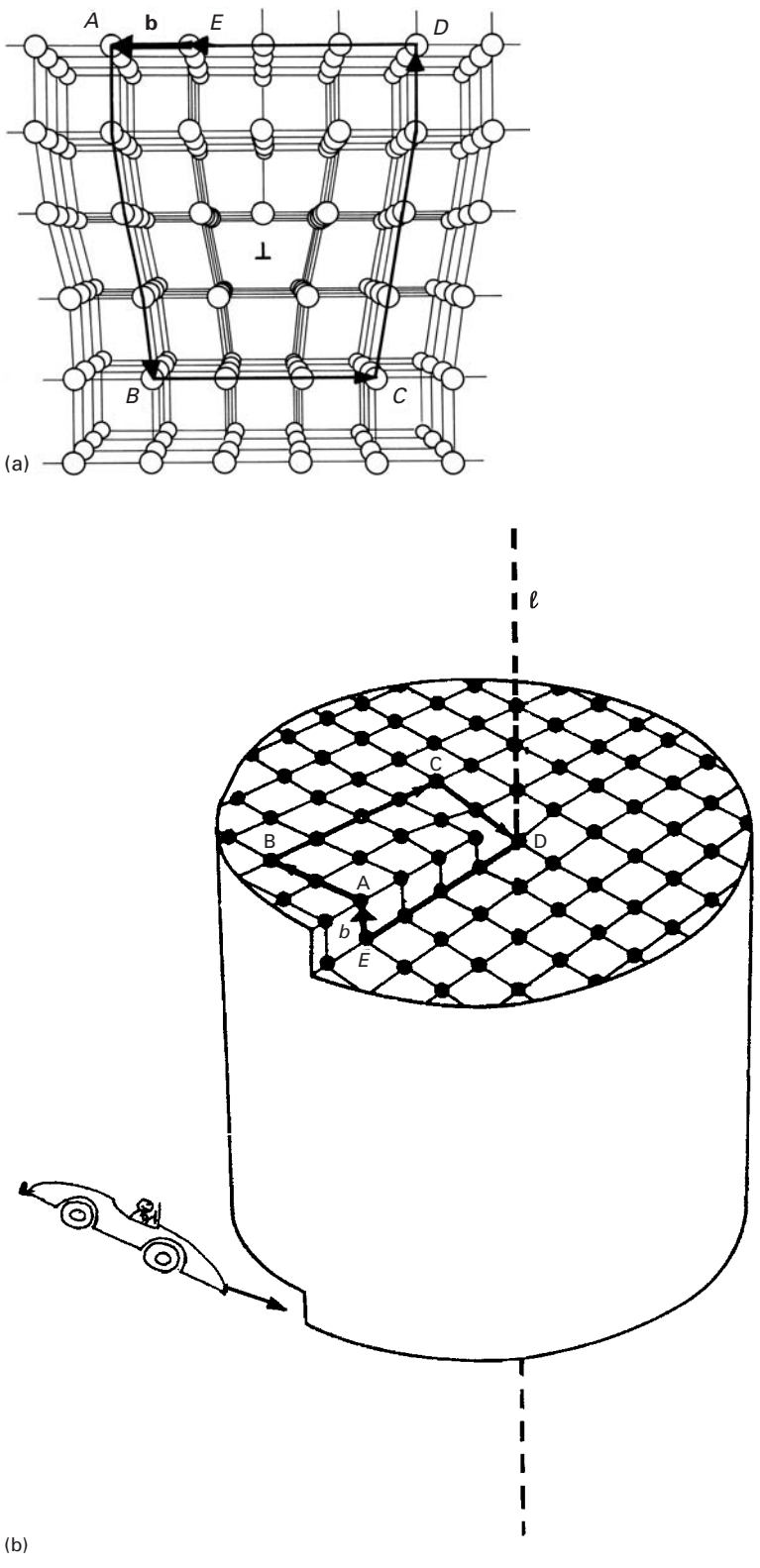


**Fig. 4.17** (a) Arrangement of atoms in an edge dislocation and the Burgers vector **b** that produces closure of circuit *ABCDE*. (b) Arrangement of atoms in screw dislocation with "parking garage" setup. (Notice car entering garage.)

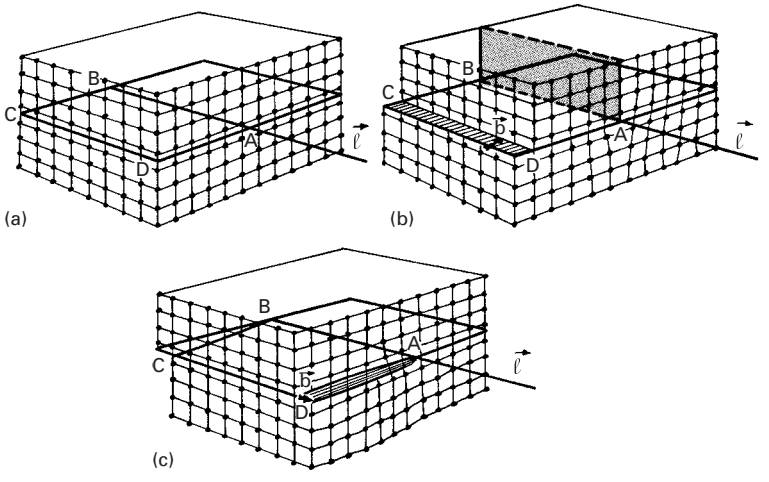


**Fig. 4.18** Geometrical production of dislocations. (a) Perfect crystal. (b) Edge dislocation. (c) Screw dislocation.

to 3*a*. The failure of the circuit to close represents the vector **b**. A Burgers circuit is also represented around the screw dislocation in Figure 4.17(b). The essential difference between these two types of dislocation is that in the edge dislocation, **b** is perpendicular to dislocation line vector, $\ell$, whereas in the screw dislocation, **b** is parallel to $\ell$.

Edge dislocations were proposed by Orowan, Polanyi and Taylor, in 1934.[4] Screw dislocations were proposed by Burgers in 1939.[5] Figure 4.18 shows how the shearing of the lattice can generate edge and screw dislocations. Imagine a cut made along *ABCD* in Figure 4.18(a). If the shearing direction is as marked in Figure 4.18(b), the Burgers vector is perpendicular to line *AB* or $\ell$. The resultant dislocation is of edge character. If the shearing direction, defined by **b**, is parallel to *AB*, then $\mathbf{b} \parallel \ell$, and the resulting dislocation is of screw character. (See Figure 4.18(c).) The movement of an edge dislocation under an applied shear stress $\tau$ is shown in Figure 4.19. The perfect lattice shown in Figure 4.19(a) is broken and the dislocation is formed as shown in Figure 4.19(b). This edge dislocation ($\mathbf{b} \perp \ell$ ) moves from left to right, and the final, deformed configuration is shown in Figure 4.19(c). The relationship between the applied shear stress, the direction of movement of dislocation, and the plastic strain generated is quite different for the two types of dislocation. Figure 4.20 shows how a hypothetical crystal subjected to a shear stress $\tau$ undergoes plastic deformation by means of the propagation of (a) an edge dislocation and (b) a screw dislocation. The direction of motion of the dislocations is always parallel to **b**. The final shear is the same, but the motion of the two dislocations is completely different. There is also a mixed dislocation that possesses both screw and edge character. Figure 4.21 shows such a dislocation, together with the "cut." It can be seen that the shear direction is neither parallel (screw) nor perpendicular (edge) to the direction of the cut.

[4] E. Orowan, *Z. Phys*., 89 (1934) 604. M. Polanyi, *Z. Phys*., 89 (1934) 660. G. I. Taylor, *Proc. Roy. Soc*. (*London*), A145 (1934) 362.

[5] J. M. Burgers, *Proc. Kon. Ned. Akad. Wetenschap*., 42 (1939) 293, 378.

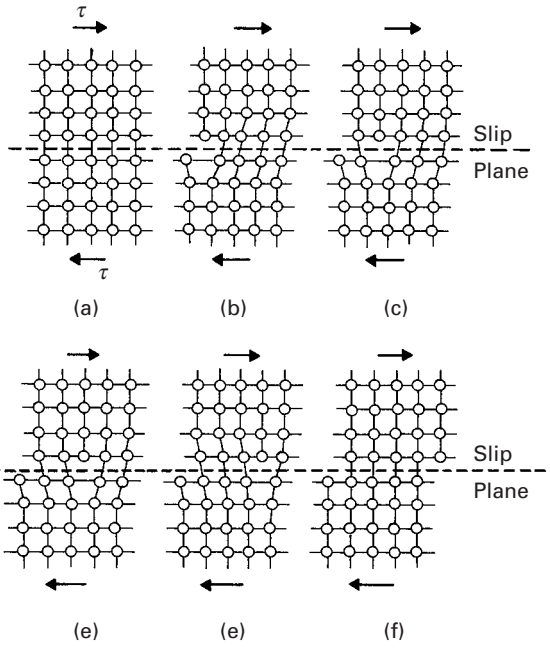


**Fig. 4.19** The plastic deformation of a crystal by the movement of a dislocation along a slip plane.

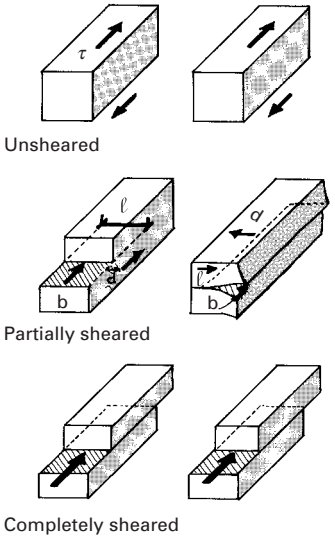


**Fig. 4.20** Plastic deformation (shear) produced by the movement of (a) edge dislocation and (b) screw dislocation. Note $d$ is the direction of dislocation motion; $\ell$ is the direction of dislocation line.

Another type of dislocation is called a *helical dislocation*. It forms a large helix and is sometimes observed in crystals that were heat-treated to produce climb. "Climb" is the movement of a dislocation perpendicular to its slip plane. "Glide" is the movement along the slip plane. Climb is described in Chapter 13 (Creep). These dislocations are of mixed character; the reader should not confuse them with screw dislocations.

Dislocations will be studied in detail in this chapter, since they are the building blocks for the understanding of the mechanical response of metals. The treatment, however, still is far from comprehensive. For further details, the reader is referred to the suggested readings at the end of the chapter.

### 4.4.1 Experimental Observation of Dislocations

It took 20 years to prove, beyond any doubt, the existence of dislocations experimentally, and this period (1935–1955) was surrounded by skepticism and harsh polemics. Nevertheless, the existence of dislocations is nowadays universally recognized, and the "lunatic" theories and models have been proven to be remarkably correct. A number of techniques have allowed the observation of dislocations, including etch pitting, X-ray diffraction (Berg–Barrett topography), and, most importantly, transmission electron microscopy (TEM). The last one is established as the principal method for observing dislocations.

In TEM, the foil has to be thinned to a thickness between 0.1 and 0.3 μm, becoming transparent to electrons when the accelerating voltage is in the 100–300 kV range. Dislocations produce distortions

of the atomic planes. Hence, for certain orientations of the foil with respect to the beam, the region around a dislocation diffracts the beam. The dislocations can then be seen as dark, thin lines under a bright field. TEMs with higher operating voltages (in the megavolt range) are available and allow thicker specimens to be observed. Figure 4.22 shows dislocations in titanium and silicon rendered visible by this technique. The dislocations in titanium (Figure 4.22(a)) appear as sets of parallel segments; the segments are parallel because the dislocations minimize their energy by being along certain crystallographic planes. The same phenomenon is observed in silicon (see Figure 4.22(b)). A hardness indentation (lower right-hand corner) generated a profusion of dislocation loops. These loops are not circular, but consist of segments that are crystallographically aligned because of energy minimization considerations. The dislocation configurations in materials are highly varied and depend on a number of parameters, such as total strain, strain rate, stress state, deformation temperatures, crystallographic structure, etc. Note that the dislocations in silicon (Figure 4.22(b)) appear as white lines, whereas in Figure 4.22(a) they are dark lines. This is because Figure 4.22(b) is a dark-field image, in which the grain diffracts, and the dislocation transmits, the electron beam. The figure is opposite to the normal bright-field transmission images (Figure 4.22(a)).

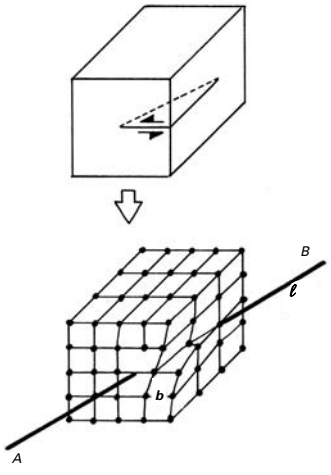


**Fig. 4.21** Mixed dislocation obtained from cut-and-shear operation; notice the angle between **b** and $\ell$.

Dislocations are also present in ceramics, although they are less mobile. They can be produced by plastic deformation at high temperatures, by thermal stresses during cooling, or by applying very high stresses, made possible by, for instance, impacts at several hundred meters per second. Figure 4.23 shows dislocations observed in alumina

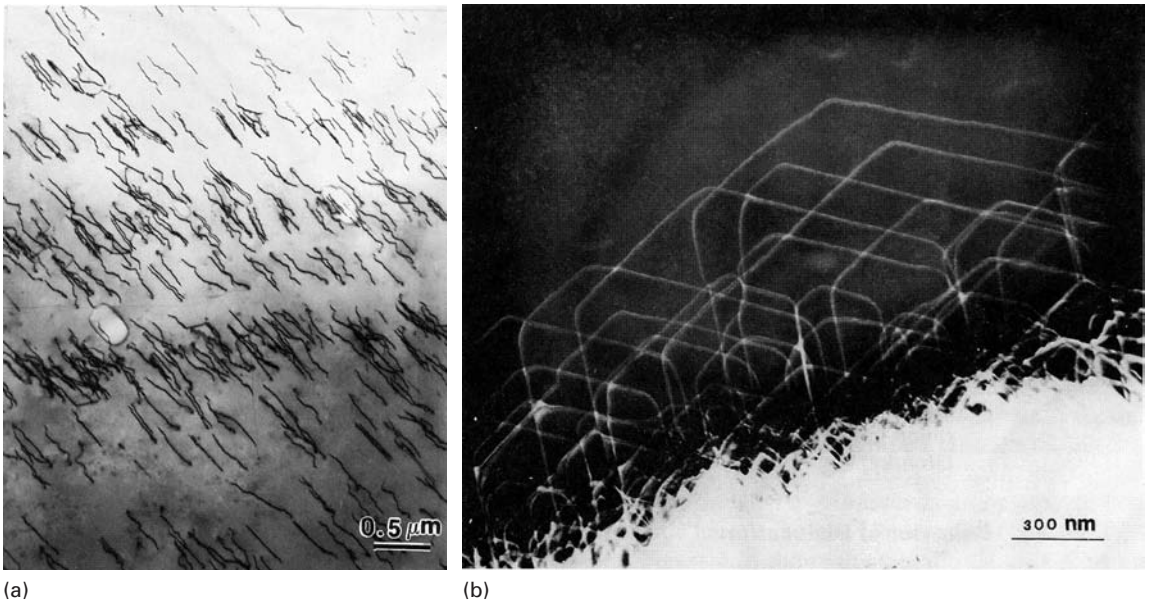


(a) (b)

**Fig. 4.22** Dislocations in metals. (a) Titanium. (Courtesy of B. K. Kad.) (b) Silicon.


(a) (b)

**Fig. 4.23** Dislocations in (a) $Al_2O_3$ and (b) TiC. (Courtesy of J. C. LaSalvia.)

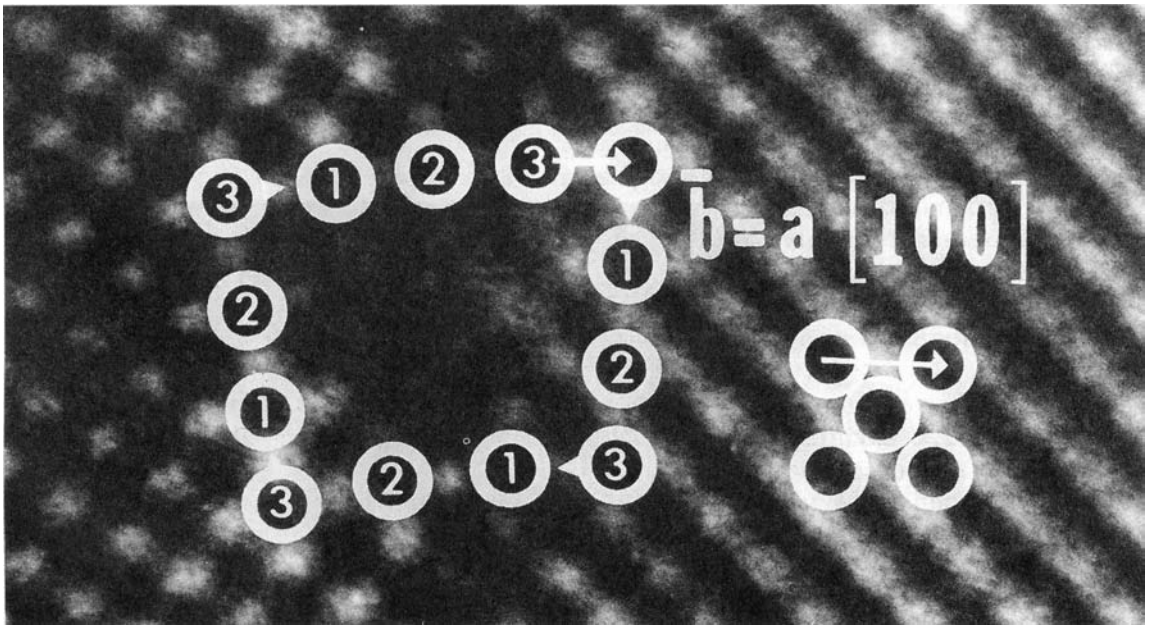


**Fig. 4.24** Atomic resolution transmission electron micrograph of dislocation in molybdenum with a Burgers circuit around it. (Courtesy of R. Gronsky.)

and titanium carbide. The dislocations in the alumina were generated by impact at 600 m/s. The dislocations in the titanium carbide were produced by plastic deformation above the material's ductile-to-brittle transition temperature (~2,000 °C). At room temperature, this ceramic would simply undergo brittle fracture.

High-resolution TEM can resolve the individual atoms and identify the lattice distortions around a dislocation. Figure 4.24 shows

molybdenum imaged in such a fashion. The dark spots represent one atom each. Mo has the BCC structure, and the foil plane imaged is (100). The right-hand side of the picture shows a unit cell. A Burgers circuit is drawn around an edge dislocation, which has a line $\ell$ perpendicular to the plane of the foil. The closure gap represents the Burgers vector of the dislocation. A comparison of the figure with the unit cell establishes the magnitude of the Burgers vector; it is equal to the lattice parameter $a$. This is clearly indicated in the figure. The presence of the dislocation can also be felt by noticing the break in the [110] planes, making 45° with the cube axes.

The electron micrographs of Figures 4.22–4.24 illustrate the presence and variety of dislocation configurations observed in crystalline materials.

## 4.4.2 Behavior of Dislocations

*Dislocation Loops*

A dislocation line can form a closed loop, instead of extending until it reaches an interface or the surface of the crystal. This is illustrated in Figure 4.25(a), where a square loop is sketched. Two cuts, along perpendicular sections, were made: *AAA* and *BBB*. Figure 4.25(b) and (c) show these sections. It can clearly be seen that the dislocation segments *CF* and *DE* (Figure 4.25(b)) are of edge character, while segments *CD* and *FE* (Figure 4.25(c)) are of screw character. This is due to the direction of the shear. The loop can be imagined as a cut made in the interior of the crystal (an impossible feat, of course); the edges of the cut form the dislocation line, after shear is applied to the crystal. Dislocations *CF* and *DE* are of the same type, with opposite signs; the same applies to *CD* and *FE*. The sign convention used for edge dislocations is the following: If the extra semiplane (wedge) is on the top portion, it is positive; if on the bottom, it is negative. Hence, *CF* is positive and *DE* is negative. For screw dislocations, a similar convention is used. If the helix turns in accord with a normal screw, it is positive. If not, it is negative. According to this convention, *CD* is positive and *FE* is negative.

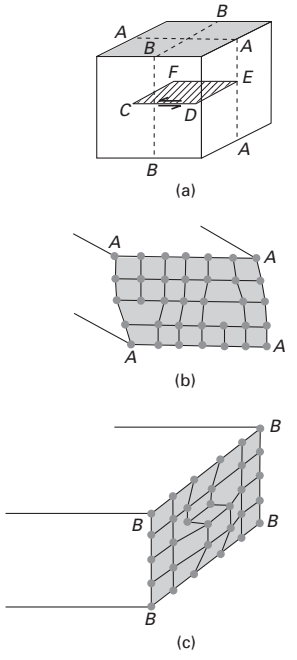


**Fig. 4.25** Square dislocation loop.

The actual dislocation loops are not necessarily square. An elliptical shape would be more favorable energetically than a square. For an elliptical or circular shape, the character of the dislocation changes continuously along the line. Figure 4.26(a) shows this situation; the regions that are edge and screw are shown by appropriate symbols. The symbols most commonly used are an inverted T (⊥) for a positive edge, and an S for a positive screw dislocation. The negative signs can be described by a correct T and by an inverted S (<S>). In Figure 4.26(a), all the portions of the loop between the short segments of pure screw and edge character are mixed. These loop segments move as shown in the figure. The loop expands and eventually "pops out" of the parallelepiped, creating the shear shown in Figure 4.26(b). Figure 4.26(c) shows a shear loop in copper.

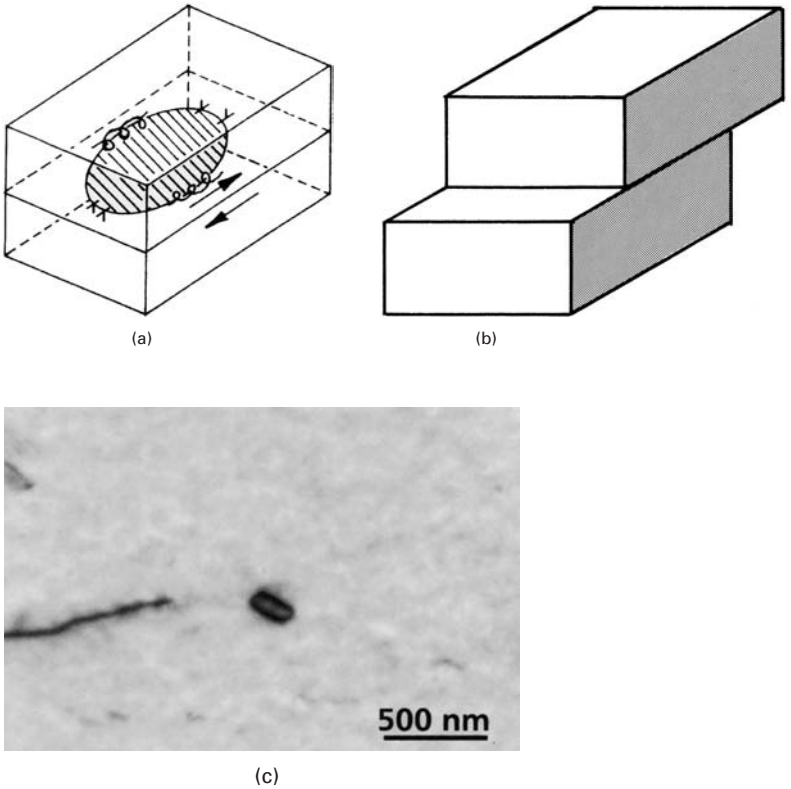


**Fig. 4.26** Elliptic dislocation loop. (a) Intermediate position. (b) Final (sheared) position. (c) TEM of shear loop in copper (Courtesy of F. Gregori and M. S. Schneider.)

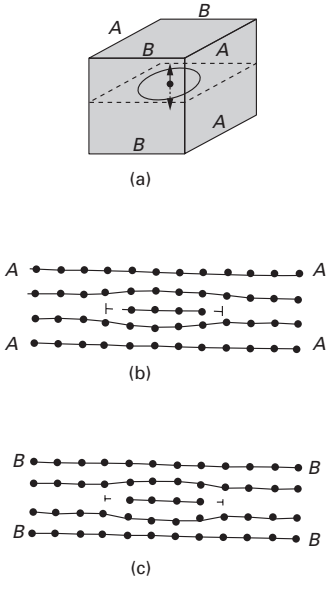


**Fig. 4.27** Prismatic loop produced by the introduction of a disk into metal. (a) Perspective view. (b) Section *AAAA*. (c) Section *BBBB*.

There is another type of loop, called a *prismatic loop*, that should not be confused with a common loop. A prismatic loop is created when a disk of atoms is either inserted or removed from the crystal. Figure 4.27(a) shows this situation; cuts *AAAA* and *BBBB* are indicated. A disk having the thickness of one atomic layer was introduced and it can be seen that sections *AAAA* (Figure 4.27(b)) and *BBBB* (Figure 4.27(c)) are identical. They are edge dislocations with opposite signs. This configuration is very different from that encountered in normal loops. One can also *remove* a disk of atoms, instead of adding it. These loops do not have the same ability to move as do normal loops because the Burgers vector is perpendicular to the loop.

### Movement of Dislocations

The plastic deformation of metals is normally accomplished by the movement of dislocations. The elements of dislocation motion are reviewed in this section, together with the resulting deformations. In actual deformation and for elevated strains, complex interactions occur between dislocations. These interactions can be broken down